NASA Contractor Report 3333

# Analytical and Experimental Study of Mean Flow and Turbulence Characteristics Inside the Passages of an Axial Flow Inducer

C. A. Gorton and B. Lakshminarayana

NASA

NASA Contractor Report 3333

# Analytical and Experimental Study of Mean Flow and Turbulence Characteristics Inside the Passages of an Axial Flow Inducer

C. A. Gorton and B. Lakshminarayana
*The Pennsylvania State University*
*University Park, Pennsylvania*

# NASA

National Aeronautics
and Space Administration

Scientific and Technical
Information Branch

1980

TABLE OF CONTENTS

TABLE OF CONTENTS (concluded)

NOMENCLATURE

| | |
|---|---|
| AX, N1, N2 | Orthogonal coordinate system along hotwire axis (Fig. 9) |
| B | Slope of hotwire calibration curve |
| C | Total absolute velocity |
| $C_f$ | Skin friction coefficient |
| $C_\theta$ | Absolute tangential velocity |
| E | Output D.C. voltage of hotwire anemometer |
| $E_o$ | D.C. voltage of hotwire anemometer at zero velocity |
| e | Output A.C. voltage of hotwire anemometer |
| F | Body force including viscous terms |
| $g_o$ | Gravitational acceleration |
| h | Static head |
| K | Hotwire correction factor for the deviation from the cosine law |
| L | Constant used to relate hotwire voltage and velocity |
| N | Number of blades |
| n | Unit normal to blade surface |
| $0(\varepsilon)$ | Terms of small order |
| P | Static pressure |
| Q | Mean velocity sensed by hotwire probe |
| $Q_R$ | Total relative velocity |
| q | Fluctuating velocity sensed by hotwire probe |
| R | Nondimensionalized radius (= $r/r_t$) |
| R, $\theta$, Z | Rotating cylindrical coordinate system (Fig. 2) |
| $R_e$ | Reynolds number (=$\overline{Q_R} \cdot r/\nu$) |
| r | Local radius |

| | |
|---|---|
| s | Blade surface point |
| U, V, W | Mean relative velocity components in the $R,\theta,Z$ directions respectively (in experimental results nondimensionalized with respect to $U_b$) |
| $U_b$ | Blade tip speed (= $r_t\Omega$) |
| u, v, w | Fluctuating relative velocity components in the $R,\theta,Z$ directions respectively (in experimental results, nondimensionalized with respect to $Q_R$) |
| x | Location of a unit source |
| Z | Nondimensional axial location (= $z/r_t$) |
| z | Local axial location |
| $\alpha$ | Blade limiting streamline angle |
| $\beta$ | Angle of the flow with inducer axis |
| $\gamma$ | Angle of the blade with inducer axis |
| $\Delta$ | Small quantity or change |
| $\epsilon_w$ | Blade limiting streamline parameter (= $\tan \alpha$) |
| $\xi$ | Source strength |
| $\theta$ | Local tangential location |
| $\nu$ | Kinematic viscosity |
| $\rho$ | Fluid density |
| $\sigma$ | Normal stress |
| $\tau$ | Shear stress |
| $\tau_w$ | Wall shear stress |
| $\phi$ | Inlet flow coefficient |
| $\psi_s$ | Static head coefficient (= $2g_o h/U_b^2$) |
| $\psi_T$ | Stagnation head rise coefficient |
| $\Omega$ | Angular velocity of inducer |

NOMENCLATURE (concluded)

## Superscripts

$^{-}$               Time-averaged or passage-averaged quantity

$\rightarrow$               Vector quantity

## Subscripts

| | |
|---|---|
| ax, n1, n2 | Components along AX,N1,N2 directions (Fig. 9) |
| m | Refers to manometer values |
| o | Initial value |
| t | Refers to values at the inducer tip |
| w | Refers to values at the inducer blade surface |
| 1, 2, 3 | Refers to values sensed by hotwire sensors 1,2,3 (Fig. 9) |

# INTRODUCTION

## Objectives and Statement of the Problem

Inducers are designed to increase the suction specific speed of centrifugal impellers in liquid rocket feed systems and are used to provide a small head rise sufficient to operate without cavitation. Typical inducer characteristics include high solidity (ratio of blade chord to blade spacing), low aspect ratio (span squared to blade area), and low flow coefficient (ratio of inlet axial velocity to blade tip speed). The flow in these long and narrow passages is greatly influenced by the effects of turbulence and viscosity, resulting in large friction losses and introducing considerable three-dimensionality in the flow, thus making the prediction of the flow behavior extremely difficult. Secondary motions within the inducer are not confined to thin regions at the blade surface, but extend over the entire cross-section of the flow.

The primary objective of the current study reported in this thesis has been to gather additional understanding of the complex inviscid and viscid effects on the inducer flow field, including the three components of mean velocity, turbulence intensities and turbulence stresses inside the passage. It is hoped that the knowledge gained from this investigation will serve the establishment of a theoretical model for the eventual analysis of the three-dimensional flow in inducers as well as other turbomachinery dominated by secondary fluid motions caused by viscosity and turbulence. Hence, the subjects addressed in this thesis are:

2

1) To develop measuring techniques using a triaxial hotwire probe to measure the three components of velocity, turbulence intensities and stresses within the rotating blade channel.

2) Using these techniques, to carry out a complete flow survey of two axial stations within the blade passage.

3) To perform a complete survey of the static pressure distribution on the blade suction and pressure surfaces.

4) To perform a complete survey of limiting streamline angle on the blade suction and pressure surfaces.

5) To predict the three-dimensional inviscid flow in the inducer by numerically solving the exact equations of motion and to study the possible methods of reducing the computation time required for the convergence to the solutions of these equations.

6) To approximately predict the three-dimensional viscid flow in the inducer using dominant viscous terms in the exact solution equations.


Previous Related Work

The Department of Aerospace Engineering at The Pennsylvania State University has been conducting a systematic analytical and experimental investigation of flow behavior in axial flow inducers under NASA sponsorship since November 1963. A brief summary of previous theoretical and experimental results obtained from this investigation is given in this section, in addition to the applicable results of related research by other sources.

Analytical Investigations

Because of the presence of large secondary flows caused by three-dimensional boundary layers and the complexity of the viscid equations of motion governing the inducer flow, very little theoretical analysis is available related to the prediction of the three-dimensional flow characteristics. Most of the design and analysis of the inducer fluid flow is based on conventional two-dimensional methods.

Montgomery (Ref. 17) used the simplified radial equilibrium equation

$$\frac{\partial h}{\partial r} = \frac{C_\theta^2}{g_o r} \tag{1}$$

in conjunction with arbitrary expressions for the losses to predict the exit head rise and flow coefficient for an $80^o$ helical inducer. However, the use of arbitrary loss expressions does not provide any specific method of relating the loss distribution to a given inducer geometry or flow characteristic.

An approximate solution using the simplified radial equilibrium equation in an integrated form has been obtained for a four-bladed inducer by Lakshminarayana (Ref. 9). The basic assumptions in this analysis are the existence of fully developed turbulent flow, the shape of the radial and mainstream direction velocity profiles and the use of empirically determined friction loss coefficients. This analysis leads to a good prediction of the outlet absolute tangential velocity, but axial velocities are not predicted due to the lack of accurate information concerning the radial velocity profiles within the blade passage.

The momentum integral equations valid for the inducer have been developed and programmed for numerical solution (Ref. 2). The equations

take into account the changes in free stream velocity due to camber and incidence in addition to the interaction between the pressure and suction surface boundary layers, and is based on skin friction correlations for rotating boundary layers developed in Ref. 14. The numerical technique utilizes a fourth-order difference scheme. Preliminary results of the analysis are discussed in Ref. 2.

An accurate knowledge of boundary layer characteristics and skin friction losses in a rotating channel is a prerequisite for the development of an acceptable theoretical model for the inducer flow. While a considerable amount of information on viscous flow in a non-rotating flow passage is available, there is no information available for the rotating case. A systematic study of the boundary layer on a rotating blade and inside a rotating channel has been undertaken by the Aerospace Engineering Department at The Pennsylvania State University. In the first phase of this program, the boundary layer on a simpler configuration (a single rotating helical blade of large chord length enclosed in an annulus) was studied. The results of this investigation are reported in Ref. 14. Consequently, this investigation has been extended to a four-bladed flat plate inducer in Ref. 2, where an attempt has been made to predict and measure the boundary layer characteristics inside the blade passage. Further study is to be made on the three-dimensional boundary layer characteristics within the inducer passage by utilizing the rotating hotwire anemometry techniques developed in this thesis. Information gained through this investigation should provide knowledge of the significant viscous effects within the blade passage and eventually lead to the exact prediction of the inducer flow.

A significant contribution toward the general solution of the equations governing the inducer flow is due to Cooper and Bosch (Ref. 4). This three-dimensional analysis employs an iterative numerical procedure to solve the inviscid equations of motion, expressed in finite-difference form, for a grid of points representing the channel between the blades. This method is discussed in greater detail in a later section of this thesis.

Experimental Investigations

Several experimenters have investigated inducers of varying geometry and inlet angle and have tested them in various fluids such as water, liquid hydrogen or nitrogen under a wide range of flow parameters (Refs. 16, 17, 18, 19, 21, 23, 24). In most cases, however, these studies deal only with cavitation performance, overall performance and efficiency.

Acosta (Ref. 1) has studied the cavitating and non-cavitating performance of $78^\circ$, $81^\circ$ and $84^\circ$ helical flat plate inducers under various flow coefficients. His investigations at $\phi = 0.070$ under non-cavitating conditions observed a deterioration in the radial distribution of axial velocity and head rise at the inducer exit, with a backflow region near the hub and a sharp positive gradient in head rise near the tip. These results are similar to those obtained in Ref. 20 for a three-bladed inducer at $\phi = 0.065$. Acosta attributes strong three-dimensional and viscid effects for the departure of the flow from design values based of the simplified radial equilibrium equation. He also noticed a decrease in inducer efficiency at large solidity, which can be attributed to the influence of blade blockage on flow characteristics

and an increase in viscous and turbulent mixing losses due to the decrease in channel width. These results are confirmed in Refs. 11 and 20. Soltis, Anderson and Sandercock (Ref. 23) were led to similar conclusions while investigating the non-cavitating performance of a 78$^{\circ}$ axial inducer under various flow coefficients. They derived the outlet axial velocity profile using experimental values of the total pressure and outlet flow angles in the simplified radial equilibrium equation. This analysis tends to establish that the flow is axisymmetric at small axial distances downstream of the trailing edge, since radial velocities are likely to be small and the wake diffusion in such inducers is very rapid. Similar observations are made by Mullan (Ref. 18), Meng and Moore (Ref. 16), Montgomery (Ref. 17), and Osborn (Ref. 19).

The main conclusions of the various investigations described above are:

1) The overall head rise coefficient increases, especially near the tip, when the operating flow coefficient decreases.

2) The total head rise coefficient increases when the solidity of the blades is decreased.

3) The radial distribution of outlet velocity tends to deteriorate when the flow coefficient is decreased. At low flow coefficients and for most inducer configurations, there is a large positive radial gradient in exit axial velocity with a backflow near the hub.

Experimental investigations at The Pennsylvania State University have been conducted on a three-foot diameter inducer operated in air at a flow coefficient of $\phi = 0.065$. The inducer has been operated with four, three, and two blades giving solidities at the tip of 2.86, 2.13,

and 1.43 respectively. The inducer test facility is shown in Fig. 1a, with design values of inducer inlet and outlet angles given in Fig. 1b.

A visualization study of the flow through the four-bladed inducer configuration is reported in Ref. 10. The flow near the blade surfaces, inside the rotating passage, downstream and upstream of the inducer is visualized by means of smoke, tufts, ammonia filament and lamp black techniques. The flow is found to be highly three-dimensional with appreciable radial velocity throughout the passage. Some of the major conclusions of this visualization study are:

1) At or near design flow coefficient, no backflow is observed upstream of the inducer. A separated region of the flow exists near the hub at the discharge of the inducer.

2) The extent of the backflow increases considerably, both at inlet and at exit, for flow coefficients lower than the design value.

3) The expected radial motions within the blade passage have been confirmed and appear to be quite strong at all the radii.

4) The radial flows inside the blade boundary layer, when encountered by the annulus wall, tend to deflect toward the mid-passage and then radially inward.

The qualitative nature of the velocity profiles, derived from visualization experiments (Ref. 10), indicate that the conventional practice of assuming the boundary layer is thin, two-dimensional and is a small perturbation of the inviscid flow is not valid in this case. The values of limiting streamline angles are found to be large.

The flow measurement at several stations downstream of the blade row are reported in Refs. 9, 20 and 11 for four-, three- and two-bladed inducers respectively. The radial distribution of stagnation and static

8
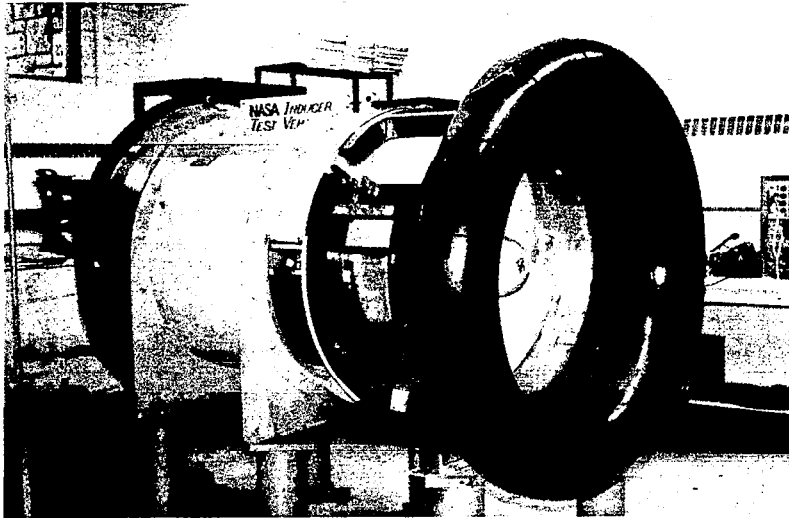


Figure 1a.  Inducer Test Facility
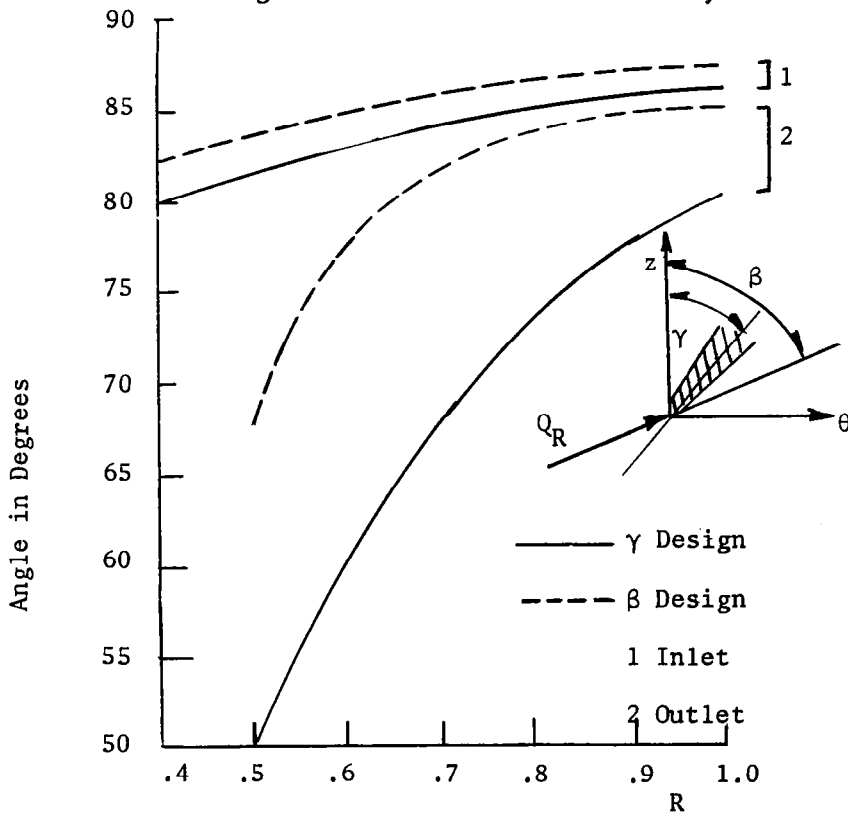


Figure 1b.  Inducer Inlet and Outlet Angle

pressure, axial and tangential velocity and flow angles of the absolute flow were measured at the several locations downstream using conventional and hotwire probes. Absolute flow measurements were also carried out at the exit of the three-bladed and two-bladed inducers and reported in Refs. 8 and 20 and Ref. 11 respectively. All inducers were tested at the same flow coefficient and Reynolds number. Major conclusions derived by comparison of these measurements with those of the four-bladed inducer are:

1) The performance of the inducer improves continuously with decrease in solidity, the two-bladed inducer showing substantial improvement over both the four- and three-bladed inducers.

2) The static and stagnation head rise increases continuously, at all radii, with decrease in solidity. The radial gradient of stagnation head rise coefficient, $\partial \psi_T / \partial r$, is found to be almost constant from hub to tip for the two-bladed inducer, unlike that at the other solidities where a steep rise is observed near the tip.

3) The downstream axial velocity profile is found to be similar, qualitatively, for all the inducers tested. The steep rise in axial velocity toward the tip observed in three- and four-bladed inducers is absent in the case of the two-bladed configuration, but the extent of separated zone (backflow) near the hub increases continuously with decrease in solidity.

4) The radial distribution of tangential velocity shows a trend similar to the $\psi_T$ distribution. However, the large values of $\partial V / \partial r$ observed in four- and three-bladed inducers are reduced substantially in the two-bladed configuration.

10

5) Hydraulic efficiency (local as well as overall) increases continuously with decrease in solidity.

In order to understand the flow behavior inside the inducer passages, experimental investigation of the relative blade-to-blade flow inside the inducer passages is undertaken using rotating pressure probes and the pressure transfer device. Measurements inside the four-bladed inducer are reported in Refs. 7 and 15 and for the three-bladed inducer in Refs. 7 and 20. The measurement of relative flow near the trailing edge reveals the presence of a loss core located slightly inward from the tip. The mid-passage at this radius is found to have minimum relative stagnation pressure and hence maximum loss. The radial velocity inside the blade boundary layer, when encountered by the annulus wall, tends to deflect toward the mid-passage and then radially inward. These inter-action effects are responsible for the large losses observed experi-mentally. These loss regions extend radially from mid-radius to tip. Comparison of the relative flow measurements taken in the three- and four-bladed inducers provide the following conclusions:

1) Measurements taken near the leading edge shows marked reduction in boundary layer growth, flow losses and radial inward velocity in the case of the three-bladed inducer. The losses near the tip are nearly halved from those of the four-bladed inducer and the "wake" type of profile observed near the mid-passage of the tip disappears in the case of the three-bladed inducer.

2) Measurements taken near the trailing edge indicate that the relative velocity and pressure distributions (blade-to-blade) are similar for both of the inducers, even though there is appreciable

reduction in losses and relative flow diffusion in the case of the three-bladed configuration.

3) There is appreciable improvement in hub and wall static pressure distribution in the case of the three-bladed inducer.

A method of measuring the three velocity components and the corresponding turbulent intensities has been developed for a stationary reference frame and has been reported in Refs. 12 and 20. This procedure, which utilizes three stationary hotwires located in the coordinate directions and located very near to the inducer trailing edge, has led to valuable information on the blade-to-blade variation of all the velocity and turbulence intensity components at that location. Major conclusions from these measurements are:

1) The radial velocities obtained from the hotwire measurements are found to be of the same order of magnitude as the axial velocities throughout the flow passage.

2) The blade-to-blade variation of axial, tangential and radial velocities measured at the exit by means of the hotwire probes are found to be nearly uniform. Similarly, the blade-to-blade variation of the relative velocities derived from the hotwire data is found to be nearly uniform. This is probably due to considerable wake diffusion that takes place between the trailing edge and the hotwire measuring station.

3) The exit turbulence intensities are found to be rather uniform in the entire flow passage. The magnitudes of the turbulence intensities also reveal the highly turbulent nature of the flow in inducers.

In an axial flow inducer, the interaction between the pressure surface and suction surface boundary layers result in an extremely

complex flow, especially near the outer half of the blade span. Since

these interaction effects are very complex, experimental investigation

assumes a very important role in this program. These effects are being

studied at The Pennsylvania State University in a helical channel,

specifically designed and fully instrumented for this purpose. The

channel consists of constant-thickness blades of zero camber. It is

proposed to carry out experiments at zero and other incidences. Details

of the experimental program, the Reynolds equation and velocity profiles

analysis valid for this flow and some preliminary measurements are given

in Ref. 2.

## Methods and Means of Investigation

As discussed in the previous sections, the three-dimensional viscid

and inviscid effects of the inducer fluid flow makes meaningful

predictions extremely difficult. An existing numerical procedure to

simultaneously solve the three-dimensional equations of inviscid motion

and continuity, developed by Cooper and Bosch (Ref. 4), is first utilized

in an attempt to obtain the inviscid solution of the inducer flow field.

The inducer geometry used for this numerical analysis is shown in Fig. 2.

The incorporation of the dominant viscous terms into the equations of

motion of Ref. 4 is then attempted. Use is made of empirically derived

values of blade skin friction coefficient to derive the necessary

viscous terms in the equation. The exact equations of motion, including

all of the viscous terms, are extremely difficult to solve numerically.

As an approximation, only the dominant viscous terms in the $r$-$\theta$-$z$

directions are considered.
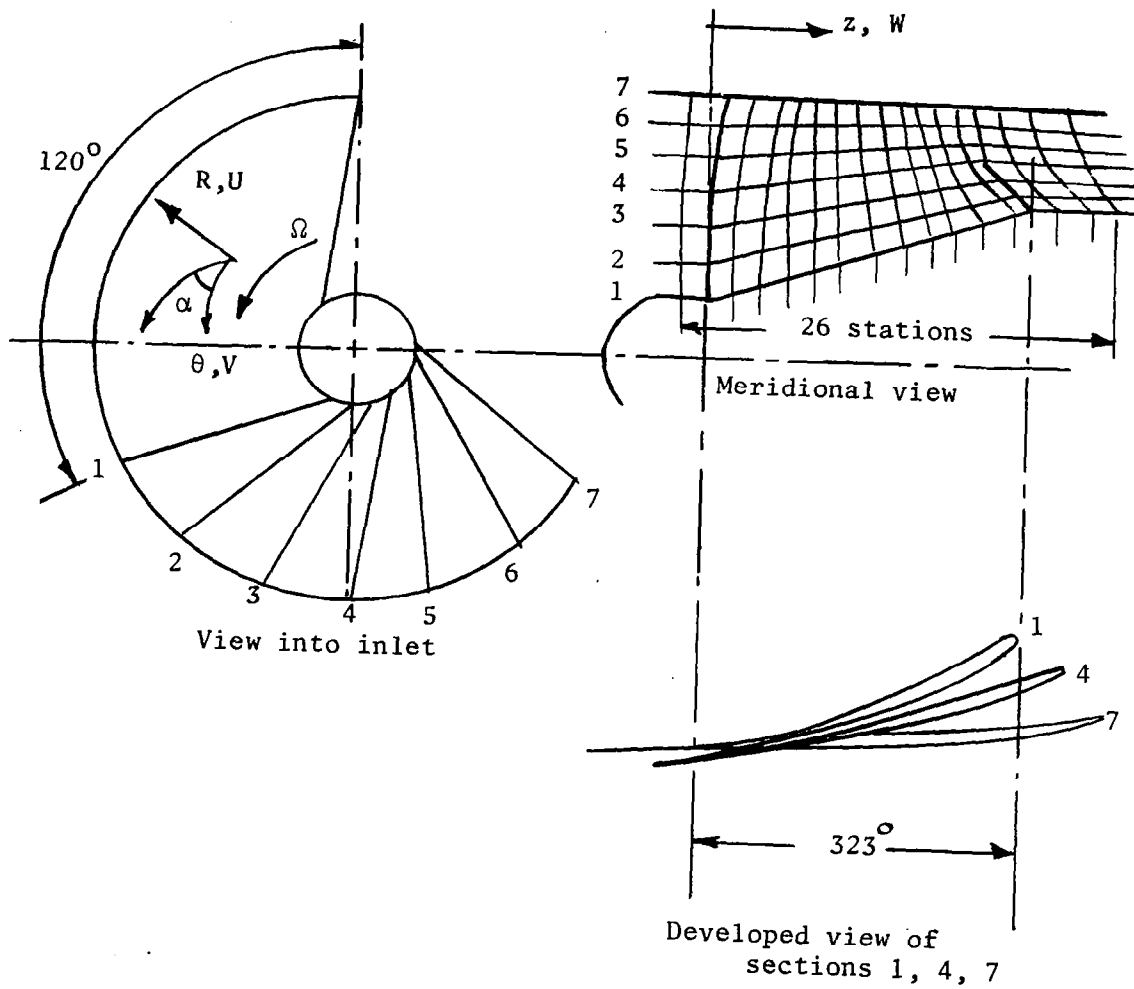
Figure 2. Inducer Geometry for Numerical Analysis.

Because of the iterative nature of the solution to the exact equations, a large amount of computer time and computer storage is usually required. In an attempt to reduce the solution convergence time, a method of initially determining input variables needed by the exact solution program is derived.

Extensive measurements inside the blade passages are carried out not only to confirm the validity of the flow predictions, but also to gain a better understanding of the secondary motions of the flow. Extensive blade static pressure distributions are measured and compared with theory and a thorough survey of limiting streamline angles on the blade surface is also presented. A triaxial hotwire anemometer is used for measuring the three components of velocity, turbulence intensity and turbulence stress within the rotating inducer blade passage. The techniques used in this method are described in detail in a later section. The location of the experimental flow measuring stations are given in Fig. 3. Comparison of experimental results with results of the present theoretical analysis and results of previous investigations are discussed.

The three-bladed inducer was used in the experimental and theoretical investigations of this thesis.

Appreciation is expressed to E. Jordan and A. K. Anand for their assistance in instrumentation and measurements.

Axial Measuring Station
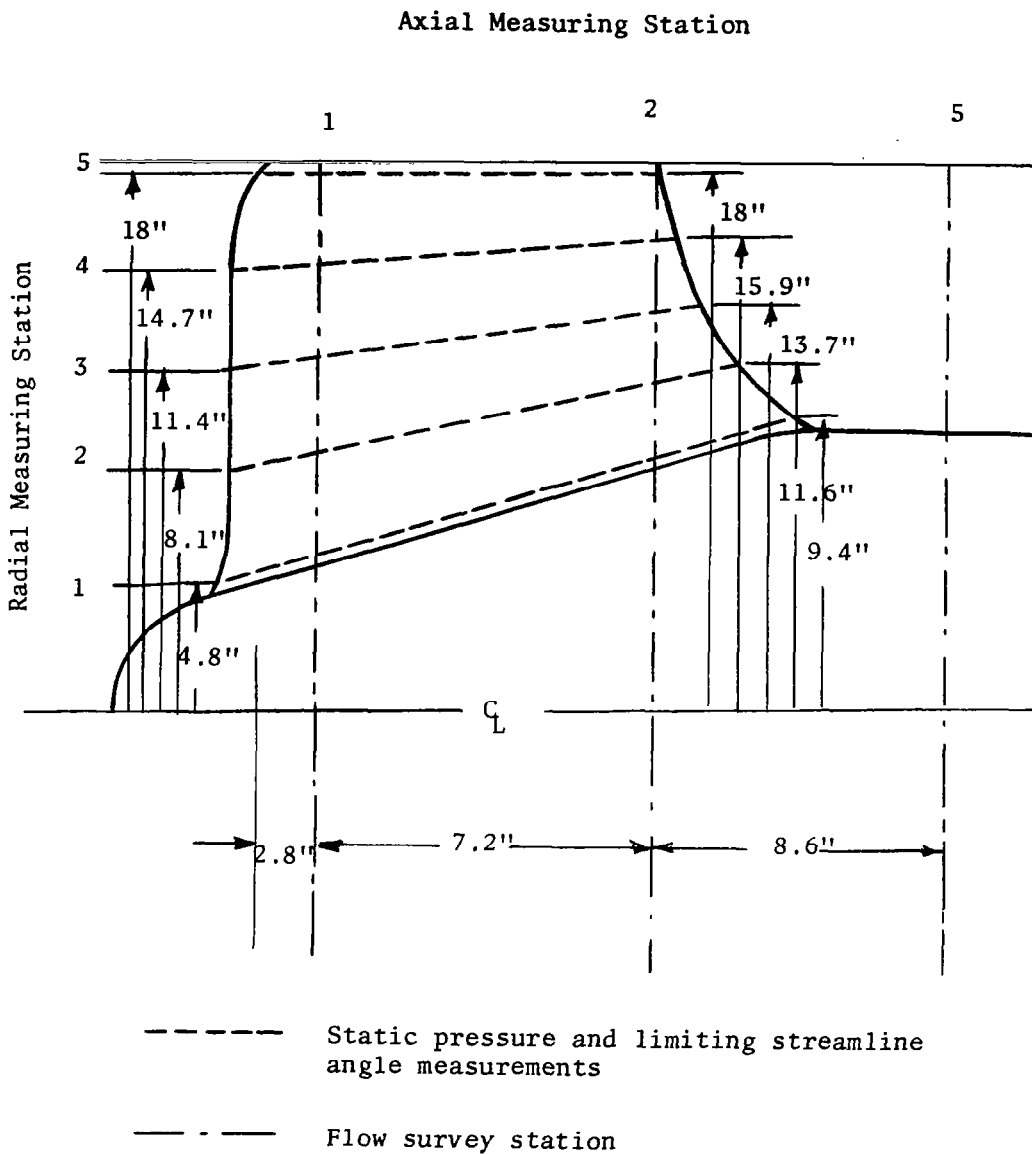


Figure 3.  Location of Experimental Flow Measuring Stations.

# THEORETICAL ANALYSIS

A thorough knowledge of all significant inviscid effects (blade blockage, flow turning, finite hub/tip ratio, etc.) and viscid effects (boundary layer growth, energy dissipation, etc.) is essential in the accurate prediction of the flow in all turbomachinery. Relevant to this, the availability of modern computers with large storage capacities and fast computation times greatly enhance the possibility of numerically solving the complete equations of motion. One of the early investigations in this area was made by Cooper and Bosch (Ref. 4) for the case of the three-dimensional inviscid flow through axial flow inducers. Application of this method of analysis to the Penn State inducer is given in this chapter. In addition, this chapter describes modifications to the Cooper-Bosch method which have been attempted to help reduce convergence time of the solution and provide a viscid solution capability based on empirically determined blade skin friction coefficients. A method of initializing the blade flow parameters as input to the Cooper-Bosch method has also been attempted in a search for a faster convergence to the solution.

## Exact Inviscid Analysis

As mentioned above, Cooper and Bosch have developed a method of obtaining the exact inviscid solution of the inducer flow field. This three-dimensional analysis employs an iterative numerical procedure to solve the equations of motion expressed in finite-difference form.

General Equations and Method

The nonlinear partial differential equations governing the flow in a rotating cylindrical coordinate system $r$, $\theta$, $z$ are:

r momentum: 
$$\frac{g_o}{\rho}\frac{\partial p}{\partial r} + U\frac{\partial U}{\partial r} + \frac{V}{r}\frac{\partial U}{\partial \theta} + W\frac{\partial U}{\partial z} - \frac{1}{r}(V + r\Omega)^2 + F_r = 0 \qquad (2)$$

$\theta$ momentum: 
$$\frac{g_o}{\rho r}\frac{\partial p}{\partial \theta} + U\frac{\partial V}{\partial r} + \frac{V}{r}\frac{\partial V}{\partial \theta} + W\frac{\partial V}{\partial z} + \frac{UV}{r} + 2U\Omega + F_\theta = 0 \qquad (3)$$

z momentum: 
$$\frac{g_o}{\rho}\frac{\partial p}{\partial z} + U\frac{\partial W}{\partial r} + \frac{V}{r}\frac{\partial W}{\partial \theta} + W\frac{\partial W}{\partial z} + F_z = 0 \qquad (4)$$

continuity: 
$$\frac{U}{r} + \frac{\partial U}{\partial r} + \frac{1}{r}\frac{\partial V}{\partial \theta} + \frac{\partial W}{\partial z} = 0 \qquad (5)$$

Where W, V, U are relative velocities in the axial, tangential and radial directions respectively (Fig. 2). $F_r$, $F_\theta$ and $F_z$ are the components of the body forces including viscous terms, and are zero for the inviscid case considered in this section. In the Cooper-Bosch method, the above equations are rearranged to give residuals which are reduced to zero by a relaxation procedure. The total residual (RT) of one relaxation cycle is calculated by

$$RT = \sum_{i=1}^{IMAX}\sum_{j=1}^{JMAX}\sum_{k=1}^{KMAX}[(R1)^2 + (R2)^2 + (R3)^2 + (R4)^2]_{i,j,k} \qquad (6)$$

where R1, R2, R3 and R4 are the residuals calculated for the three momentum equations (2-4) and the continuity equation (5), and IMAX, JMAX and KMAX are the number of grid stations in the radial, tangential and axial directions which are used in the numerical analysis.

18

From this, the total RMS (root mean square) residual is defined as

$$RMS = \sqrt{\frac{(RT)^2}{4 \cdot (IMAX) \cdot (JMAX) \cdot (KMAX)}} \qquad (7)$$

and is thus a measure of the degree of convergence between the iterated solution and the exact solution.

The application of this method to the solution of the flow in the three-bladed Penn State inducer has been reported by Poncet and Lakshminarayana in Ref. 20.

In applying this method to the Penn State inducer, the flow is assumed to be incompressible, and a grid of 7 x 7 x 26 is chosen to represent the blade passage. The flow geometry is shown in Fig. 2.

The boundary condition to be satisfied on the hub, annulus walls and the blade surfaces is $\vec{Q}_R \cdot \vec{n} = 0$, where $\vec{n}$ is the direction normal to the channel boundaries and $\vec{Q}_R$ is the total relative velocity.

The first of the 26 axial stations corresponds to the upstream through-flow boundary where the initial conditions are applied. For the boundary value problem to be consistent, these initial upstream conditions must specify the three components of velocity and pressure, and the tangential velocity on the second axial station (which thus defines the swirl at the inlet of the inducer).

The last four axial stations correspond to the downstream flow-through boundary, and extend to about one-fifth of the chord length downstream of the trailing edge. With $\vec{Q}_R \cdot \vec{n} = 0$ to be satisfied on these stagnation stream surfaces, the set of boundary conditions for the problem is complete.

The Cooper-Bosch program has been suitably modified for use on the high speed digital computer system at The Pennsylvania State University. However, because of the iterative techniques employed in the Cooper-Bosch program, a large amount of computer time is usually required to converge to a satisfactory solution. For increased efficiency, the program has been compiled under a Fortran IV H level optimization procedure which reduces the time required for repetitive calculations, and production runs were submitted using the resulting object card deck. Output results from the computer program were placed onto 9 track, 1600 BPI (bits per inch) magnetic computer tape for future accessibility.

Initial Input to the Exact Solution Program

An investigation of available mathematical methods to solve the four simultaneous nonlinear partial differential equations governing the inducer flow revealed that there was no alternate method which would solve the equations more efficiently or effectively with a minimum of programming effort than the method described in Ref. 4. The next available approach for the speedier solution of the governing flow equations is the optimization of the input parameters of velocity and pressure which would allow faster convergence to the three-dimensional solution. Cooper and Bosch have derived an approximate solution in Ref. 4 to be used as an initial input to the exact program. This method derives the blade-to-blade average quantities using axisymmetric equations, then uses these quantities in a blade-to-blade solution of an integrated form of the scalar momentum equation in the tangential direction. The flow parameters derived by this method were used in

Ref. 20. However, an alternative method of developing the initial input flow parameters has been attempted in the present analysis, and is discussed in detail in the following two sections.

Douglas-Neumann Analysis.- The initial estimation for the velocity and static pressure distribution throughout the inducer flow passage is calculated by the two-dimensional Douglas-Neumann program described in detail in Ref. 5. The technique employed by the Neumann program to solve a particular fluid flow problem is to use source distributions of appropriate strength on the surface of the blade profile in such a way that the flow normal to the surface of the body is either zero or prescribed. When the Neumann boundary condition is applied, an integral equation in source strength $\xi$ is obtained

$$-\vec{C}_\infty \cdot \vec{n} = \xi(s) + \int_{body} \xi(x)A(x,s)\ dx \qquad (8)$$

where $A(x,s) = \vec{n} \cdot \vec{C}(x,s)$ and $C_\infty$ is the onset flow. $\vec{C}(x,s)$ is the velocity at a surface point s due to a unit source at x. The solution for the general case of a lifting cascade at any angle of attack is calculated by superposition of three "basic flows" in such a way that the correct angle of attack is obtained and the Kutta condition is satisfied. The "basic" flows are: flow at zero angle of attack, flow at $90^\circ$ angle of attack, and circulatory flow for each cascade. Super-position of solutions is possible because the potential equation is linear and the boundary condition on the cascade blade is homogeneous.

In the Douglas-Neumann results, velocities and static pressure
coefficients are normalized with the modulus of the average onset flow
velocity

$$\frac{C_{inlet} + C_{exit}}{2} \tag{9}$$

The listing of the Douglas-Neumann program is given in Ref. 5.

Quasi-Three-Dimensional Modification.- The investigation of the
flow around an isolated airfoil in a contracting or diverging stream is
presented in Ref. 13. This analysis provides a simple method of modi-
fying the two-dimensional Douglas-Neumann flow solutions to account for
the three-dimensional effect of the converging or diverging streamlines.
An expression for static pressure coefficient on the airfoil surface is
derived as a function of channel slope, two-dimensional static pressure
coefficient, and the Fourier coefficients of the blade profile. The
analysis utilizes thin airfoil theory approximations and assumes that
thickness effects are the same as in plane flow. The mean flow is
assumed to be inviscid, steady, and incompressible, and the variation
of channel height is assumed to vary linearly from leading to trailing
edge while the length of the contracting section is assumed to be the
same as the axial projection of the blade. In the present application,
the expression for static pressure coefficient has been modified in an
attempt to represent the flow about a row of two-dimensional infinite
cascades. This quasi-three-dimensional approach has been applied to
the two-dimensional results obtained from the Douglas-Neumann analysis
for the Penn State inducer. The effect of the converging channel as
determined by the above analysis on the Neumann solution for the Penn

State inducer is essentially to decrease the blade static pressure
near the trailing edge.

A comparison of the radial variation of axial and tangential
velocities calculated by the above method with the experimental results
of Ref. 20 shows close agreement (Fig. 4). The agreement between the
measured tangential velocity and inviscid prediction may be fortuitious,
since the axial velocity predicted at the same location is considerably
different from the measured values.

Using the input parameters of velocity and pressure derived from
the preceeding analysis results in a lower total RMS (root mean square)
residual than with the previous method of initializing the input
variables. As an example, the final RMS residual for the inviscid
results of Ref. 20 was 0.12450 after 68 relaxation cycles, whereas a
similar value is obtained using the present analysis in 10 relaxation
cycles. This amounts to a considerable saving in computer time.
Twenty-five iteration cycles has reduced the RMS residual to 0.10579,
indicating that a faster convergence to the solution should be possible.
Further investigation should be carried out to confirm the effectiveness
of the input analysis as an alternative to the Cooper-Bosch approximate
solution method.

In a further attempt to decrease the convergence time, the exit
flow angle was allowed to change depending upon the tangential and axial
velocities calculated at the inducer trailing edge. Since the exact
downstream boundaries are not known in this type of problem, it was
hoped that by allowing the downstream boundaries to adjust themselves
and thereby unload the blade trailing edge, a more exact definition of
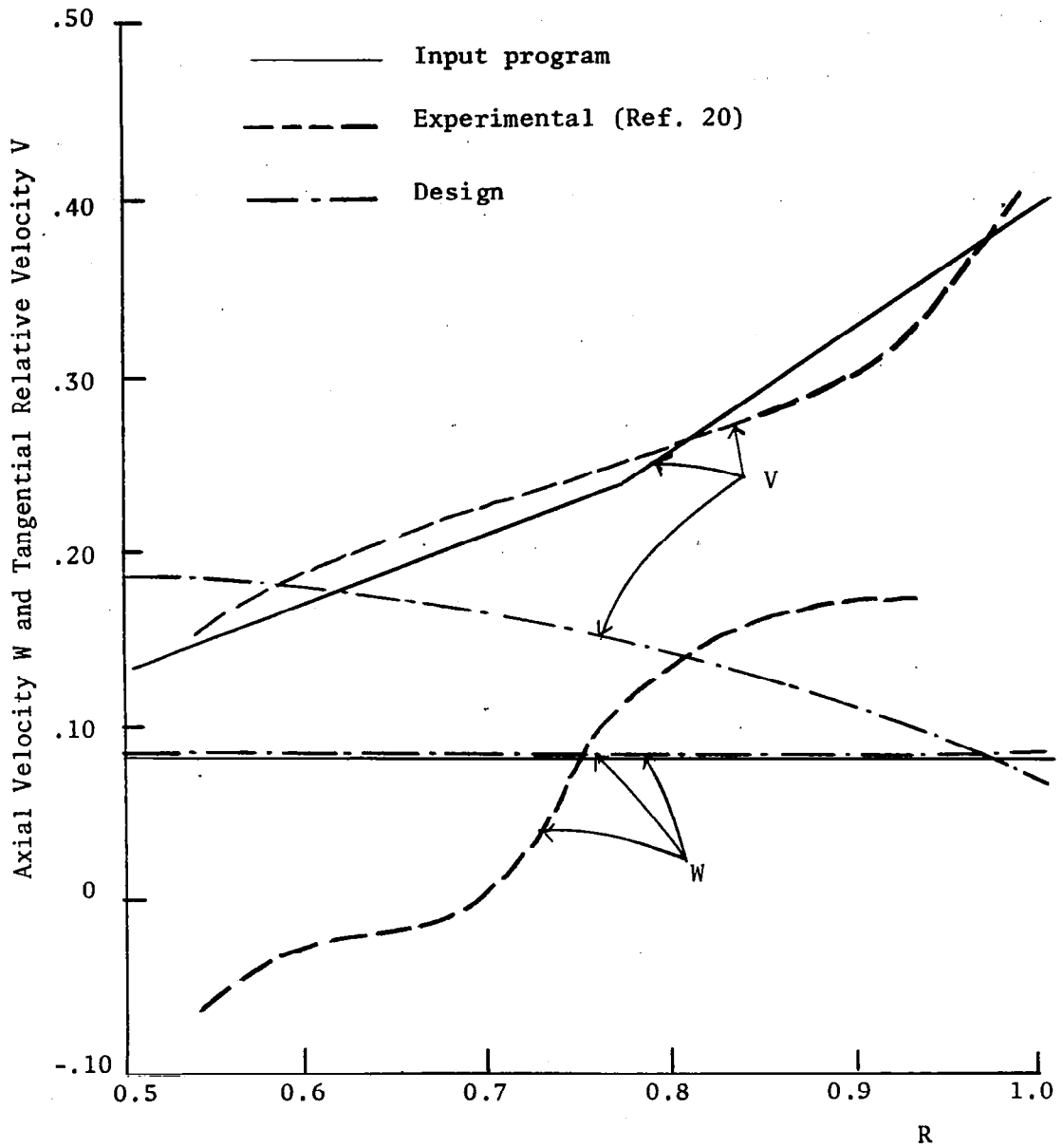
Figure 4.   Input Data Comparison at Axial Flow Survey Station 5

the downstream streamlines would result in lower RMS residuals. Cooper and Bosch suggest a similar technique as a means of reducing RMS residuals in their recommendations for future work.

Since the extension of the stagnation stream surfaces downstream have been constructed to be uniformly periodic with a spacing of $2\pi/N$ (N being the number of blades), the values of velocity and pressure at the downstream tangential channel boundaries should be equal. This condition is applied at the blade trailing edge after each iteration cycle. If the pressure and suction surface parameters differ with each other at the trailing edge grid point, the average value is used in the residual calculations. If the axial and/or tangential velocities at the trailing edge diverge significantly from the design values during the iteration process, then the flow exit angle, defined by $\beta = \tan^{-1}\frac{V}{W}$ at the trailing edge, is recalculated and is used to redefine the downstream stagnation stream surfaces. This method also has the advantage of automatically forcing the Kutta-Joukowski condition for the blade pressure distribution to be satisfied. Changes made to the original Cooper-Bosch program can be seen in Appendix B and are concentrated in subroutine "MAIN". A flow chart diagram of the Cooper-Bosch program, including the modification discussed above, is given in Appendix A.

## Viscid Analysis

In addition to the attempts to improve the convergence of the exact inviscid solution, a method of incorporating viscid effects into the governing equations of motion has also been investigated.

General Equations and Theoretical Method

The viscid equations of motion are:

r momentum:

$$\frac{1}{\rho} \frac{\partial p}{\partial r} + \frac{V}{r} \frac{\partial U}{\partial \theta} + U \frac{\partial U}{\partial r} + W \frac{\partial U}{\partial z} - \frac{1}{r} (V + r\Omega)^2 = \frac{1}{\rho} [\frac{\partial \tau_{r\theta}}{r\partial \theta} + \frac{\partial \tau_{rz}}{\partial z} + \frac{\partial \sigma_{rr}}{\partial r} + \frac{(\sigma_{rr} - \sigma_{\theta\theta})}{r}]$$

(10)

θ momentum:

$$\frac{1}{\rho r} \frac{\partial p}{\partial \theta} + \frac{V}{r} \frac{\partial V}{\partial \theta} + U \frac{\partial V}{\partial r} + W \frac{\partial W}{\partial z} + \frac{UV}{r} + 2\Omega U = \frac{1}{\rho} [\frac{\partial \sigma_{\theta\theta}}{r\partial \theta} + \frac{\partial \tau_{\theta z}}{\partial z} + \frac{\partial \tau_{\theta r}}{\partial r} + \frac{2}{r} \tau_{\theta r}]$$

(11)

z momentum:

$$\frac{1}{\rho} \frac{\partial p}{\partial z} + \frac{V}{r} \frac{\partial W}{\partial \theta} + U \frac{\partial W}{\partial r} + W \frac{\partial W}{\partial z} = \frac{1}{\rho} [\frac{\partial \tau_{z\theta}}{r\partial \theta} + \frac{\partial \sigma_{zz}}{\partial z} + \frac{\partial \tau_{rz}}{\partial r} + \frac{\tau_{rz}}{r}]$$  (12)

continuity:

$$\frac{U}{r} + \frac{\partial U}{\partial r} + \frac{1}{r} \frac{\partial V}{\partial \theta} + \frac{\partial W}{\partial z} = 0$$  (13)

where

$$\sigma_{\theta\theta} = - \overline{v^2} \ , \ \tau_{\theta z} = - \overline{vw} = \tau_{z\theta}$$

$$\sigma_{rr} = - \overline{u^2} \ , \ \tau_{rz} = - \overline{uw} = \tau_{zr}$$

$$\sigma_{zz} = - \overline{w^2} \ , \ \tau_{\theta r} = - \overline{vu} = \tau_{r\theta}$$

Molecular viscosity terms have been neglected in these equations.

26

Comparing these equations with the momentum equations used by Cooper and Bosch, the following expressions for FR, FT, and FZ (the exact program variables for viscous loss terms) can be given as:

$$FR = -\frac{1}{\rho}\left[\frac{\partial \tau_{r\theta}}{r\partial\theta} + \frac{\partial \tau_{rz}}{\partial z} + \frac{\partial \sigma_{rr}}{\partial r} + \frac{(\sigma_{rr} - \sigma_{\theta\theta})}{r}\right] \qquad (14)$$

$$FT = -\frac{1}{\rho}\left[\frac{\partial \sigma_{\theta\theta}}{r\partial\theta} + \frac{\partial \tau_{\theta z}}{\partial z} + \frac{\partial \tau_{\theta r}}{\partial r} + \frac{2}{r}\tau_{\theta r}\right] \qquad (15)$$

$$FZ = -\frac{1}{\rho}\left[\frac{\partial \tau_{z\theta}}{r\partial\theta} + \frac{\partial \sigma_{zz}}{\partial z} + \frac{\partial \tau_{rz}}{\partial r} + \frac{\tau_{rz}}{r}\right] \qquad (16)$$

Since the stagger angle is very large, these viscous terms can be approximated by retaining the dominant terms as well as neglecting the normal shear stresses, resulting in:

$$FR = -\frac{1}{\rho}\frac{\partial \tau_{rz}}{\partial z} \qquad (17)$$

$$FT = -\frac{1}{\rho}\frac{\partial \tau_{\theta z}}{\partial z} \qquad (18)$$

$$FZ = -\frac{1}{\rho}\frac{\partial \tau_{z\theta}}{r\partial\theta} \qquad (19)$$

The distribution of shear stress is assumed to be linear across the flow passage from pressure surface to suction surface. The values of wall shear stresses are assumed to be known from previous experimentation. Skin friction coefficient $C_f$ for a four-blade flat plate helical channel is given in Ref. 2. The results, summarized in Fig. 5, are considered to be valid for the three-blade inducer under consideration. Interpolation of the curves in Fig. 5 for a given blade surface

27
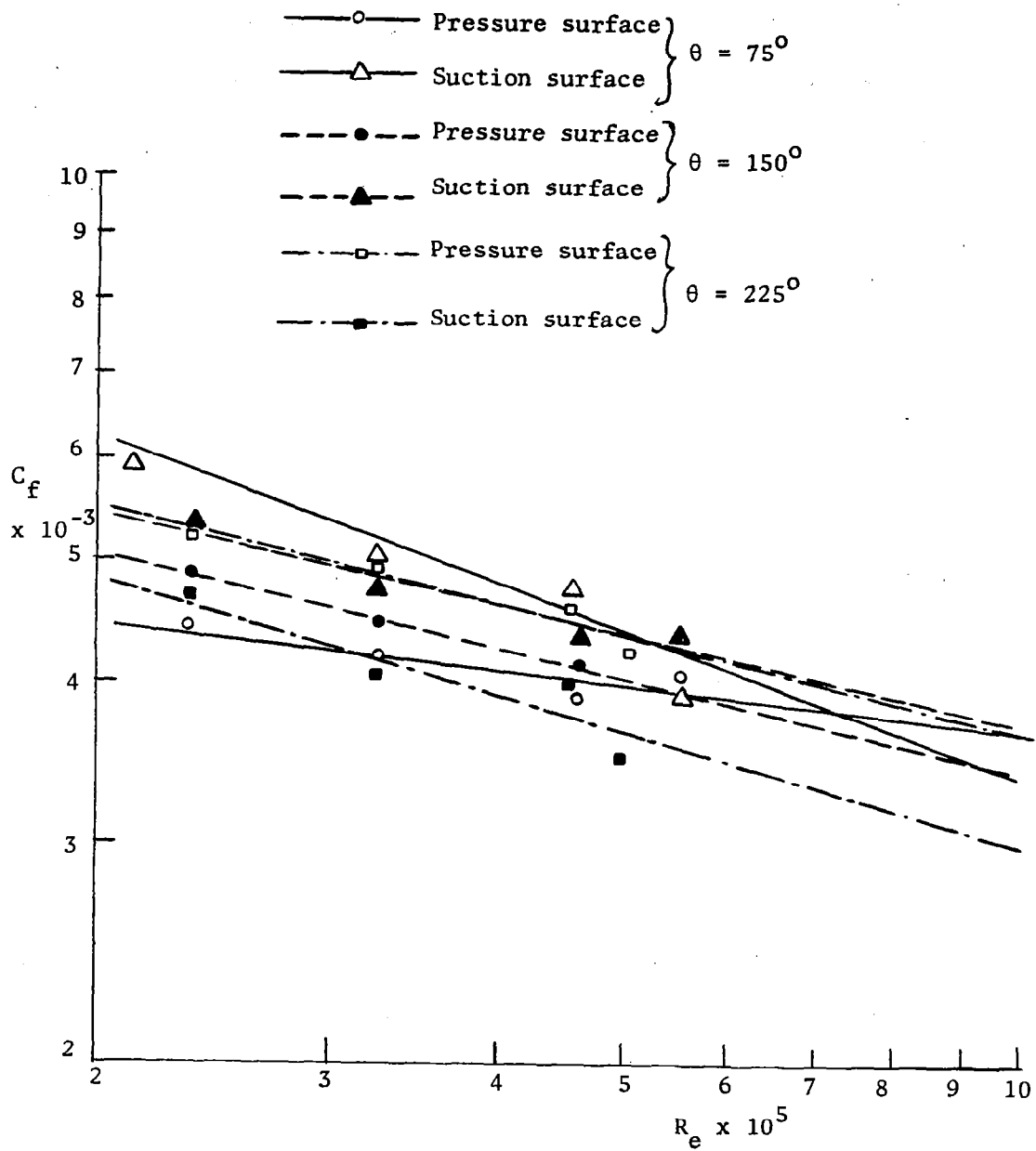


Figure 5. Skin Friction Coefficient vs. Reynolds Number

grid location under consideration gives a value of wall shear stress $\tau_w = C_f \cdot \frac{1}{2} \rho \bar{Q}_R^2$ for the appropriate Reynolds number $R_e = \bar{Q}_R \cdot r / \nu$ of the flow at that point, where $\bar{Q}_R$ is the average relative velocity across the flow passage as derived by the Cooper-Bosch relaxation procedure. Calculation of $\tau$ at each grid location within the flow passage allows the derivatives of equations 17-19 to be calculated by finite-difference methods.

An additional requirement placed on the viscid analysis is to satisfy the viscid boundary condition which requires that all components of velocity are zero at the blade surface.

The changes to the original Cooper and Bosch exact program necessitated by the inclusion of the viscous loss terms are made in subroutines "MAIN", "DLOSS" and "RESID". Flow chart diagrams for the modified subroutines of the Cooper-Bosch program are given in Appendix A. A complete Fortran listing of the modified Cooper-Bosch program is given in Appendix B.


Input and Solution

The input variables and formats for the modified viscid analysis program are identical to the original Cooper-Bosch program, with the exception of including a set of curves to define blade skin friction coefficient $(C_f)$ vs. Reynolds number $(R_e)$ for various reference tangential locations throughout the inducer channel. Input values are taken from log-log plots similar to that shown in Fig. 5. Straight line approximations for the reference data are required. A definition for each of the additional input quantities follows. For the exact format

in which these parameters must be coded, consult the program Fortran
listing in Appendix B.

NCURVE:             Number of $C_f$ vs. $R_e$ reference curves used as input.  Each
                    curve must correspond to a specific blade tangential
                    location.  Maximum of 3, minimum of 2.

THETA(I):           Tangential location, in degrees from leading edge, where
                    a specific $C_f$ vs. $R_e$ curve applies.  The array index (I)
                    increases from 1 to NCURVE, proceeding from leading edge
                    to trailing edge.

REREF1(I),

REREF2(I):          Minimum and maximum values respectively of $R_e$ used in
                    straight line approximation of $C_f$ vs. $R_e$ curve.

CFREFP(1,I),

CFREFP(2,I):        $C_f$ values corresponding to REREF1(I) and REREF2(I)
                    respectively on the blade pressure surface.

CFREFS(1,I),

CFREFS(2,I):        $C_f$ values corresponding to REREF1(I) and REREF2(I)
                    respectively on the blade suction surface.

The viscid modifications which have been discussed are activated in the computer program when the appropriate value of fluid kinematic viscosity is used as an input parameter.  If zero viscosity is coded, the modified program will automatically revert to an inviscid analysis as represented in the original Cooper-Bosch program.  Preliminary running of the modified viscid program indicates an increase in computer time of approximately two to three times more than a corresponding inviscid analysis run.  This increase in computation time is due to the calculation of the viscous loss terms FR, FT and FZ at each grid point location throughout the duration of one relaxation cycle, which may involve several thousand iterations of the flow parameters in order to reduce the RMS residual from the previous cycle.  The efficiency of the computer programming can certainly be improved upon in future study.

Comparison of the results of the Cooper-Bosch inviscid and viscid analyses and their relationship to experimental measurements are discussed in a later chapter.

EXPERIMENTAL EQUIPMENT, METHODS AND TECHNIQUES

The primary goal of performing the following experimental program was to investigate the flow characteristics such as velocity, turbulence characteristics and static pressure of the relative flow inside a three-bladed inducer. The importance of this experimental data for a better understanding and prediction of the flow has been mentioned in the introduction.

A secondary goal was the determination of the effectiveness of the triaxial rotating hotwire as a method of measuring mean and fluctuating velocities and turbulence stresses within the inducer blade passage.

## Three-Bladed Inducer

The experimental investigation was performed on a three-foot diameter axial flow inducer with three equally spaced blades. The test facility is pictured in Fig. 1a. Design of the blades is by the mean streamline method of Wislicenus (Ref. 25). The inducer was operated at 450 rpm, which was determined to an accuracy of 0.1 rpm by means of a photocell circuit with rotating calibrated disk and displayed on an electronic counter. Important parameters of the inducer are as follows:

| | |
|---|---|
| Number of Blades | 3 |
| Hub/Tip Ratio at Outlet | 0.50 |
| Hub/Tip Ratio at Inlet | 0.25 |
| Radial Clearance | 0.0625" |
| Inlet Flow Coefficient (Design) | 0.065 |
| Blade Chord at $r/r_t = 1.0$ | 82.96" |
| Blade Chord at $r/r_t = 0.75$ | 63.18" |

Blade Chord at $r/r_t$ = 0.50                    49.94"

Solidity at $r/r_t$ = 1.0                         2.15

Solidity at $r/r_t$ = 0.75                        2.21

Solidity at $r/r_t$ = 0.50                        2.61

Reynolds Number Based on Tip Radius              $7.0 \times 10^5$

The design values of blade and flow angles at inducer inlet and exit
are given in Fig. 1b.

The use of the three-bladed inducer for the continued experimental
investigation defined in this report is a result of conclusions reached
by prior investigations described in Ref. 20; namely, it has appreciably
better performance than a similar four-bladed inducer tested at the same
flow coefficient.

Blade static pressure measurements were obtained with the use of
hypodermic steel tubing of .063" ID imbedded in the blade at ten
separate pressure and suction surface locations.  The pressure measure-
ments at each location were carried out at five radial stations by
utilizing .063" diameter taps drilled at equally-spaced intervals from
tip to hub.  The approximate radial locations of the pressure taps are
shown in Fig. 3 and the actual experimental radial and chordwise locations
of the pressure taps are given in Table 1 and Table 2 respectively.

Velocity and turbulence measurement stations within the blade
passage have been previously used (Ref. 20) and were constructed by
cutting tangential slots in the hub wall at the locations shown in
Fig. 3.

The inducer was statically and dynamically balanced at facilities
in the Garfield Thomas Water Tunnel of The Pennsylvania State
University.

Table 1.  Radial Location of Blade Static

Pressure Measurement Stations*

| Tangential Measurement Station | Radial Measurement Station | | | | |
|---|---|---|---|---|---|
| | 1 | 2 | 3 | 4 | 5 |
| **Pressure Surface** 1 | .291 | .466 | .644 | .815 | .985 |
| 2 | .295 | .466 | .637 | .808 | .985 |
| 3 | .322 | .479 | .654 | .819 | .985 |
| 4 | .342 | .500 | .664 | .823 | .985 |
| 5 | .356 | .514 | .671 | .823 | .985 |
| 6 | .370 | .521 | .678 | .829 | .985 |
| 7 | .390 | .541 | .689 | .835 | .985 |
| 8 | .411 | .555 | .699 | .842 | .985 |
| 9 | .438 | .575 | .719 | .849 | .985 |
| 10 | .473 | .609 | .726 | .863 | .985 |
| **Suction Surface** 1 | .288 | .466 | .640 | .815 | .985 |
| 2 | .301 | .479 | .644 | .823 | .985 |
| 3 | .322 | .486 | .658 | .823 | .985 |
| 4 | .342 | .500 | .664 | .823 | .985 |
| 5 | .356 | .514 | .671 | .829 | .985 |
| 6 | .370 | .527 | .678 | .835 | .985 |
| 7 | .390 | .541 | .685 | .835 | .985 |
| 8 | .397 | .548 | .692 | .835 | .985 |
| 9 | .425 | .555 | .699 | .835 | .980 |
| 10 | .435 | .561 | .692 | .842 | .983 |

*Radial locations nondimensionalized as $r/r_t$.

Table 2.  Chordwise Location of Blade Static

Pressure Measurement Stations*

| Tangential Measurement Station | | Radial Measurement Station | | | | |
|---|---|---|---|---|---|---|
| | | 1 | 2 | 3 | 4 | 5 |
| Pressure Surface | 1 | 11.3 | 8.9 | 6.5 | 5.7 | 4.9 |
| | 2 | 15.5 | 14.3 | 13.0 | 12.0 | 11.0 |
| | 3 | 24.0 | 24.0 | 24.0 | 23.8 | 23.5 |
| | 4 | 34.0 | 36.0 | 38.0 | 38.0 | 38.0 |
| | 5 | 44.0 | 48.0 | 52.0 | 52.3 | 52.5 |
| | 6 | 51.0 | 55.5 | 60.0 | 60.5 | 61.0 |
| | 7 | 58.0 | 63.0 | 68.0 | 69.0 | 70.0 |
| | 8 | 66.0 | 72.0 | 78.0 | 78.5 | 79.0 |
| | 9 | 74.0 | 80.0 | 86.0 | 86.5 | 87.0 |
| | 10 | 82.0 | 88.0 | 94.0 | 95.0 | 96.0 |
| Suction Surface | 1 | 15.0 | 13.3 | 11.5 | 11.0 | 10.4 |
| | 2 | 19.5 | 18.9 | 18.2 | 17.6 | 17.0 |
| | 3 | 28.4 | 29.2 | 30.0 | 30.0 | 30.0 |
| | 4 | 45.0 | 47.5 | 50.0 | 50.5 | 51.0 |
| | 5 | 54.0 | 57.0 | 60.0 | 61.0 | 62.0 |
| | 6 | 62.0 | 66.0 | 70.0 | 70.8 | 71.5 |
| | 7 | 69.0 | 73.5 | 78.0 | 78.5 | 79.0 |
| | 8 | 75.0 | 80.5 | 86.0 | 86.0 | 86.0 |
| | 9 | 81.0 | 86.5 | 92.0 | 92.3 | 92.5 |
| | 10 | 85.0 | 91.0 | 97.0 | 97.0 | 97.0 |

*Chordwise locations are expressed as percent chord from blade leading edge.

## Blade Static Pressure Measurement

An extensive experimental investigation of the blade static pressure distribution has been undertaken to help provide a check on prior theoretical analyses and useful information for future theoretical development.

## Equipment Used

A schematic diagram of the blade static pressure test setup is shown in Fig. 6. The equipment used to measure the blade static pressure distribution of the three-bladed inducer is as follows:

Scanivalve.- The scanivalve, a scanning type pressure sampling valve for measuring multiple pressures, was mounted in the rotating hub section of the inducer. The scanivalve incorporates a fluid wafer switch for time-sharing one pressure lead with up to twenty-four (24) unknown pressures, and is stepped by a rachet-geared solenoid. A solenoid controller used push button pulse length feedback and increased drawing voltage to step the solenoid driven scanivalve. The controller was equipped with a 24-division indicator dial which allowed monitoring of the static pressure station under consideration.

Three Channel Pressure Transfer Device (PTD).- A 3-channel pressure transfer device was used to transfer the static pressure measurements from the rotating reference frame of the three-bladed inducer to the stationary reference frame. Each channel was made airtight by the use of double-sealed ball bearings, and pressure leakage was prevented by use of O-rings and plastic sealers. The PTD was mounted on a stand
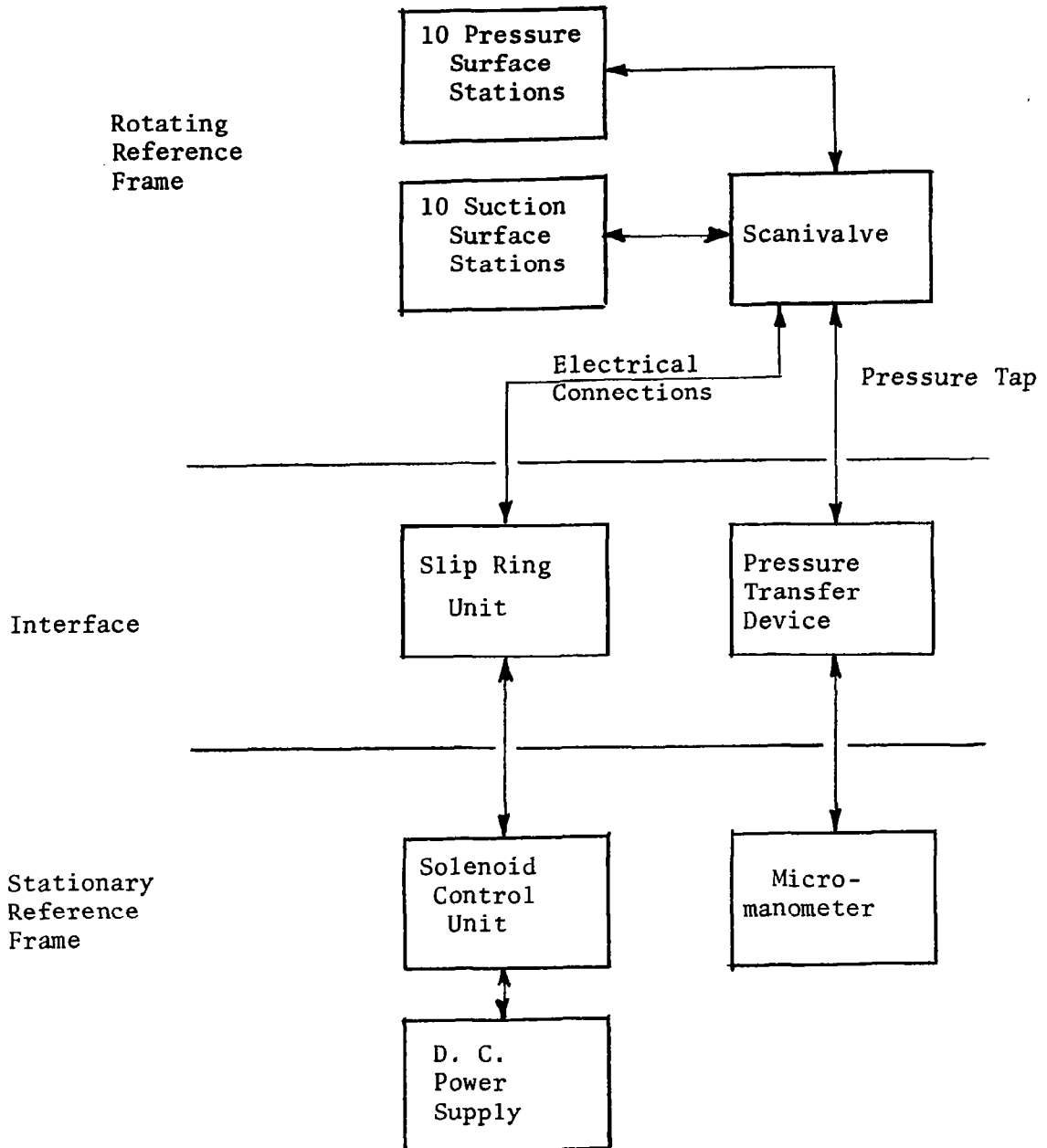
Figure 6.  Schematic Diagram of Blade Static Pressure Test Setup

outside the rotor assembly and was housed in a streamlined cowling to reduce any interference on the incoming flow.

Slip-Ring Unit.- An eight-channel slip-ring unit was used to conduct electrical signals from the stationary reference frame to the rotating reference frame of the scanivalve. Electrical continuity was provided by carbon brushes in contact with a rotating commutator aligned along the inducer's rotational axis. The slip-ring unit was mounted on the pressure transfer device, and all electrical and pressure connections were transferred through a hollow shaft and flexible couplings to the nose cone of the inducer.

Peripheral Equipment.- A transistorized 30 volt D.C. power supply was used to provide voltage to the scanivalve and solenoid controller units. A micromanometer graduated in 0.001" divisions was used to measure the blade static pressure.

Procedures and Techniques

Flexible vinyl tubing of 0.063" inside diameter was used to connect the ten suction and ten pressure surface stations to the available tubes on the scanivalve. The vinyl tubing was also used to connect the collection tubulation of the scanivalve to the measurement channel of the pressure transfer device. The manometer was similarly joined to this channel. Electrical connections from the scanivalve were transferred through the slip-ring unit to the solenoid controller and power supply. The blade static pressure measurement test setup is shown in Fig. 7.

38
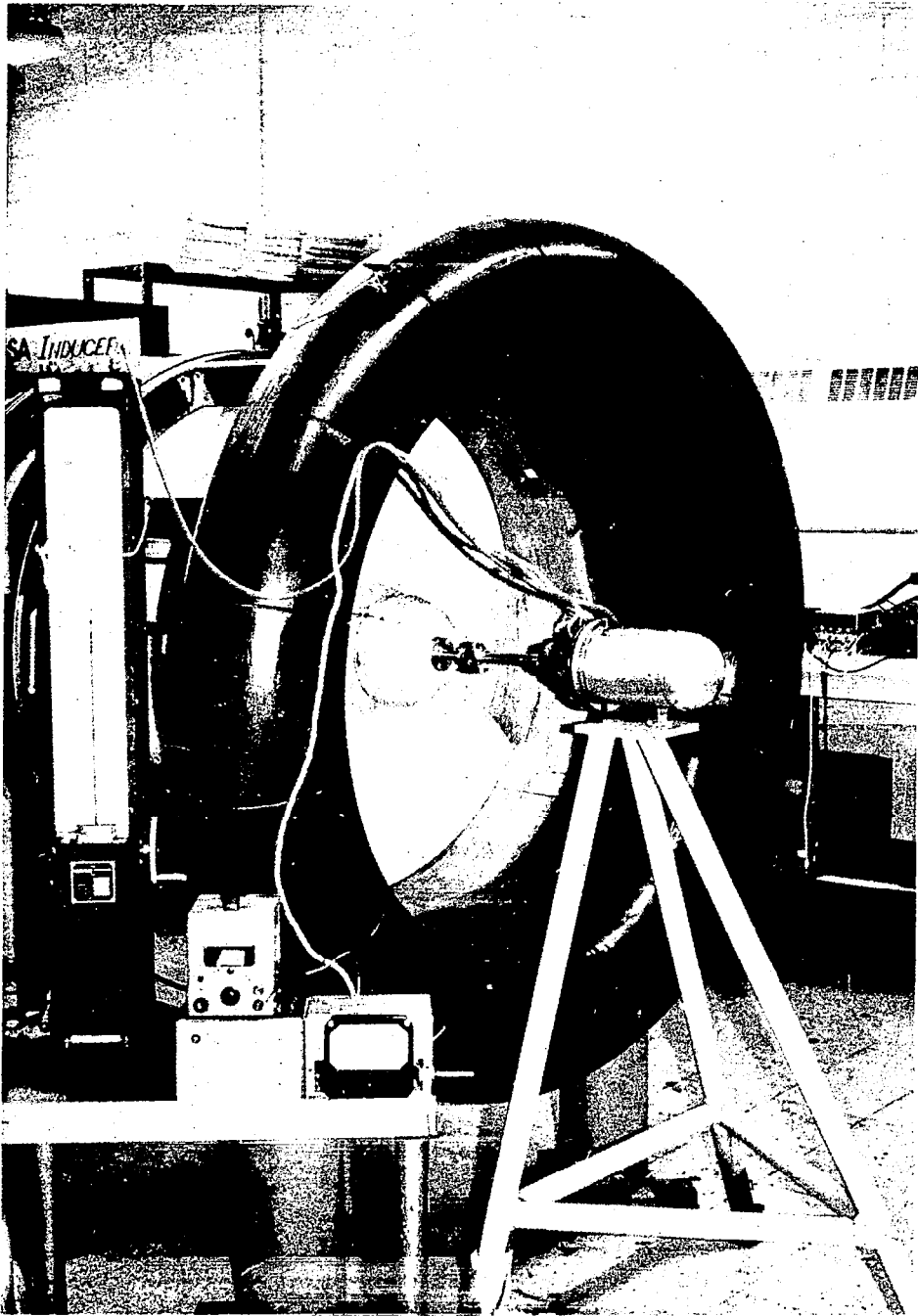


Figure 7.   Blade Static Pressure Test Setup

Masking tape was used to cover the radial pressure taps not under
consideration in a particular run.

Once the inducer speed was adjusted to 450 rpm, the static pressures
associated with the ten pressure and ten suction surface stations at a
particular radial passage location could be measured by stepping the
scanivalve through its range of operation. The dial on the solenoid
controller would indicate which station pressure was being measured.
Each step provided the blade static pressure of a different chordwise
station. Pressure readings were measured on the micromanometer to an
accuracy of 0.001".

Since the blade static pressure measurements were taken on the
rotating blade, it was necessary to apply a centrifugal force correction
to obtain the static head. If $h_m$ is the height of the water column
measured by the manometer, the actual static head is given by

$$h = \frac{\rho_m}{\rho} \, h_m + \frac{\Omega^2}{2g_o} \, (r^2 - r_o^2) \qquad (20)$$

where $\rho_m$ is the density of the manometer liquid, $r_o$ is the radius of the
rotating shaft used in the pressure transfer device, and $r$ is the radius
of the static pressure tap under consideration.

From this, the blade static pressure coefficient is defined by

$$\psi_s = \frac{2g_o h}{U_b^2} \qquad (21)$$

and is calculated for all pressure measurement stations.

## Blade Limiting Streamline Angle Measurement

The measurement of the blade limiting streamline angle ($\alpha$), which is the limiting position of the streamline as the blade surface is approached, is a further attempt to define the flow phenomena within the blade boundary layer, including nature and magnitude of the radial flows and the direction of the wall shear stress. The information gained will help establish the extent of three-dimensionality in the inducer flow and will be valuable in developing a viscid theory for the prediction of rotating boundary layer characteristics.

### Equipment, Procedures and Techniques

The blade measurement stations are identical to those used for the blade static pressure measurements of the previous section. The method and equipment for measurement are essentially the same as that used in Ref. 10. An ammonia transfer device (ATD) was placed inside the hub section along the axis of rotation. For a specific blade measurement station, the .063" flexible vinyl tubing associated with that location was attached to the ATD. Likewise, a thin strip of ozalid paper was attached radially on the blade surface adjacent to the measurement station.

Once the inducer had been rotated to the required 450 rpm, a small amount of ammonia gas was injected at low mass flow rate into the ATD and allowed to penetrate through the radial taps on the blade. The resulting ammonia trace on the ozalid paper was then measured to determine the limiting streamline angle. This procedure was repeated for all measurement stations.

### Three-Sensor Rotating Hotwire Measurement

Initial feasibility investigation into the use of the hotwire anemometer in the rotating flow passage of the three-blade Penn State inducer has been mentioned in Ref. 2. One problem experienced had been the inability of the relatively crude slip-ring unit to maintain the continuity of the hotwire circuitry. It did not allow suitable operation of the hotwire for extended periods of time to allow meaningful measurements to be obtained. The present study was an attempt to improve upon the accuracy and longevity of the initial investigation and prove the suitability of hotwires in the measurement of the relative mean and fluctuating velocities in a rotating environment.

Equipment Used

A schematic diagram of the rotating hotwire test setup is given in Fig. 8. A detailed description of the equipment used in the measurement of the relative mean and fluctuating velocities within the rotating passage of the three-bladed inducer follows:

Triple-Sensor Hotwire Probe.- A subminiature triaxial probe designed for boundary layer flows was used in the experimentation (Fig. 9). The wire is 3μm diameter copper plated tungsten with a length/diameter ratio of approximately 300. The probe was attached to a specifically designed probe support for use in traversing the inducer flow passage (Fig. 10a).

42
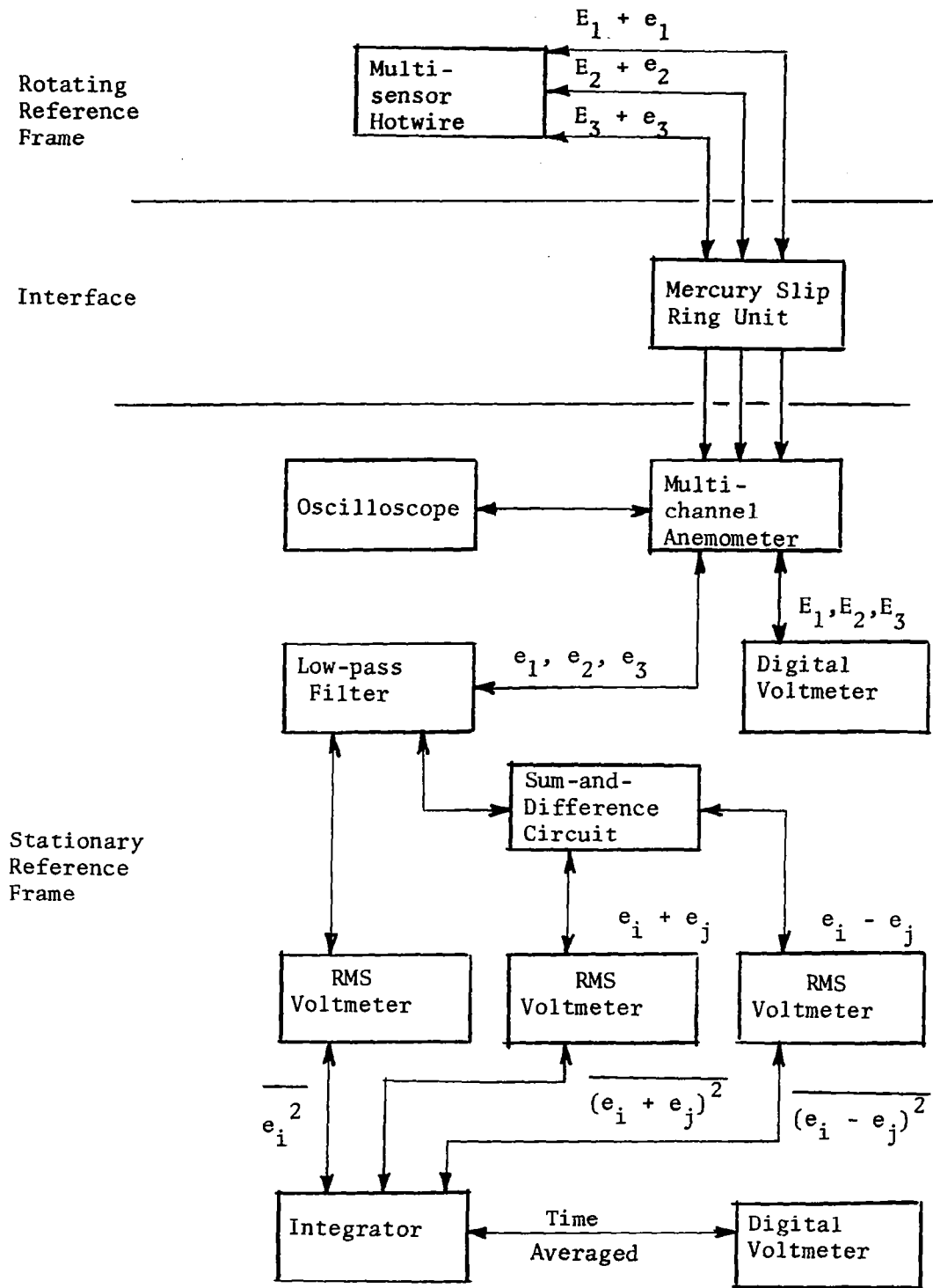


Figure 8.   Schematic Diagram of Rotating Hotwire Test Setup
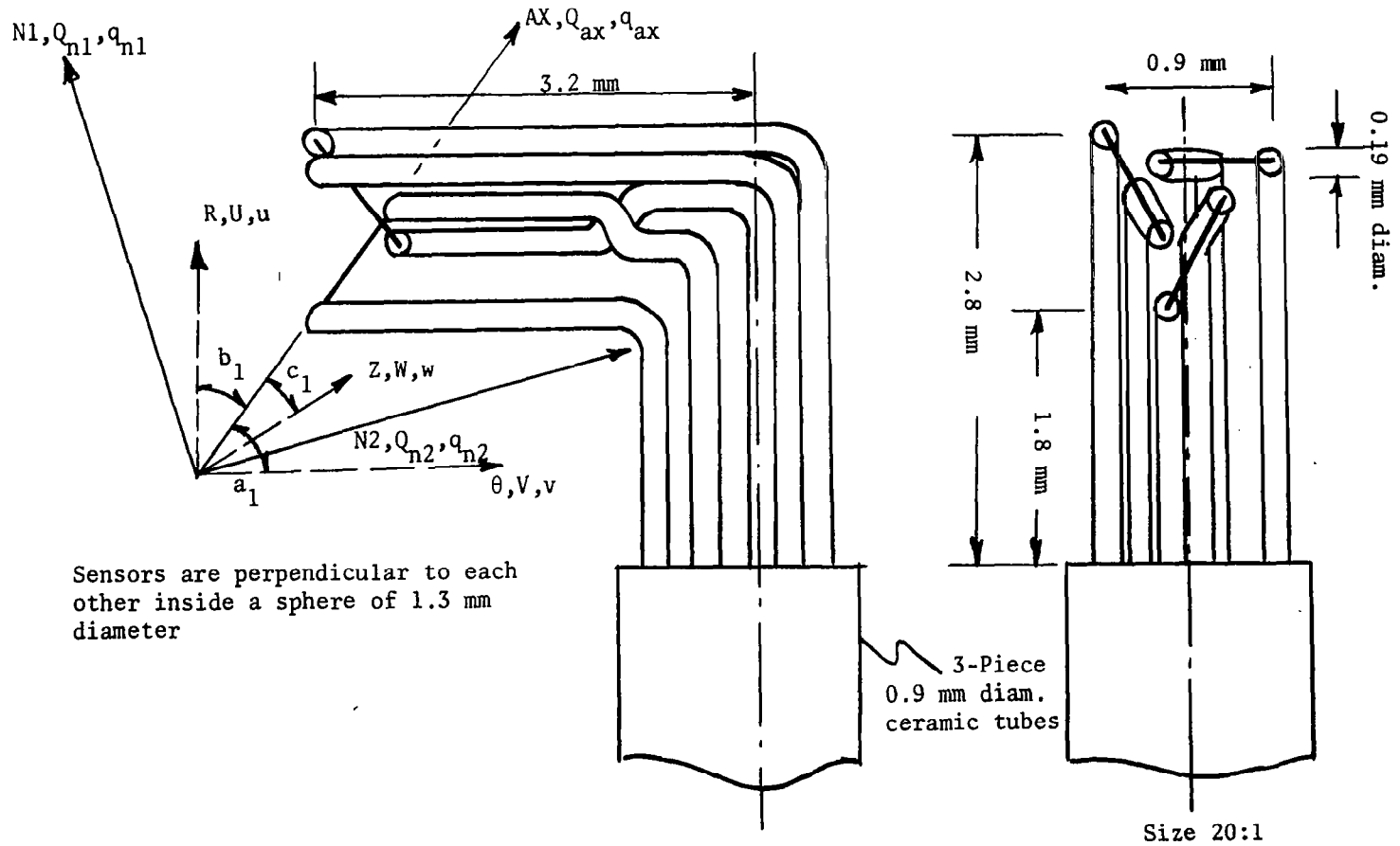
Figure 9. Sub-miniature Triaxial Hotwire Probe.
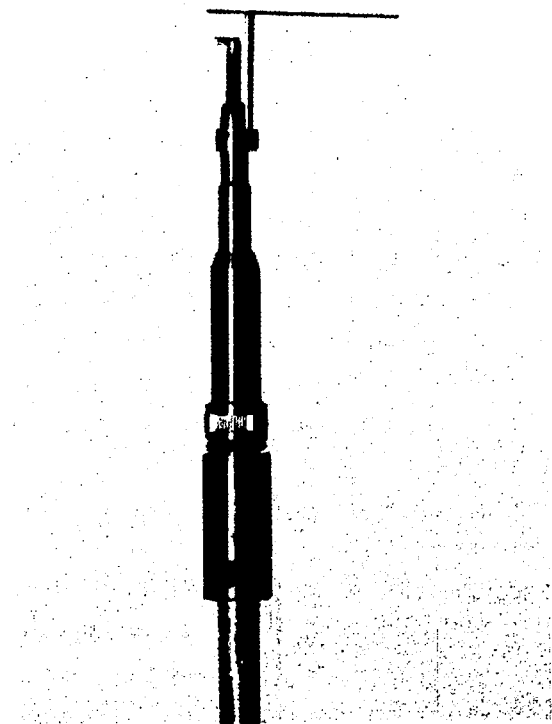
Figure 10a.  Triaxial Hotwire Probe
and Support

Figure 10b.  Triaxial Probe
Mounted in Inducer Hub

Three-Channel Constant Temperature Hotwire Anemometer.- Two dual-channel constant temperature hotwire anemometers were used to provide the three-channel capability necessary for these measurements. The original anemometer circuitry has been given in Ref. 20 and is not reproduced here.

Mercury Slip-Ring Unit.- A ten-channel mercury slip-ring unit was utilized in transmitting the hotwire signals from the rotating reference frame of the inducer to the stationary hotwire anemometers. The slip-ring unit exhibits the smallest and most stable resistance in the transfer of measuring signals from the rotating electrical elements to the stationary electrical conductors. Contact between the rotating wires and the stationary contact screws is made through a round contact disc to which the rotating wire is connected, rotating in mercury. Triple-distilled mercury was used to provide the greatest conductivity and the lowest noise level distortion possible.

Peripheral Equipment.- The A.C. voltage signals obtained from the hotwire anemometer were visualized on a four-channel storage oscilloscope. Instantaneous mean velocity D.C. voltage readings from the anemometers were displayed on a digital voltmeter.

The fluctuating voltage (A.C.) signals were processed through a 5.0 KHZ low-pass filter driven by a 15-volt regulated power supply, which was used to cut off the high frequency noise which may have entered the circuit.

Mean-square values of the A.C. voltages were obtained by passing the signals through a true RMS voltmeter and subsequently through a manually controlled signal integrator. The mean-squared voltage was displayed on a digital voltmeter.

A sum-and-difference circuit was utilized to obtain the sum and difference between the three hotwire signals needed for the turbulence intensity calculations.

A signal generator was used for sinewave generation to determine gains throughout the hotwire circuitry and the accuracy of the associated peripheral equipment.

Calibration Equipment.- A low-turbulence calibration tunnel was used for the hotwire calibration. The horizontal wind tunnel has a test cross-section of 1-1/2" x 1-1/2" and operates within the range of air velocities of 0 to 300 feet per second. The calibration velocities were measured with a nonshielded pitot tube and the micromanometer described previously.

Procedures and Techniques

Measurements were taken at two axial stations, corresponding to approximately 33% and 90% of the blade chord (Fig. 3). Various velocity measurements have previously been performed at these stations (Ref. 20) and thus a comparison of hotwire experimental results with these prior investigations are possible.

Six radial stations (corresponding to $r/r_t$ values of .973, .945, .890, .781, .671, .548) at station 1 and five radial stations ($r/r_t$ locations of .973, .945, .890, .781, .671) at station 2 were traversed at several tangential intervals within the blade passage in an attempt to get an accurate and detailed appraisal of the flow velocities,

turbulence intensities and stresses in these regions.  It was not
possible, however, to obtain measurements extremely close to the blade
surfaces due to the limitations caused by the blade curvature.

The three-sensor probe was attached to a ten-inch section of
aluminum tubing and fixed in a particular radial and tangential location
by a coupling mounted in the inducer hub (Fig. 10b).  The probe was
accurately aligned in the tangential direction with the aid of the guide
vane attached to the probe's adjustable protection pin.  Orientation of
the three individual hotwires was measured with respect to the (R, $\theta$, Z)
coordinate system (Fig. 9) by utilizing a linearly-calibrated scale eye-
piece in a 30-X microscope.  The direction cosines of this orientation
were then calculated, as were direction cosines of the two arbitrary
normals to each wire (Table 3).  These values were used in the governing
hotwire equations derived in the next chapter.

The experimental setup for the hotwire measurements is shown in
Fig. 11.  With the probe in position, the inducer was started and
rotated to 450 rpm.  The corresponding mean D.C. voltages of the three
hotwire channels $E_1$, $E_2$, $E_3$ were recorded, in addition to the statistical
properties of the fluctuating voltages

$$\overline{e_1^2}, \ \overline{e_2^2}, \ \overline{e_3^2}, \ \overline{(e_1 + e_2)^2}, \ \overline{(e_1 - e_2)^2},$$

$$\overline{(e_1 + e_3)^2}, \ \overline{(e_1 - e_3)^2}, \ \overline{(e_2 + e_3)^2} \text{ and } \overline{(e_2 - e_3)^2}.$$

The time-averaged voltages were obtained over an integration of 100
seconds.  The inducer was then stopped, the probe was moved to another
location, and the procedure repeated until the flow field was entirely

Table 3. Direction Cosines Used in Hotwire Analysis

| Angle Orientation (Fig. 9 and Eqns. 22-24) | | Hotwire 1 | | Hotwire 2 | | Hotwire 3 | |
|---|---|---|---|---|---|---|---|
| | | Angle (degrees) | Direction Cosine | Angle (degrees) | Direction Cosine | Angle (degrees) | Direction Cosine |
| AX-$\theta$ | $a_1$ | 117° 24.5' | -.46034 | 120° 59.2' | -.51486 | 130° 26.5' | -.64865 |
| AX-R | $b_1$ | 128° 53' | -.62773 | 49° 56.5' | .64357 | 94° 39' | -.08108 |
| AX-Z | $c_1$ | 51° 07' | .62773 | 55° 30.5' | .56634 | 139° 21.5' | -.75676 |
| N1-$\theta$ | $a_2$ | 90° | 0 | 90° | 0 | 90° | 0 |
| N1-R | $b_2$ | 45° | .70711 | 48° 39.1' | .66063 | 173° 53' | -.99431 |
| N1-Z | $c_2$ | 45° | .70711 | 138° 39.1' | -.75071 | 83° 53' | .10653 |
| N2-$\theta$ | $a_3$ | 152° 35.5' | -.88775 | 149° 00.8' | -.85728 | 139° 33.5' | -.76109 |
| N2-R | $b_3$ | 71° 00.2' | .32551 | 112° 44.5' | -.38651 | 86° 02.3' | .06910 |
| N2-Z | $c_3$ | 108° 59.8' | -.32551 | 109° 53.1' | -.34013 | 49° 50.5' | .64496 |

Figure 11.  Rotating Hotwire Test Setup

49

50

surveyed.  Station 1 and Station 2 were surveyed similarly, expect that no turbulence measurements were recorded at station 1.

The resultant voltage measurements from the three-channel rotating hotwire experiment were converted to mean velocities U, V, W and turbulence quantities $\overline{u^2}$, $\overline{v^2}$, $\overline{w^2}$, $\overline{uv}$, $\overline{uw}$, $\overline{vw}$ from the appropriate calibration curves and the applicable equations derived from the analysis of the next chapter.

The data reduction was accomplished in a computer program written to solve, for all flow stations considered, the resulting three simultaneous mean velocity equations and six simultaneous turbulence velocity equations.  The high speed digital computer at the Penn State Computation Center was used in this task.

# DERIVATION OF THE HOTWIRE EQUATIONS

The derivation of the equations for the three sensor-hotwire is a completely general method and is based on the hotwire configuration shown in Fig. 9.

## Direction Cosine Method for Nonorthogonal Probes

Consider one hotwire sensor with respect to the $(R, \theta, Z)$ coordinate system. Hotwire (1) has an orthogonal coordinate system $(AX, N1, N2)$ associated with its orientation. This $(AX, N1, N2)$ coordinate system can be transformed to the $(R, \theta, Z)$ coordinate system by:

$$(Q + q)_{ax} = a_1 (V + v) + b_1 (U + u) + c_1 (W + w) \qquad (22)$$

$$(Q + q)_{n1} = a_2 (V + v) + b_2 (U + u) + c_2 (W + w) \qquad (23)$$

$$(Q + q)_{n2} = a_3 (V + v) + b_3 (U + u) + c_3 (W + w) \qquad (24)$$

where $Q_{ax}$, $Q_{n1}$ and $Q_{n2}$ are the mean velocities associated with the $(AX, N1, N2)$ coordinate system and $U$, $V$ and $W$ are the transformed mean velocities in the $(R, \theta, Z)$ coordinate system. $q$, $u$, $v$, $w$ are the fluctuating components. The coefficients $a_1$, $b_1$, $c_1$, etc. are the applicable direction cosines between $(AX, N1, N2)$ and $(R, \theta, Z)$. The specific direction cosines for the triaxial hotwire probe used in the experimental studies of this thesis are given in Table 3.

The effective cooling velocity sensed by hotwire (1) is known (Ref. 22) to be:

$$(Q + q)_1 = [(Q + q)_{n1}^2 + (Q + q)_{n2}^2 + K_1^2 (Q + q)_{ax}]^{1/2} \qquad (25)$$

where $K_1$ is the associated correction factor for deviation from the cosine law.

Substituting equations 22-24 into equation 25 and expanding the resulting expression to reflect the instantaneous velocity components as the sum of the mean ($Q_1$, U, V, W) and fluctuating ($q_1$, u, v, w) velocity components, we get:

$$Q_1 + q_1 = [a_4(V^2 + v^2 + 2Vv) + b_4(U^2 + u^2 + 2Uu)$$

$$+ c_4(W^2 + w^2 + 2Ww) + d_4(UV + uv + Uv + Vu)$$

$$+ e_4(VW + vw + Vw + Wv)$$

$$+ f_4(UW + uw + Uw + Wu)]^{1/2} \qquad (26)$$

where the constant coefficients are defined as

$$a_4 = a_2^2 + a_3^2 + K_1^2 a_1^2$$

$$b_4 = b_2^2 + b_3^2 + K_1^2 b_1^2$$

$$c_4 = c_2^2 + c_3^2 + K_1^2 c_1^2$$

$$d_4 = 2 (a_2 b_2 + a_3 b_3 + K_1^2 a_1 b_1)$$

$$e_4 = 2 (a_2 c_2 + a_3 c_3 + K_1^2 a_1 c_1)$$

$$f_4 = 2 (b_2 c_2 + b_3 c_3 + K_1^2 b_1 c_1)$$

The right side of equation 26 can be linearized by

$$(1 + \Delta)^{1/2} = 1 + \Delta/2 - \Delta^2/8 + \ldots \tag{27}$$

where $\Delta$ is considered small. Thus, equation 26 can be approximated to the following expression:

$$Q_1 + q_1 = a_5 (V + v) + a_6 (U + u) + a_7 (W + w)$$

$$+ a_8 (\frac{U^2}{V} + \frac{u^2}{V}) + a_9 (\frac{W^2}{V} + \frac{w^2}{V}) + a_{10} (\frac{UW}{V} + \frac{uw}{V})$$

$$+ a_{11} \frac{Uu}{V} + a_{12} \frac{Ww}{V} + a_{13} (\frac{Uw}{V} + \frac{Wu}{V}) + 0(\varepsilon) \tag{28}$$

where the constant coefficients are defined by

$$a_5 = \sqrt{a_4}$$

$$a_6 = d_4/2 \sqrt{a_4}$$

$$a_7 = e_4/2 \sqrt{a_4}$$

$$a_8 = \sqrt{a_4} \; [\frac{b_4}{2a_4} - \frac{1}{8} (\frac{d_4}{a_4})^2]$$

$$a_9 = \sqrt{a_4} \; [\frac{c_4}{2a_4} - \frac{1}{8} (\frac{e_4}{a_4})^2]$$

$$a_{10} = \sqrt{a_4} \; [\frac{f_4}{2a_4} - \frac{1}{4} (\frac{d_4}{a_4}) (\frac{e_4}{a_4})]$$

54

$$a_{11} = \sqrt{a_4} \ \ [\frac{b_4}{a_4} - \frac{1}{4} (\frac{d_4}{a_4})^2]$$

$$a_{12} = \sqrt{a_4} \ \ [\frac{c_4}{a_4} - \frac{1}{4} (\frac{e_4}{a_4})^2]$$

$$a_{13} = a_{10}$$

Taking the time-average of equation 28, we get:

$$Q_1 = a_5 V + a_6 U + a_7 W + a_8 (\frac{U^2}{V} + \frac{\overline{u^2}}{V})$$

$$+ a_9 (\frac{W^2}{V} + \frac{\overline{w^2}}{V}) + a_{10} (\frac{UW}{V} + \frac{\overline{uw}}{V}) \tag{29}$$

If we consider the fluctuating quantities $\overline{u^2}$, $\overline{w^2}$ and $\overline{uw}$ to be small, then the equation for the mean velocity sensed by the hotwire can be approximated by:

$$Q_1 = a_5 V + a_6 U + a_7 W + a_8 \frac{U^2}{V} + a_9 \frac{W^2}{V} + a_{10} \frac{UW}{V} \tag{30}$$

The difference between equations 28 and 29 is the fluctuating velocity sensed by the hotwire:

$$q_1 = a_5 v + a_6 u + a_7 w + a_8 (\frac{u^2}{V} - \frac{\overline{u^2}}{V})$$

$$+ a_9 (\frac{w^2}{V} - \frac{\overline{w^2}}{V}) + a_{10} (\frac{uw}{V} - \frac{\overline{uw}}{V}) + a_{11} \frac{Uu}{V}$$

$$+ a_{12} \frac{Ww}{V} + a_{13} (\frac{Uw}{V} + \frac{Wu}{V}) \tag{31}$$

Expressions similar to equations 30 and 31 for $Q_2$, $Q_3$, $q_2$ and $q_3$ corresponding to the mean and fluctuating velocities sensed by hotwires (2) and (3) can be derived.

## Relating Voltages and Velocities

Application of King's Law (Ref. 6) for hotwire (1) relates instantaneous velocity (= $Q_1 + q_1$) and instantaneous voltage (= $E_1 + e_1$) by the expression

$$(E_1 + e_1)^2 = E_o^2 + B_1 \sqrt{Q_1 + q_1} \tag{32}$$

where $B_1$ is the slope of the hotwire calibration curve, $E_o$ is the hot-wire voltage at zero velocity, $E_1$ is the mean voltage and $e_1$ is the fluctuating component.

Expanding and linearizing equation 32 for small $q_1/Q_1$, we get

$$E_1^2 + 2E_1 e_1 + e_1^2 = E_o^2 + B_1\sqrt{Q_1} \left(1 + \frac{1}{2} q_1/Q_1 - \ldots\right) \tag{33}$$

The time-average of equation 33 relates the mean velocities and voltages. Neglecting $\overline{e_1^2}$, we find

$$E_1^2 = E_o^2 + B_1 \sqrt{Q_1} \tag{34}$$

Subtracting equation 34 from equation 33 and neglecting $e_1^2$, then

$$2E_1 e_1 = \frac{B_1 q_1}{2 \sqrt{Q_1}} \tag{35}$$

or

$$q_1 = \left(\frac{4 \, E_1 \sqrt{Q_1}}{B_1}\right) e_1 \tag{36}$$

Similar expressions can be derived for hotwires (2) and (3). Rewriting equation 36 as $q_1 = L_1 e_1$, the time-averaged fluctuating quantities can be found to be

$$
\left\{
\begin{array}{l}
\overline{q_1^2} = L_1^2 \, \overline{e_1^2} \\[2ex]
\overline{q_2^2} = L_2^2 \, \overline{e_2^2} \\[2ex]
\overline{q_3^2} = L_3^2 \, \overline{e_3^2}
\end{array}
\right\}
\quad \text{and} \quad
\left\{
\begin{array}{l}
\overline{q_1 q_2} = L_1 L_2 \, \overline{e_1 e_2} \\[2ex]
\overline{q_1 q_3} = L_1 L_3 \, \overline{e_1 e_3} \\[2ex]
\overline{q_2 q_3} = L_2 L_3 \, \overline{e_2 e_3}
\end{array}
\right\} \tag{37}
$$

The values of $\overline{e_1^2}$, $\overline{e_2^2}$ and $\overline{e_3^2}$ are obtained directly from the experimental hotwire measurements. The values of $\overline{e_1 e_2}$, $\overline{e_1 e_3}$ and $\overline{e_2 e_3}$ are derived as follows:

$$\overline{e_1 e_2} = \frac{1}{4} \, [\overline{(e_1 + e_2)^2} - \overline{(e_1 - e_2)^2}]$$

$$\overline{e_1 e_3} = \frac{1}{4} \, [\overline{(e_1 + e_3)^2} - \overline{(e_1 - e_3)^2}] \tag{38}$$

$$\overline{e_2 e_3} = \frac{1}{4} \, [\overline{(e_2 + e_3)^2} - \overline{(e_2 - e_3)^2}]$$

The mean-squared voltages within the brackets are obtained by utilizing the sum-and-difference circuit in the experimental hotwire measurement (Fig. 8).

## Mean Velocity Calculation

Equation 30 for hotwire sensor (1) and similar equations derived for sensors (2) and (3) form a set of three nonlinear simultaneous equations in three unknowns:

$$Q_1 = a_5 V + a_6 U + a_7 W + a_8 \frac{U^2}{V} + a_9 \frac{W^2}{V} + a_{10} \frac{UW}{V} \qquad (39)$$

$$Q_2 = b_5 V + b_6 U + b_7 W + b_8 \frac{U^2}{V} + b_9 \frac{W^2}{V} + b_{10} \frac{UW}{V} \qquad (40)$$

$$Q_3 = c_5 V + c_6 U + c_7 W + c_8 \frac{U^2}{V} + c_9 \frac{W^2}{V} + c_{10} \frac{UW}{V} \qquad (41)$$

where the coefficients $a_5$, $b_5$, etc. reflect the appropriate combination of direction cosines, K factor, etc.

Values of $Q_1$, $Q_2$ and $Q_3$ are known from application of equation 34 to the D.C. hotwire voltages obtained from the experimental hotwire measurements. Solution of equations 39-41 thus give U, V and W for each measurement location considered.

The Newton-Raphson method provides an iterative procedure for solving a nonlinear system of equations involving n real functions and n real variables. Details of the method are given in Ref. 3. Applying this method to the three simultaneous nonlinear equations 39-41, we can define the expression

$$f_1(U, V, W) = a_5 V + a_6 U + a_7 W + a_8 \frac{U^2}{V} + a_9 \frac{W^2}{V} + a_{10} \frac{UW}{V} - Q_1 \qquad (42)$$

$$f_2(U, V, W) = b_5 V + b_6 U + b_7 W + b_8 \frac{U^2}{V} + b_9 \frac{W^2}{V} + b_{10} \frac{UW}{V} - Q_2 \qquad (43)$$

58

$$f_3(U, V, W) = c_5 V + c_6 U + c_7 W + c_8 \frac{U^2}{V} + c_9 \frac{W^2}{V} + c_{10} \frac{UW}{V} - Q_3 \qquad (44)$$

After determining the partial derivative expressions

$$\left[ \frac{\partial f_i}{\partial U} , \frac{\partial f_i}{\partial V} , \frac{\partial f_i}{\partial W} \right]_{i = 1,3} \qquad (45)$$

the Newton-Raphson iteration equation can be written:

$$\frac{\partial f_1}{\partial U} \cdot \Delta U + \frac{\partial f_1}{\partial V} \cdot \Delta V + \frac{\partial f_1}{\partial W} \cdot \Delta W = - f_1 \qquad (46)$$

$$\frac{\partial f_2}{\partial U} \cdot \Delta U + \frac{\partial f_2}{\partial V} \cdot \Delta V + \frac{\partial f_2}{\partial W} \cdot \Delta W = - f_2 \qquad (47)$$

$$\frac{\partial f_3}{\partial U} \cdot \Delta U + \frac{\partial f_3}{\partial V} \cdot \Delta V + \frac{\partial f_3}{\partial W} \cdot \Delta W = - f_3 \qquad (48)$$

where, for the $i^{th}$ iteration,

$$U_i = U_{i-1} + \Delta U \qquad (49)$$

$$V_i = V_{i-1} + \Delta V \qquad (50)$$

$$W_i = W_{i-1} + \Delta W \qquad (51)$$

For an initial approximation $U_o$, $V_o$ and $W_o$, the initial values of $f_1$, $f_2$ and $f_3$ from equations 42-44 and their associated partial derivatives (equation 45) can be calculated. From a matrix analysis of equations 46-48, the values of $\Delta U$, $\Delta V$ and $\Delta W$ can be determined and the values of $U_i$, $V_i$ and $W_i$ adjusted according to equations 49-51. The above procedure

is repeated until a suitable convergence criteria is satisfied (i.e., until $\Delta U$, $\Delta V$ and $\Delta W$ are less than some small number $\varepsilon$).

### Fluctuating Velocities, Turbulence Intensities and Stresses

Equation 31 for hotwire sensor (1) is squared and time-averaged to give the following expression (neglecting small order terms such as $\overline{u^4}$, $\overline{u^2 v^2}$, etc.):

$$
\begin{aligned}
\overline{q_1^2} = a_5^2 \, \overline{v^2} &+ [a_6^2 + a_{11}^2 \, (\tfrac{U}{V})^2 + a_{13}^2 \, (\tfrac{W}{V})^2 + 2a_6 a_{11} \, (\tfrac{U}{V}) \\[4pt]
&+ 2a_6 a_{13} \, (\tfrac{W}{V}) + 2a_{11}a_{13} \, (\tfrac{UW}{V^2})] \, \overline{u^2} + [a_7^2 + a_{12}^2 \, (\tfrac{W}{V})^2 \\[4pt]
&+ a_{13}^2 \, (\tfrac{U}{V})^2 + 2a_7 a_{12} \, (\tfrac{W}{V}) + 2a_7 a_{13} \, (\tfrac{U}{V}) + 2a_{12}a_{13} \, (\tfrac{UW}{V^2})] \, \overline{w^2} \\[4pt]
&+ [2a_5 a_6 + 2a_5 a_{11} \, (\tfrac{U}{V}) + 2a_5 a_{13} \, (\tfrac{W}{V})] \, \overline{uv} \\[4pt]
&+ [2a_5 a_7 + 2a_5 a_{12} \, (\tfrac{W}{V}) + 2a_5 a_{13} \, (\tfrac{U}{V})] \, \overline{vw} \\[4pt]
&+ [2a_6 a_7 + (2a_6 a_{12} + 2a_7 a_{13}) \, \tfrac{W}{V} + (2a_6 a_{13} + 2a_7 a_{11}) \, \tfrac{U}{V} \\[4pt]
&+ (2a_{11}a_{12} + 2a_{13}^2) \, (\tfrac{UW}{V^2}) + 2a_{11}a_{13} \, (\tfrac{U}{V})^2 + 2a_{12}a_{13} \, (\tfrac{W}{V})^2] \, \overline{uw} + 0(\varepsilon)
\end{aligned}
$$

$$(52)$$

Similar equations for $\overline{q_2^2}$ and $\overline{q_3^2}$ can be derived for hotwire sensors (2) and (3).

60

Likewise, equation 31 can be multiplied by the corresponding expression for $q_2$ and time-averaged to obtain:

$$\overline{q_1 q_2} = a_5 b_5 \overline{v^2} + [a_6 b_6 + a_{11} b_{11} (\tfrac{U}{V})^2 + a_{13} b_{13} (\tfrac{W}{V})^2$$

$$+ (a_6 b_{11} + a_{11} b_6) \tfrac{U}{V} + (a_6 b_{13} + a_{13} b_6) \tfrac{W}{V} + (a_{11} b_{13} + a_{13} b_{11}) \tfrac{UW}{V^2}] \overline{u^2}$$

$$+ [a_7 b_7 + a_{12} b_{12} (\tfrac{W}{V})^2 + a_{13} b_{13} (\tfrac{U}{V})^2 + (a_7 b_{12} + a_{12} b_7) \tfrac{W}{V}$$

$$+ (a_7 b_{13} + a_{13} b_7) \tfrac{U}{V} + (a_{12} b_{13} + a_{13} b_{12}) \tfrac{UW}{V^2}] \overline{w^2} + [a_5 b_6 + a_6 b_5$$

$$+ (a_5 b_{11} + a_{11} b_5) \tfrac{U}{V} + (a_6 b_{12} + a_{12} b_5) \tfrac{W}{V}] \overline{uv} + [a_5 b_7 + a_7 b_5$$

$$+ (a_5 b_{12} + a_{12} b_5) \tfrac{W}{V} + (a_5 b_{13} + a_{13} b_5) \tfrac{U}{V}] \overline{vw} + [a_6 b_7 + a_7 b_6$$

$$+ (a_6 b_{12} + a_{12} b_6 + a_7 b_{13} + a_{13} b_7) \tfrac{W}{V} + (a_6 b_{13} + a_{13} b_6 + a_7 b_{11} + a_{11} b_7) \tfrac{U}{V}$$

$$+ (a_{11} b_{12} + a_{12} b_{11} + 2a_{13} b_{13}) \tfrac{UW}{V^2} + (a_{11} b_{13} + a_{13} b_{11}) \tfrac{U^2}{V^2}$$

$$+ (a_{12} b_{13} + a_{13} b_{12}) \tfrac{W^2}{V^2}] \overline{uw} + 0(\varepsilon) \tag{53}$$

where the constants $b_n$, n = 5 to 13 refer to the coefficients in the expression for $q_2$ and are similar to the values of $a_n$ in equation 28.

Expressions similar to equation 53 can be derived for $\overline{q_1 q_3}$ and $\overline{q_2 q_3}$. Thus, the set of equations 52 and 53 form a set of six non-linear equations in nine unknowns. As an approximate method of solution, the mean velocities U, V and W are first calculated from equations 39-41

using the iteration method described in the previous section. These

velocities are then used to calculate the coefficients of equations 52

and 53. As a result, these equations are reduced to six linear equations

in six unknowns which can then be solved simultaneously to give the

quantities $\overline{u^2}$, $\overline{v^2}$, $\overline{w^2}$, $\overline{uv}$, $\overline{uw}$ and $\overline{vw}$. A computer program, coded in

Fortran IV and given in Appendix C, has been written to use the hotwire

data obtained from the experimental portion of this thesis to solve

equations 39-41, 52 and 53 for the mean velocities, turbulence intensities

and stresses respectively. The results are presented in the next

chapter.

## EXPERIMENTAL RESULTS AND COMPARISON WITH THEORY

Results of the experimental investigations are given in this chapter. In addition, comparison of these results with the theoretical results of the inviscid and viscid exact analysis programs are presented.

### Blade Static Pressure

Experimental results are plotted in Figs. 12-16 for the five radial passage stations defined previously. It should be reiterated that the measurement stations do not correspond to constant radii, since the annulus passage is continuously varying. The measurement stations are illustrated in Fig. 3 and the pressure tap locations are specified in Tables 1 and 2.

The inducer design characteristic of trailing edge loaded blades is apparent from the measured $\psi_s$ distributions. $\psi_s$ measurements on the blade pressure surface remain positive across the entire chord length, with the gradient increasing continuously from hub to tip. The pressure surface $\psi_s$ distribution decreases near the trailing edge, varying in the location at which the downswing begins from approximately 80% chord near the tip to greater than 90% chord near the hub. The blade suction surface $\psi_s$ measurements near the hub leading edge begin negative and become positive beyond 35% chord. At radial stations 3 thru 5, corresponding to mid-passage thru tip, the suction surface $\psi_s$ distribution appears to begin with positive values, cross to negative values at approximately 20-30% chord and then return to positive values at 40-55% chord. The cross-over points increase in distance from the leading edge
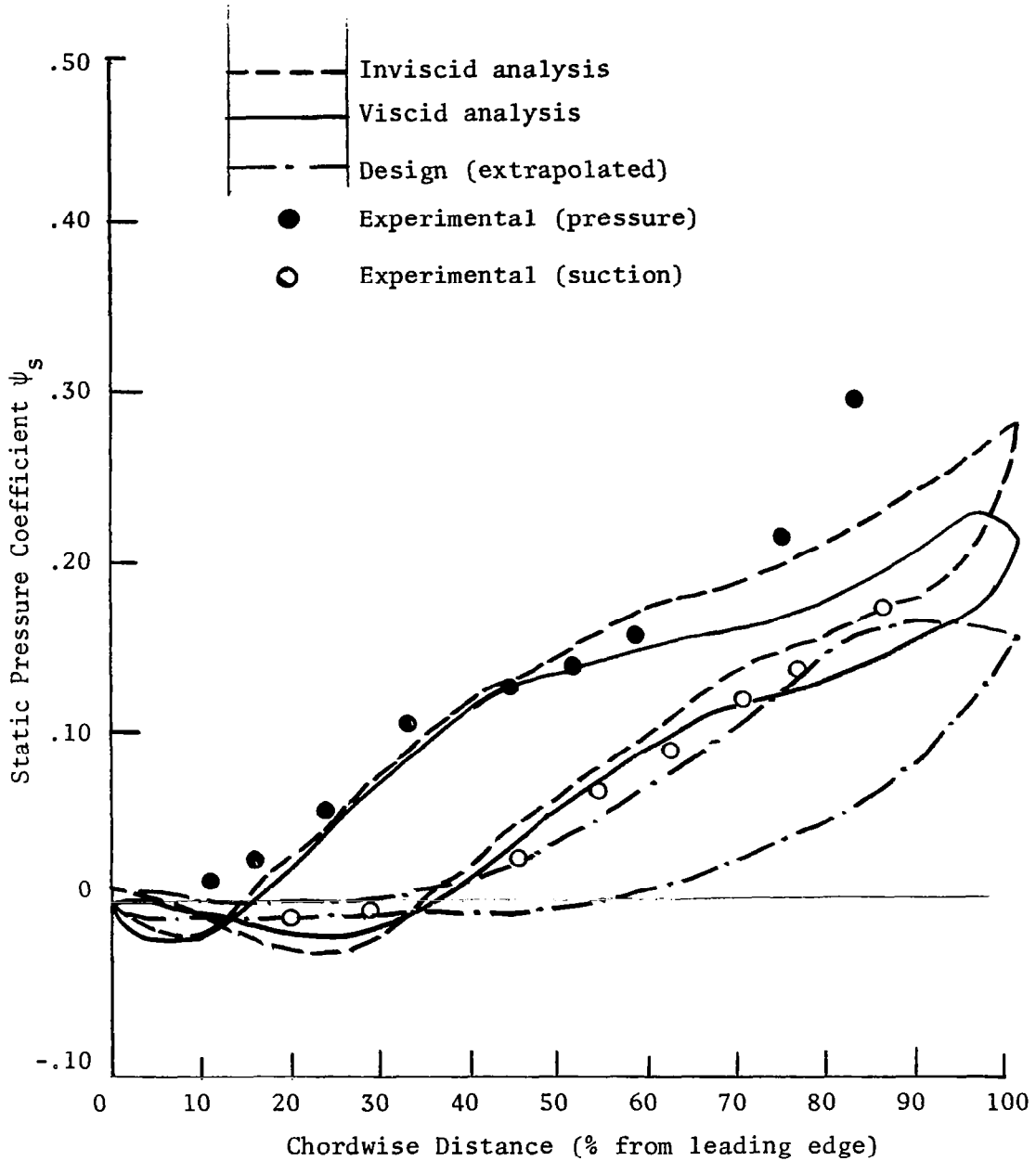
Figure 12. Blade Static Pressure Distribution - Radial Station 1

64
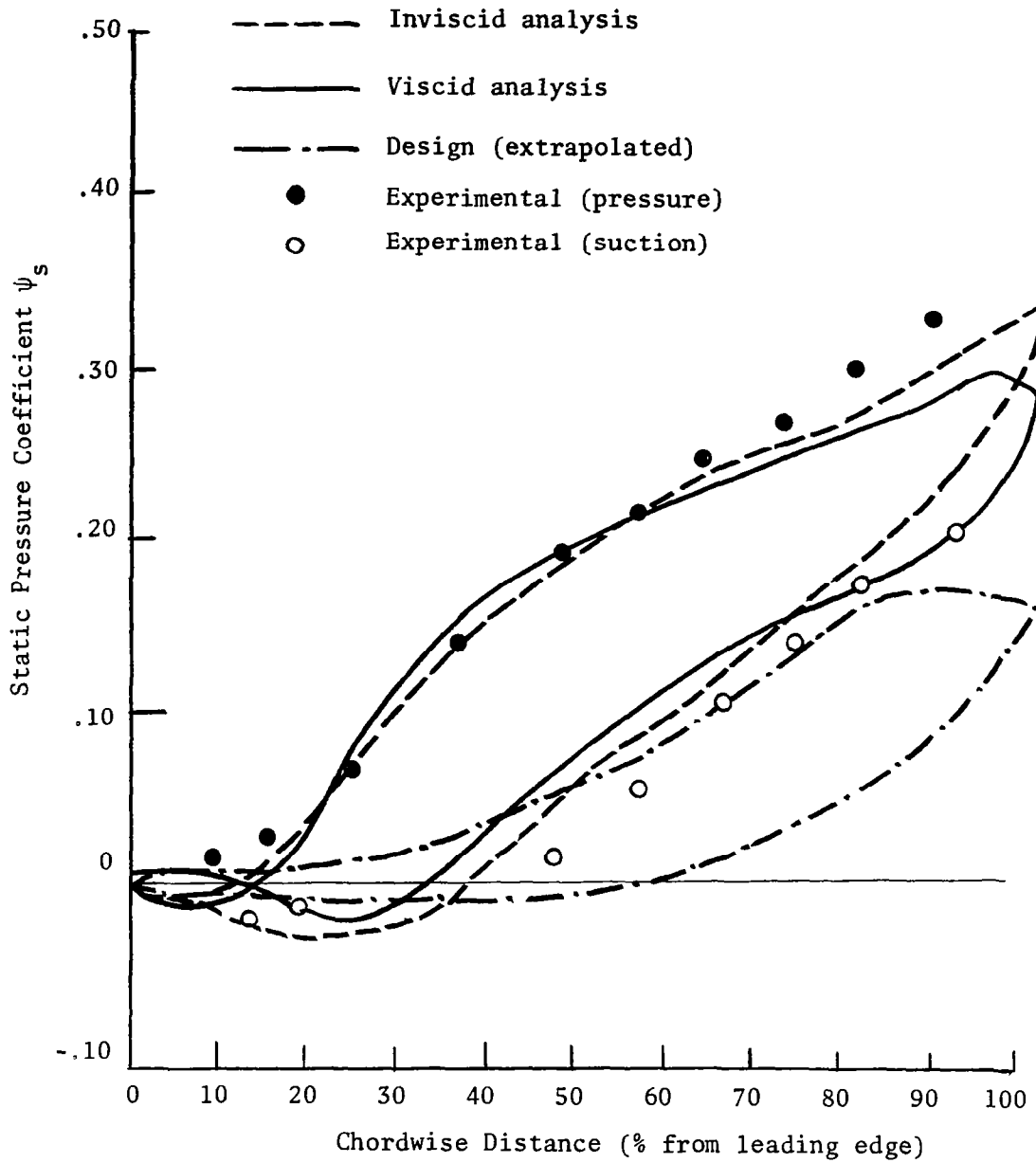


Figure 13. Blade Static Pressure Distribution - Radial Station 2
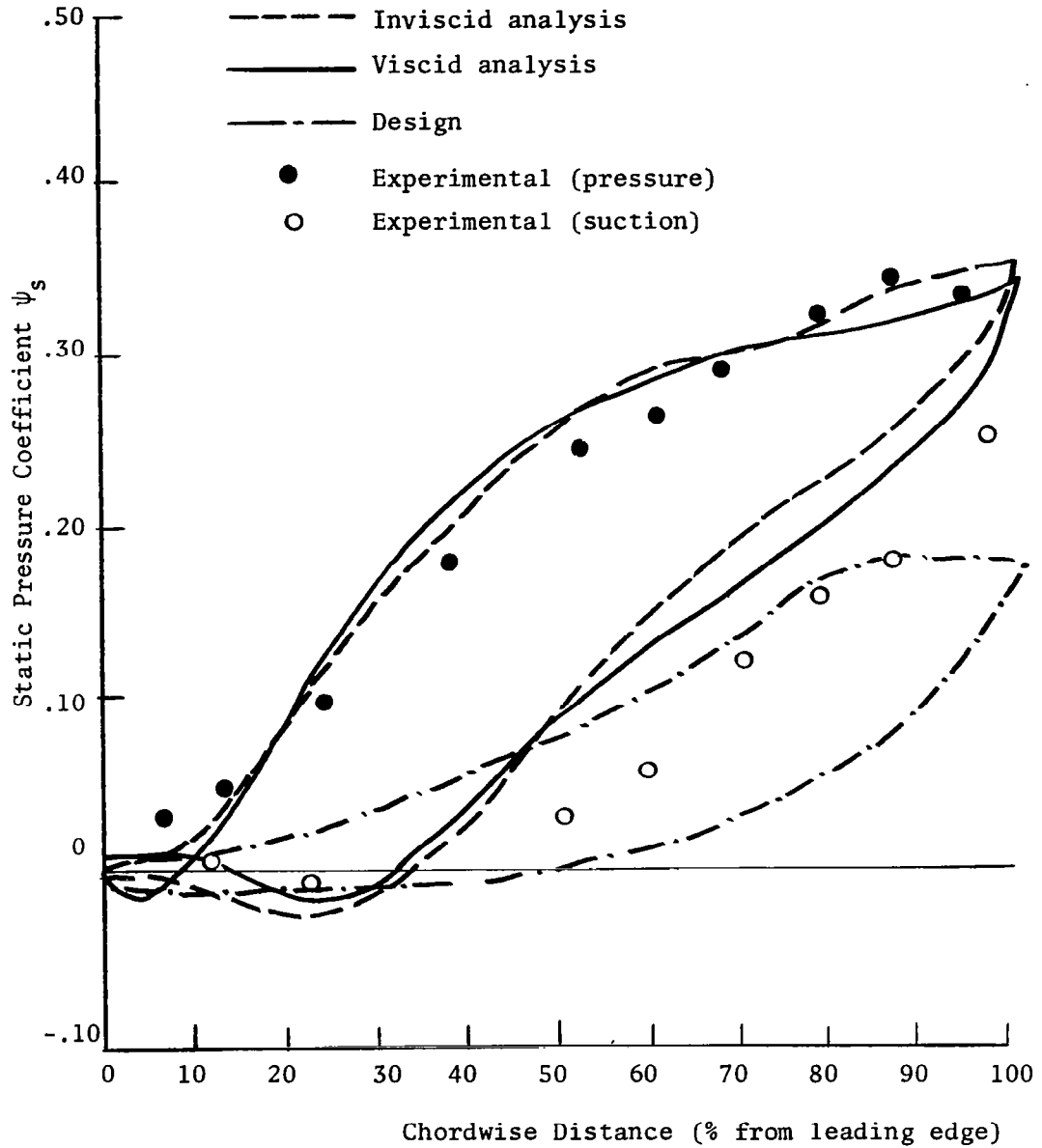
Figure 14.   Blade Static Pressure Distribution - Radial Station 3
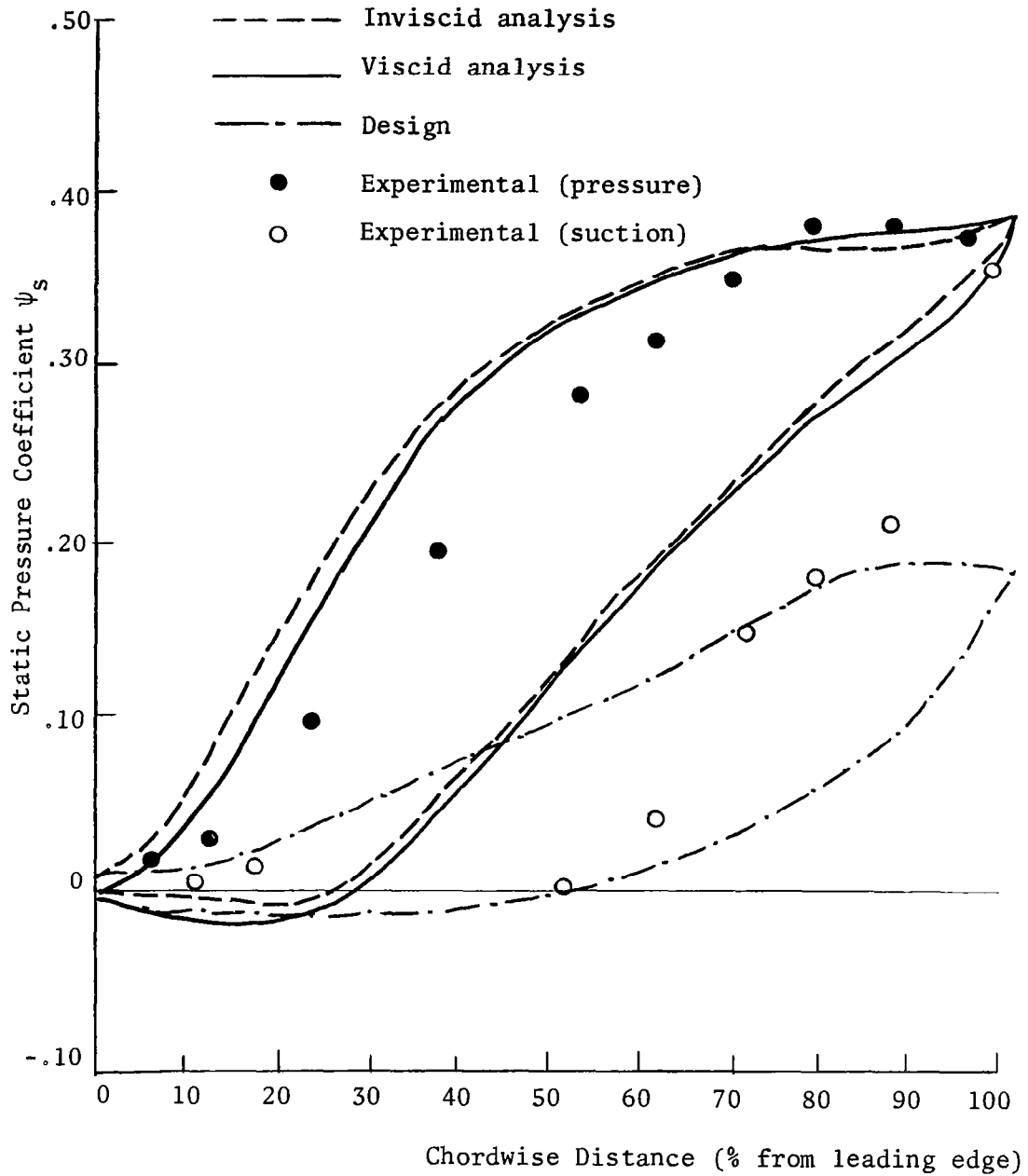
Figure 15.  Blade Static Pressure Distribution - Radial Station 4
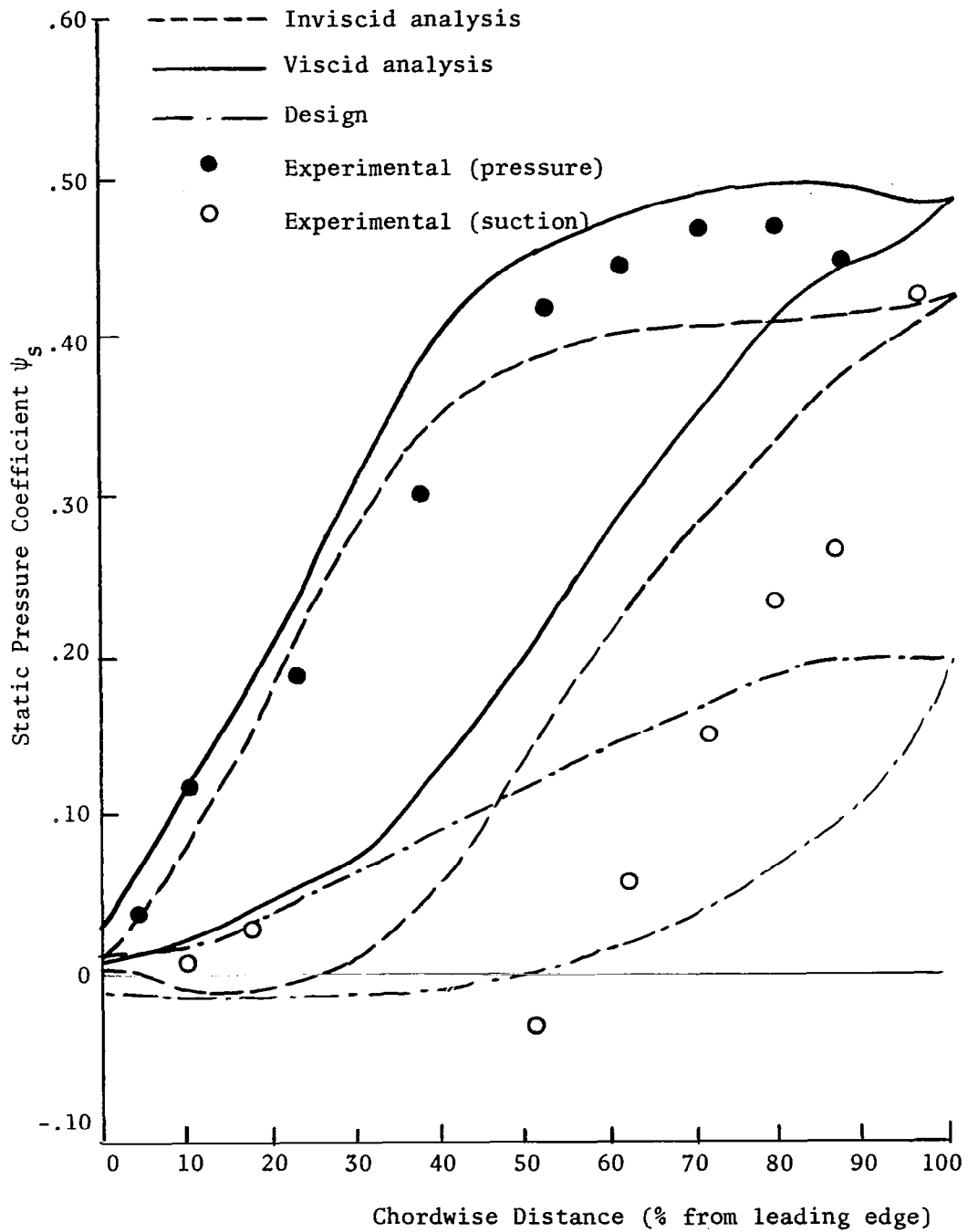
Figure 16. Blade Static Pressure Distribution - Radial Station 5

at the radial stations nearer the tip. It is also noted that the difference between the pressure surface $\psi_s$ and suction surface $\psi_s$ at most chordwise locations increases continuously from hub to tip.

It is apparent from Figs. 12-16 that there is a large discrepancy between the experimental and design curves. The design curves are based on two-dimensional theory and are derived from the mean streamline method of Wislicenus (Ref. 25). The experimental results indicate that the three-dimensional inviscid effects are appreciable.

The radial variation of the passage-averaged blade static pressure coefficients are compared in Figs. 17a-b for axial flow survey stations 1 and 2 (shown in Fig. 3). It can be seen that, for both locations, the discrepancy between design and experiment is greater near the tip, indicating the presence of velocity deficiencies resulting from increased flow losses in this region. At station 1, the difference between the design and experimental curves does not appear to increase until approximately $R = .8$, whereas at station 2, the difference begins increasing at a radius much closer to the hub. This tends to indicate an increase in the extent of the loss region as the flow moves downstream through the inducer passage.

Blade Limiting Streamline Angles

The blade limiting streamline angle $\alpha$ is the limiting position (in degrees) of the flow streamline as the blade surface is approached (Fig. 2). The angle is measured from the two-dimensional or design flow direction and hence represents the extent of three-dimensionality in the flow. A similar parameter $\varepsilon_w = \tan \alpha$ can also be defined which, in the peculiar geometry of the inducer, can approximate the ratio U/V
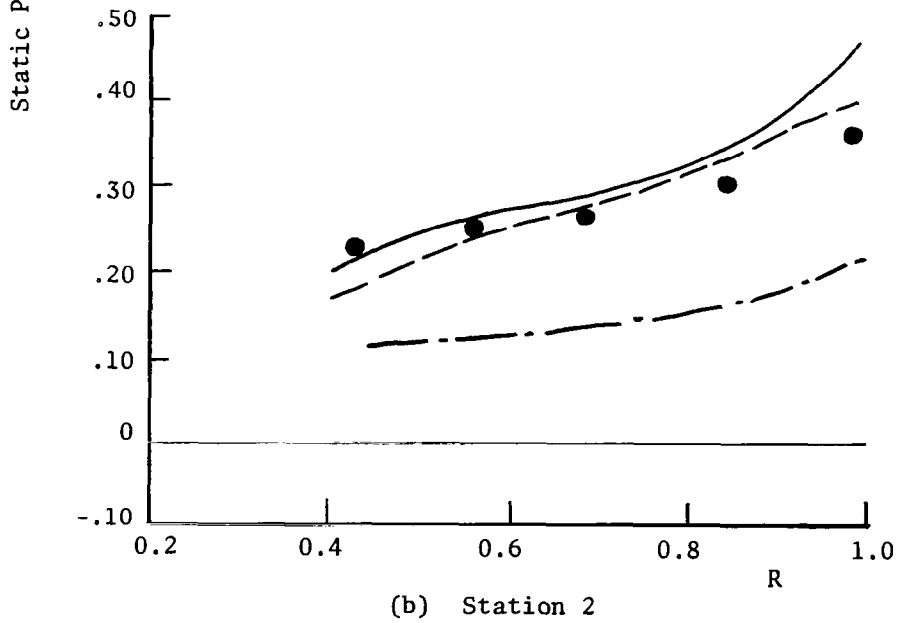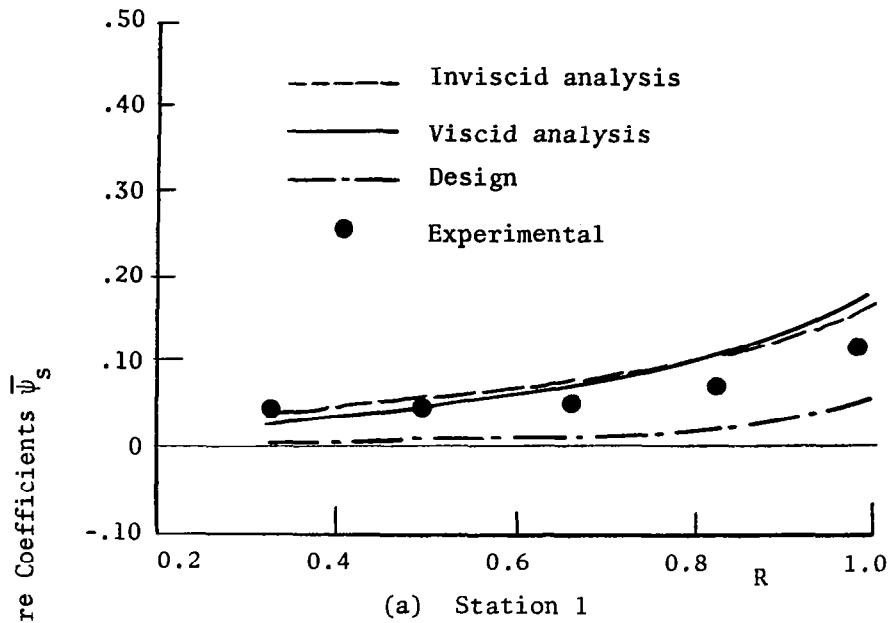
Figure 17. Radial Variation of Passage-Averaged Static
Pressure Coefficient at Stations 1 and 2

at the blade surface. The tangential variation of $\alpha$ with blade chord for each of the five radial measurement stations is shown for the pressure surface in Fig. 18 and for the suction surface in Fig. 19.

The pressure surface distribution of $\alpha$ at the tip (radial station 5) indicates negative values of $\alpha$ (and, thus, radially inward flow) from leading edge to mid-chord position. This tends to indicate the presence of the annulus wall boundary layer scraping effect which induces flow away from the tip. At all other radial stations, $\alpha$ increases continuously from leading edge to trailing edge. Near the hub trailing edge, $\alpha$ increases quite rapidly. The blade limiting streamline angles at both radial stations 1 and 2 appear to extrapolate beyond $90^{o}$, which is an indication of the existence of backflow in this region. This is presumably brought about by large radially outward flow that exists in the wake immediately downstream of the trailing edge. This has a tendency to decrease axial velocity near the hub and thus induce back-flows. At most axial locations, $\alpha$ decreases continuously from hub to tip. In several instances, this decrease appears linear.

The suction surface $\alpha$ distribution remains relatively constant at all radial stations up to approximately 60% chord from the leading edge, when a more pronounced increase is noticed. At all stations except the tip, this increase extends to approximately 85% chord and then $\alpha$ decreases toward the trailing edge. This is possibly due to the blade blockage effect in this region. At the tip, $\alpha$ increases continuously and no decrease is noted. Again, as in the pressure surface distribution, $\alpha$ decreases continuously from hub to tip at practically all axial locations, and at some locations the variation appears linear.
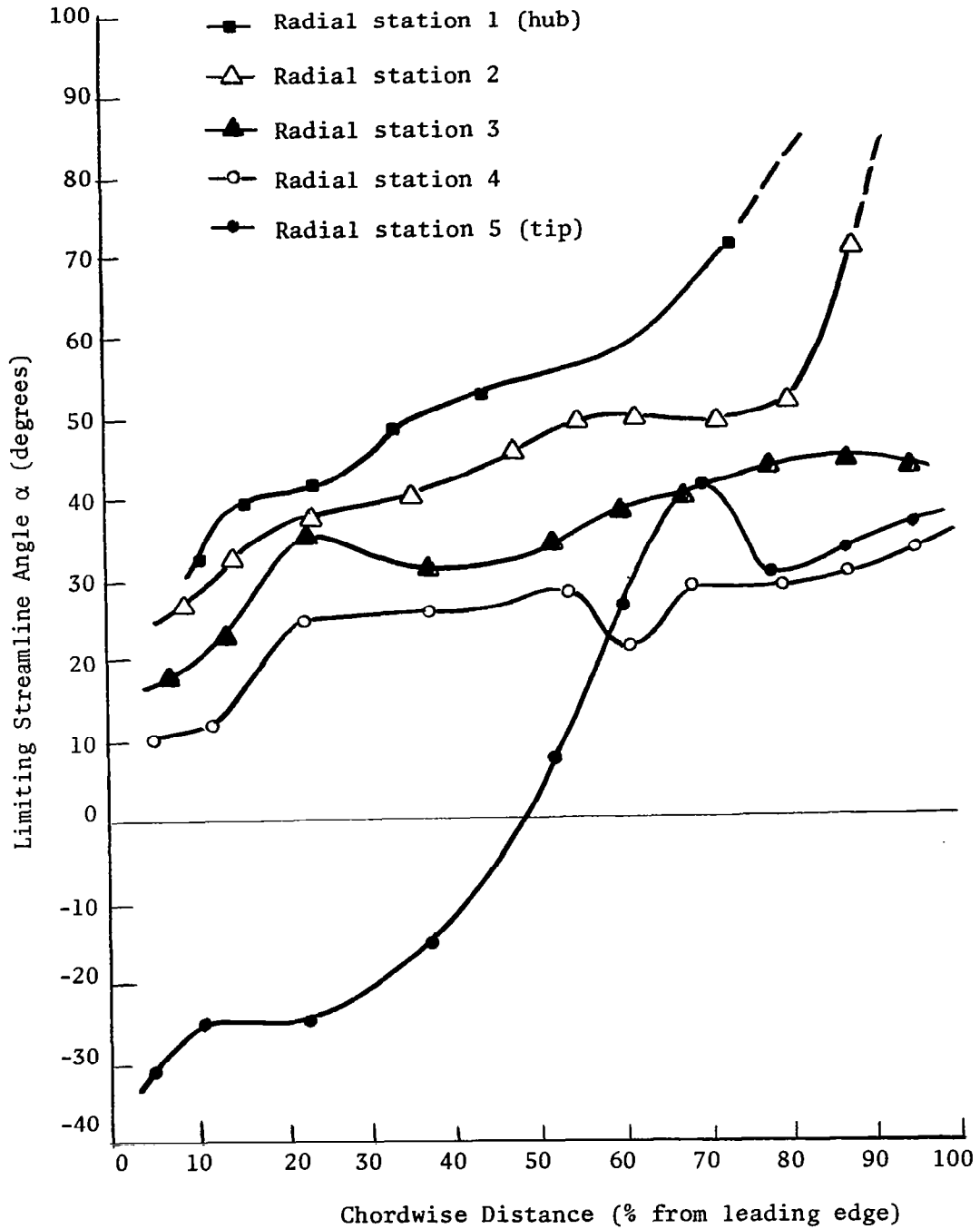
Figure 18.  Chordwise Variation of Limiting Streamline
Angle on Blade Pressure Surface
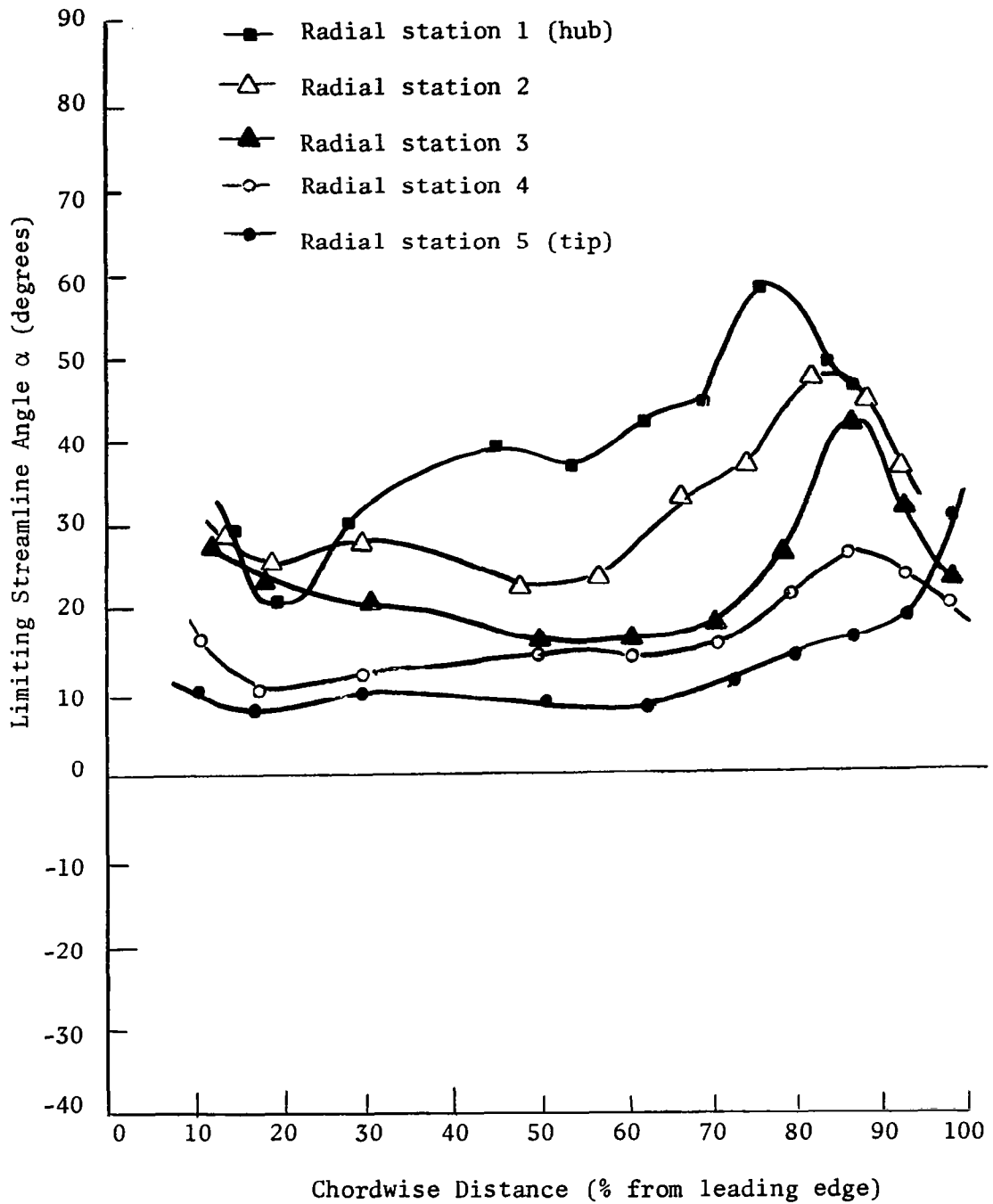
Figure 19. Chordwise Variation of Limiting Streamline Angle
on Blade Suction Surface

In most instances, the magnitudes of $\alpha$ on the suction surface are lower than at the corresponding position on the pressure surface. Fig. 20 shows the radial variation of $\alpha$ at the trailing edge. The deviation between pressure and suction surface measurements decrease continuously with increasing radius from hub to tip. The magnitude of $\alpha$, which is an indication of the extent of radial flows, is much higher than the values of a single blade reported in Ref. 14. This indicates that the radial velocity in the inducers are quite appreciable, especially near the blade surfaces.

## Mean Velocity Profiles

The triaxial hotwire probe was used to measure the relative velocity profiles inside the inducer passage. As an indication of the effectiveness of this method in obtaining the relative velocity measurements, Fig. 21 compares the total relative velocity profile at station 1 derived from the hotwire measurements with the results of Ref. 7 obtained from rotating pressure probe measurements. Good agreement is indicated at the two radii shown.

The axial, radial and relative tangential velocity components described in this section are derived from the hotwire measurements and analysis described in the previous chapter.

Measurements at Station 1

<u>Total Relative Velocity</u>.- Fig. 22 shows the tangential variation of total relative velocity $Q_R$ across the inducer passage at several
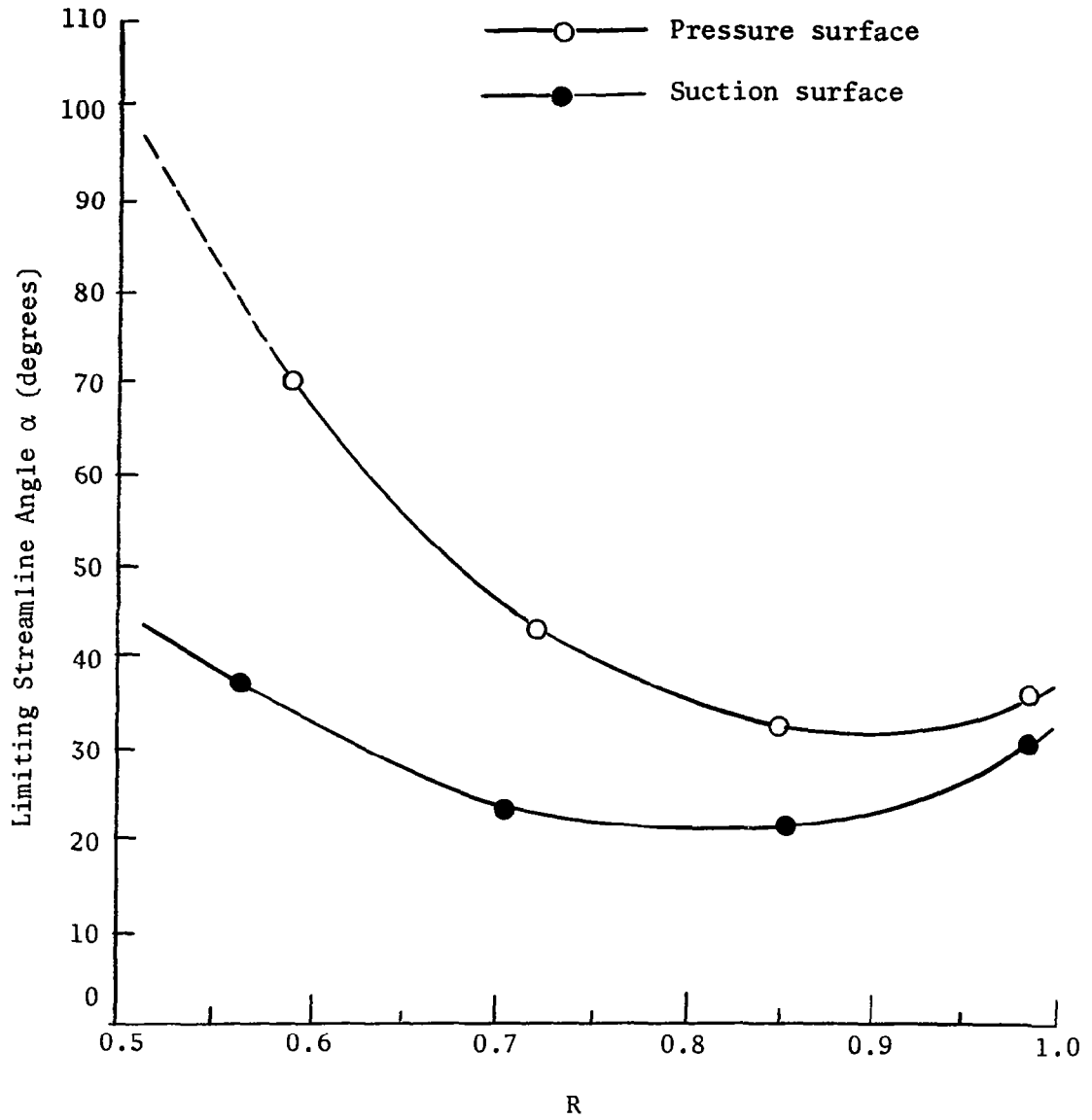
Figure 20.   Radial Variation of Limiting Streamline Angle
Near the Trailing Edge
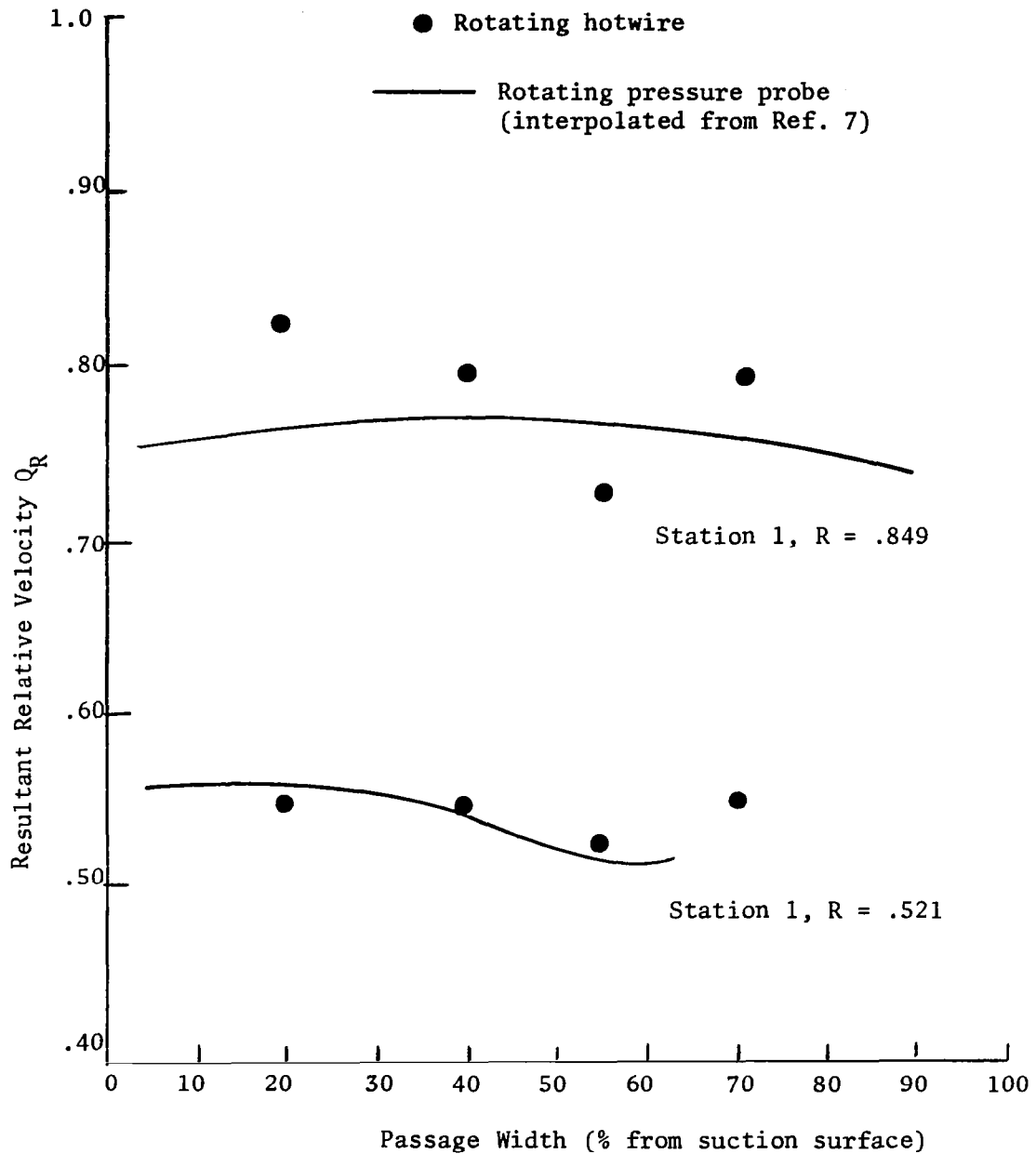
Figure 21. Comparison of Rotating Hotwire and Rotating
Pressure Probe Measurements
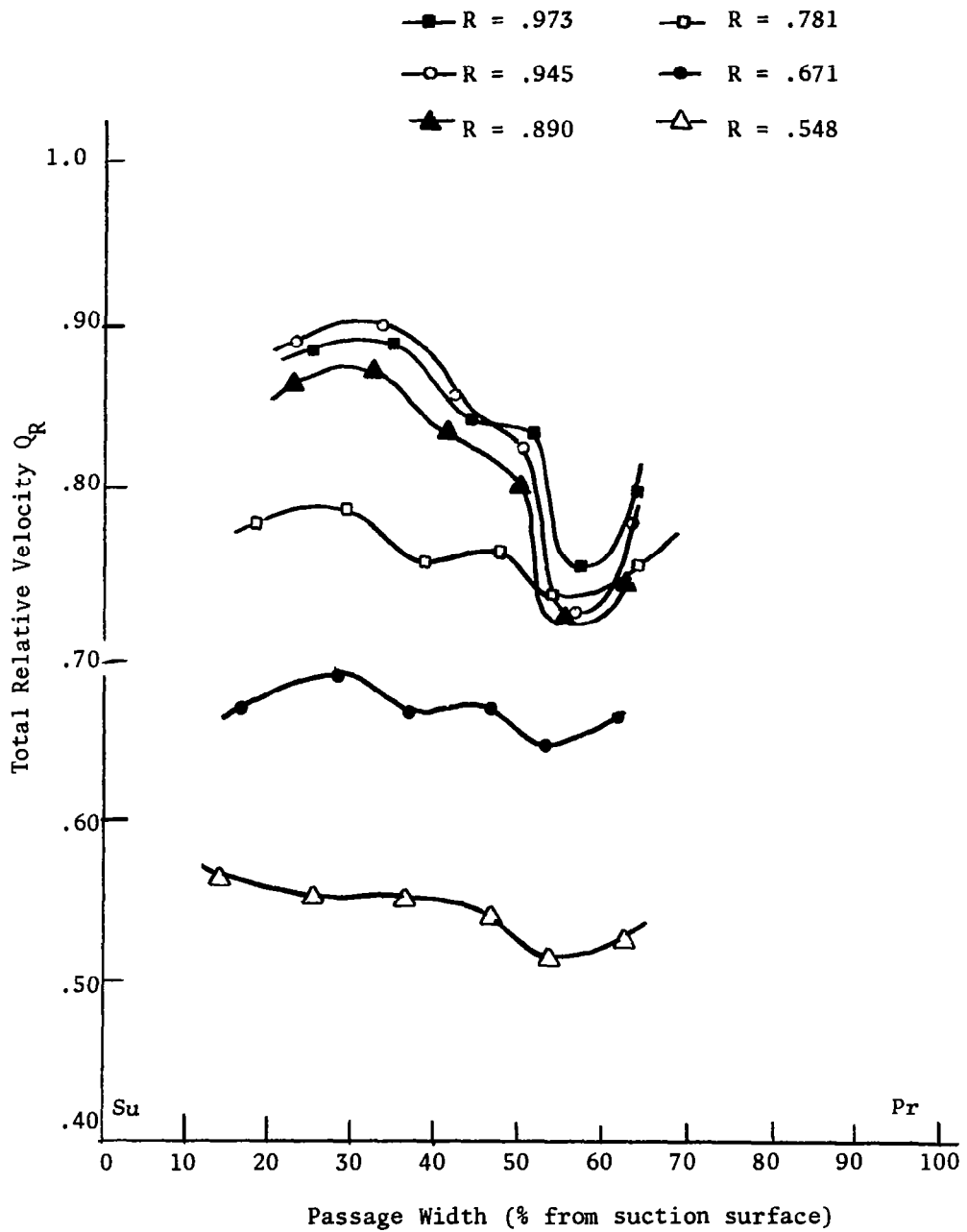
Figure 22. Total Relative Velocity Distribution
at Station 1

radii. A distinct velocity deficiency is noted at approximately 55%
from the blade suction surface for all radial stations, but it is
especially pronounced near the tip. This is the region of maximum loss.
The radial flows inside the pressure and suction surface boundary
layers, when encountered by the annulus wall, tend to roll toward mid-
passage, interact, and produce strong vortices and radially inward
flows. This interaction region is an area of considerable flow mixing,
resulting in strong eddies and the associated energy dissipation. A
concentration of high turbulence intensities in this region is confirmed
by qualitative measurement of the A. C. fluctuating hotwire voltages.
The radial variation of passage-averaged total relative velocity is
plotted in Fig. 23. The difference between the design and experi-
mental curves increases near the tip, further substantiating the
existence of three-dimensional effects and flow loss in this region.
The degradation in flow velocity near the tip also explains the
behavior of the $\overline{\psi}_s$ variation in Fig. 17a.

From the velocity profiles of Fig. 22, it is easy to discern the
suction surface boundary layer at radii above R = .671. The suction
surface boundary layer appears to grow in thickness as the tip is
approached, increasing to approximately 25% of the passage width. This
observation is consistent with the previous discussion about tip
boundary layer interaction. No evidence of the pressure surface
boundary layer can be detected in Fig. 22. This tends to indicate
that the suction surface boundary layer is thicker than that of the
pressure surface, although it should be remarked that no measurements
were taken close to the blade surface. Since the blade element is not
radial, the hotwire probe could not be located very close to the blade
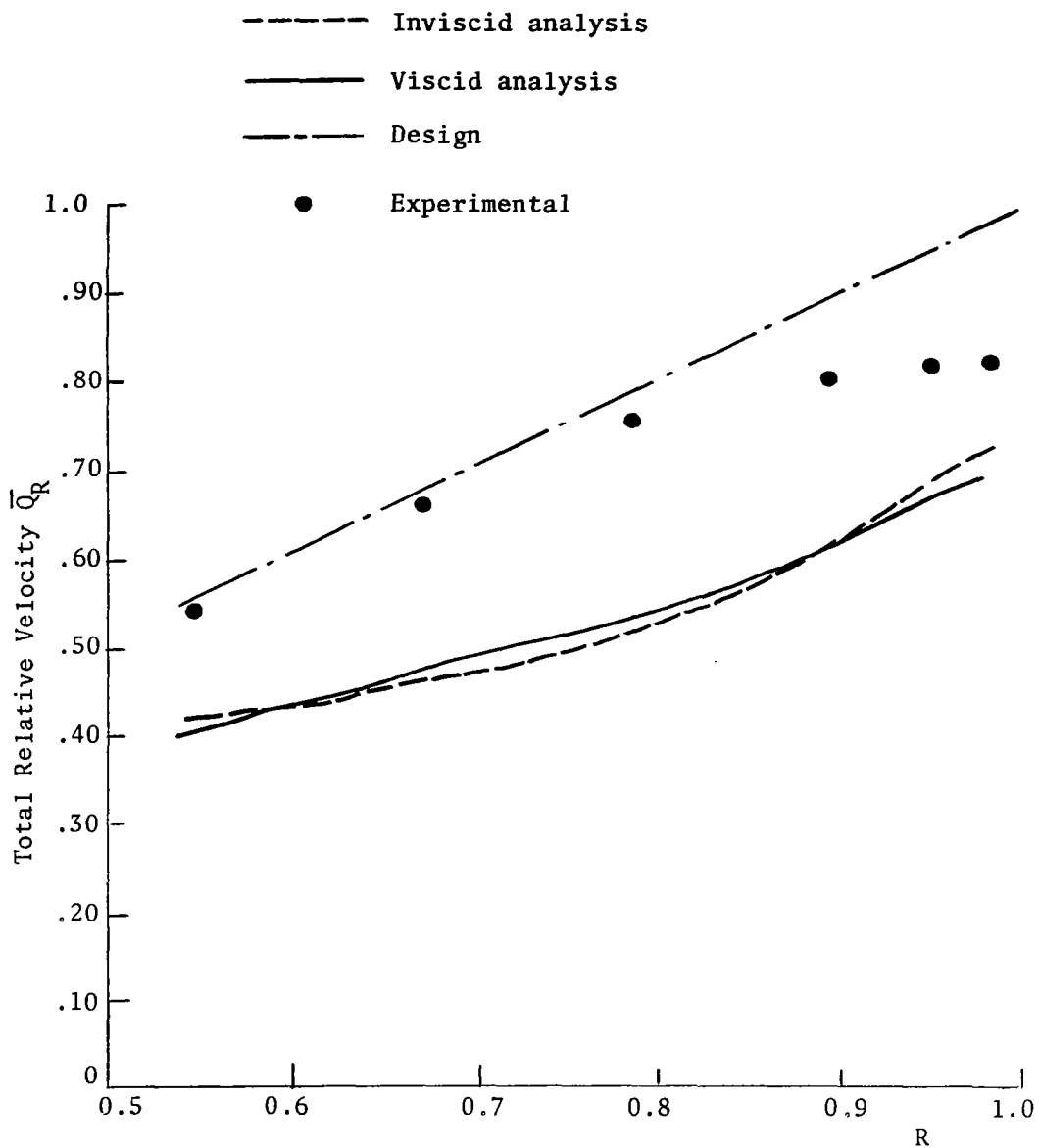
Figure 23. Radial Variation of Passage-Averaged
Total Relative Velocity at Station 1

surface while also assuring the correct orientation necessary for the data analysis described in the previous chapter.

Relative Tangential Velocity.- Fig. 24 shows the passage variation of relative tangential velocity V at the several radii. The magnitude and shape of these curves are almost identical to the total relative velocity curves of Fig. 22, indicating the dominance of the tangential flow within the inducer passage. Comments concerning the total relative velocity are also applicable here. Fig. 25 is a plot of the radial variation of passage-averaged relative tangential velocity and indicates the region of large flow loss that exists near the tip. The absolute tangential velocity can be derived from

$$C_\theta = R \ \Omega \ - V \qquad\qquad (54)$$

The high values of absolute tangential velocity near the tip indicates that the absolute stagnation pressure rise in this region is very large. This large absolute stagnation pressure rise is not due to flow turning but to the effects of complex viscous interactions.

Axial Velocity.- Fig. 26 shows axial velocity W plotted versus percentage of passage width. The general trend for the tangential variation of axial velocity indicates an increase from suction surface to pressure surface. The radial variation of the axial velocity shows the largest values occurring near the hub, decreasing consistently towards the tip. This tends to indicate the effect of blade blockage on the axial velocity distribution. It is noted from Fig. 26 that negative values of W occur at the tip location R = .973. The existence of negative axial velocities at the extreme tip location indicates the presence of the annulus wall boundary layer scraping effect and was
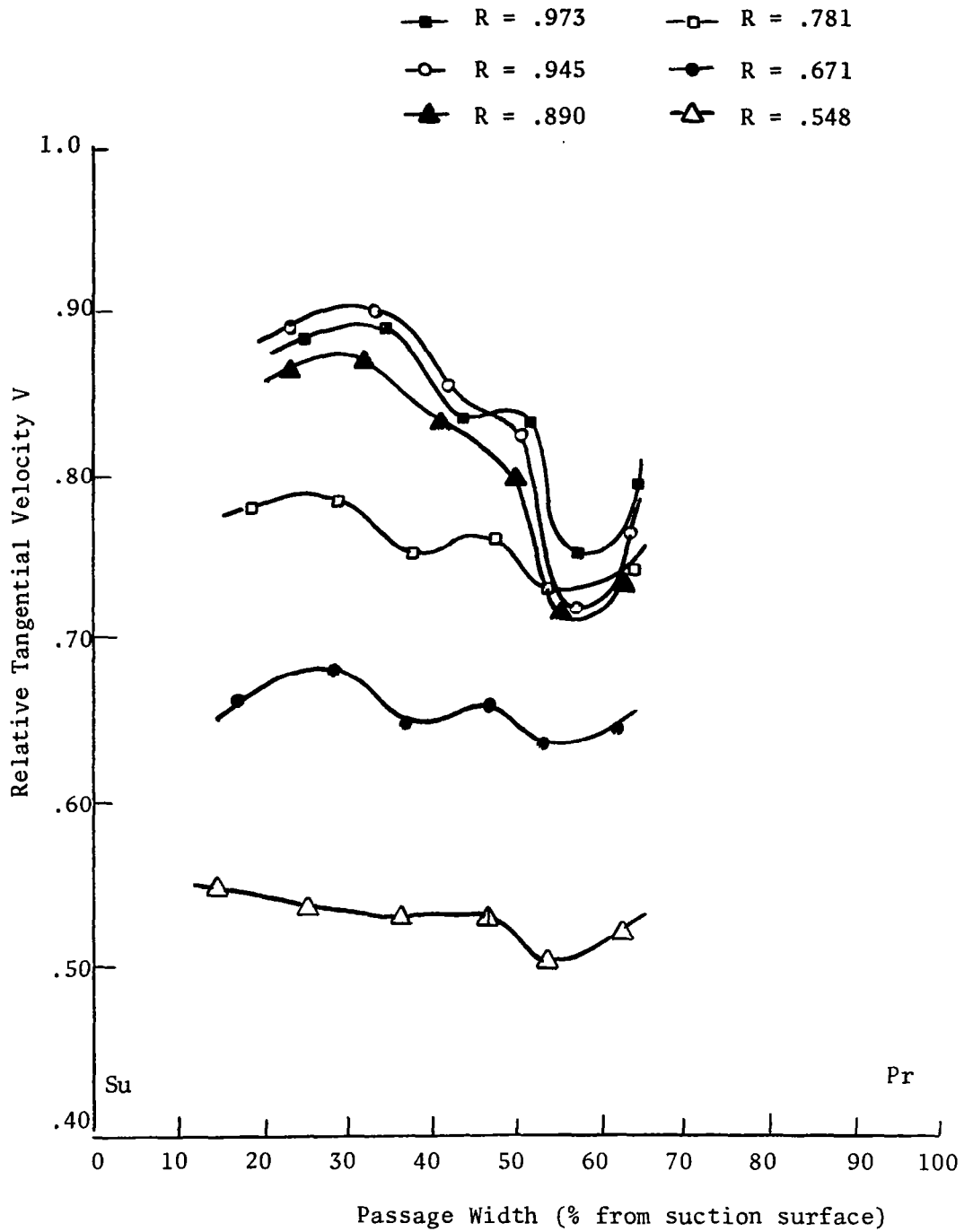
Figure 24. Relative Tangential Velocity Distribution
at Station 1
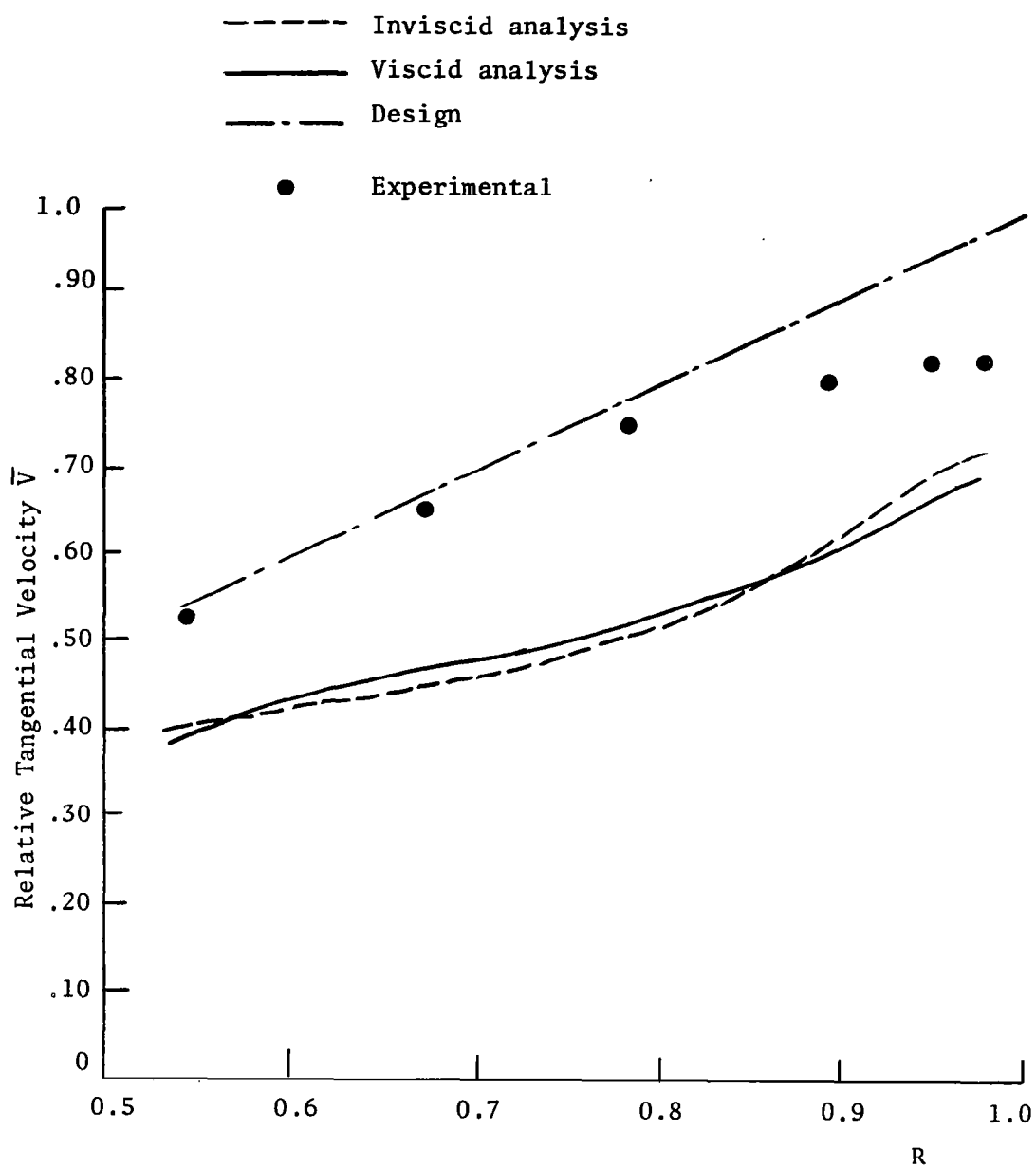
Figure 25.  Radial Variation of Passage-Averaged Relative
Tangential Velocity at Station 1
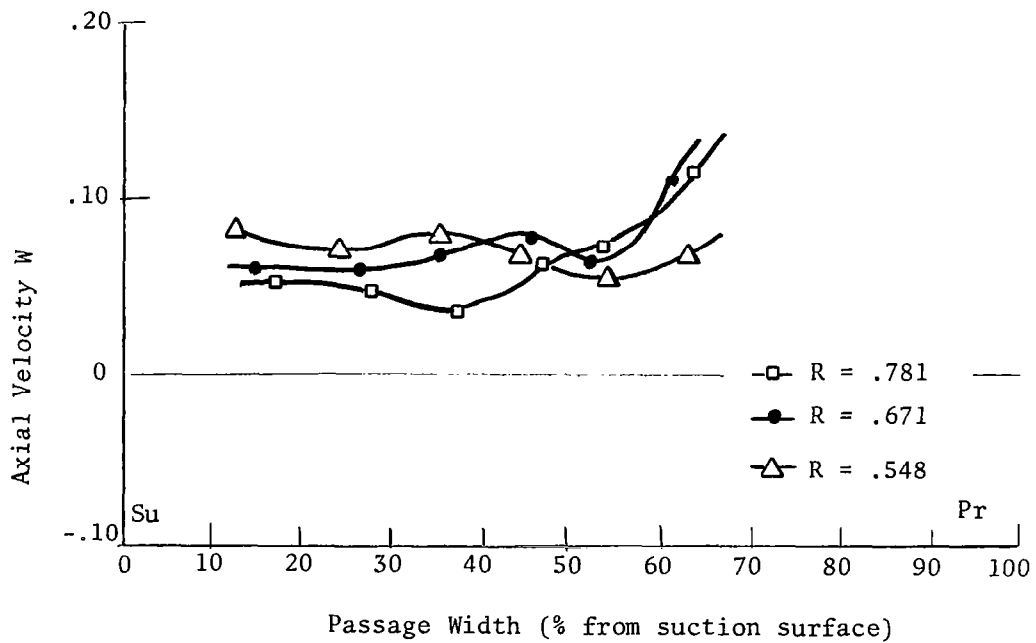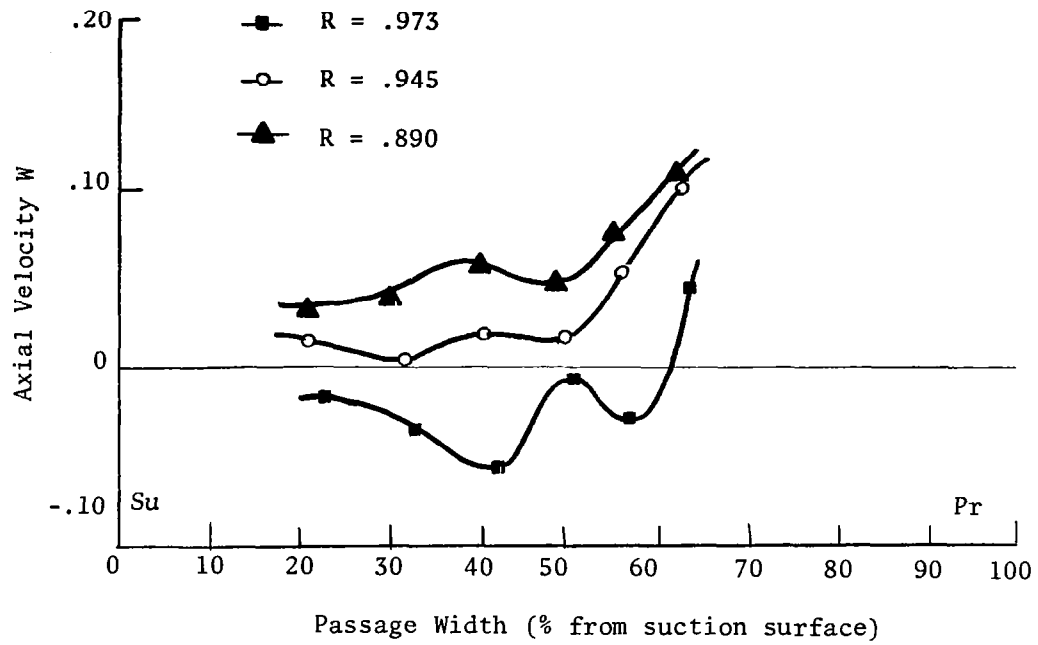
Figure 26.  Axial Velocity Distribution at Station 1

similarly noted by the limiting streamline angle measurements at this location.

It should be pointed out that the hotwire sensors used in the experimentation are not capable of distinguishing the direction of a velocity, only its magnitude. However, through the analysis of the previous chapter, hotwire equations are derived which assume an R-θ-Z coordinate system and require appropriate direction cosines to the orientation coordinate system of the hotwire. The resulting system of equations are solved numerically. It is from the numerical solution of these equations that negative values for the velocity components can appear, indicating that the positive axis of that particular velocity component was actually $180^{\circ}$ from that assumed in the measurement of the direction cosines. Thus it is possible, with the method derived in the previous chapter, to determine the magnitude and sense of the velocity vector measured by the hotwire sensors.

The radial variation of passage-averaged axial velocity is shown in Fig. 27a. The rapid decrease in axial velocity near the tip is evident. The validity of the axial velocity distribution can be ascertained by applying the continuity equation to the experimental results. Using

$$\pi \, r_t^2 \, W_1 = \int_{r_h}^{r_t} \rho 2\pi \, Wr dr \qquad (55)$$

where $W_1$ is the uniform axial velocity upstream of the inducer, the results agree favorably with the design value.

Radial Velocity.- Fig. 28 depicts the tangential variation of the radial velocity U. · Large values of U are found near the suction surface at radii close to the hub, indicating higher radially outward

(a)   Station 1
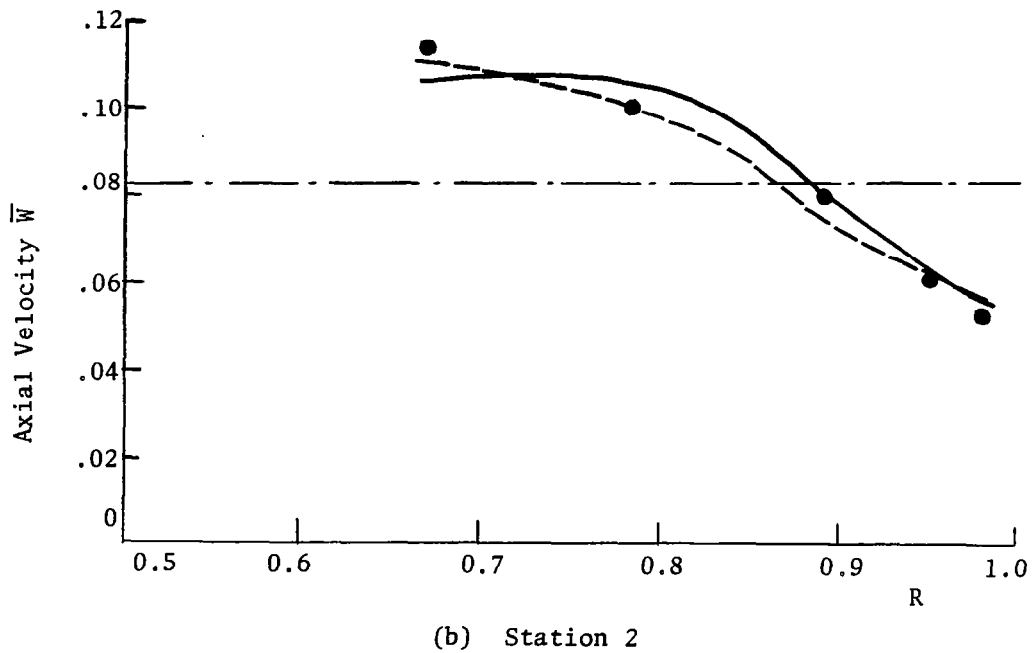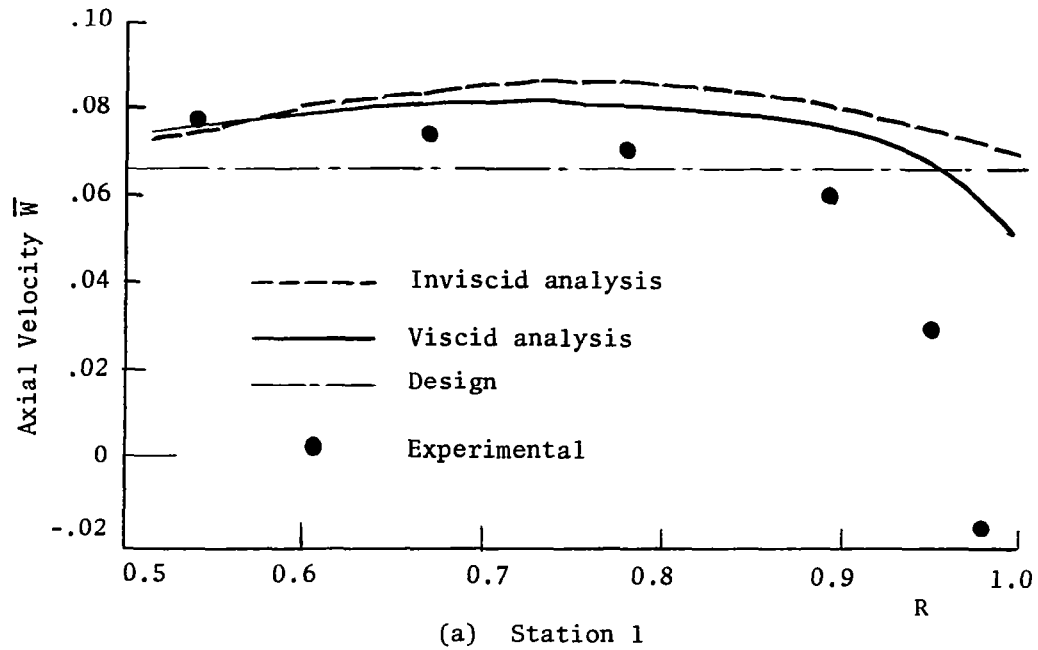
(b)   Station 2

Figure 27.   Radial Variation of Passage-Averaged Axial Velocity
at Stations 1 and 2
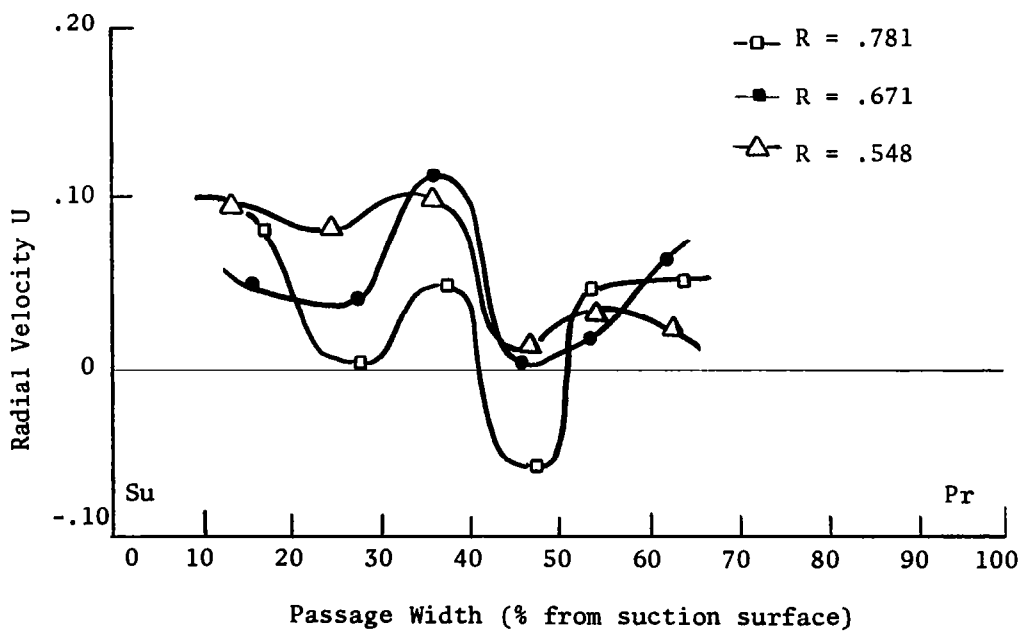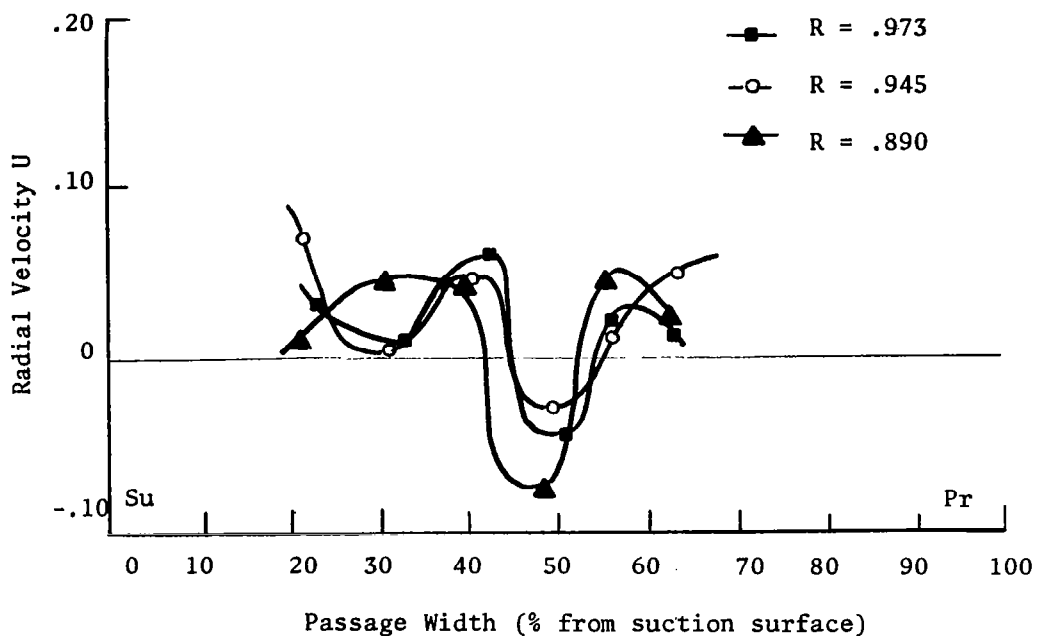
Figure 28. Radial Velocity Distribution at Station 1

flow in this region. Negative radial velocities are found at radii near the tip ($R = .781$ and greater), appearing at approximately 45% passage width. This is consistent with the previous discussions on boundary layer interaction and radially inward flow in this region. The rationale for obtaining negative velocity component values from the hotwire measurements was given in the previous section. Fig. 29a shows the radial variation of passage-averaged radial velocity. The values of U are quite large, indicating the appreciable three-dimensionality of the inducer flow. The radial velocities are of the same order of magnitude as the axial velocity. Fig. 29a indicates that the radial velocities are higher near the hub which confirms the conclusions of the blade limiting streamline measurements.

Measurements at Station 2

Total Relative Velocity.- The tangential variation of total relative velocity $Q_R$ is shown in Fig. 30a for each of the measuring stations. Again, as in station 1, a region of distinct velocity deficiency is noted near the tip. The explaination for the velocity deficiency in this area has been attributed to the large flow losses encountered as the result of boundary layer interaction and extensive flow mixing discussed fully in an earlier section. In comparison with the results of station 1 (Fig. 22), the position of the loss core appears to have shifted toward the suction surface to approximately 40% passage width. A growth in the dimensions of the eddy inside the passage is evident as the flow proceeds from station 1 to station 2.
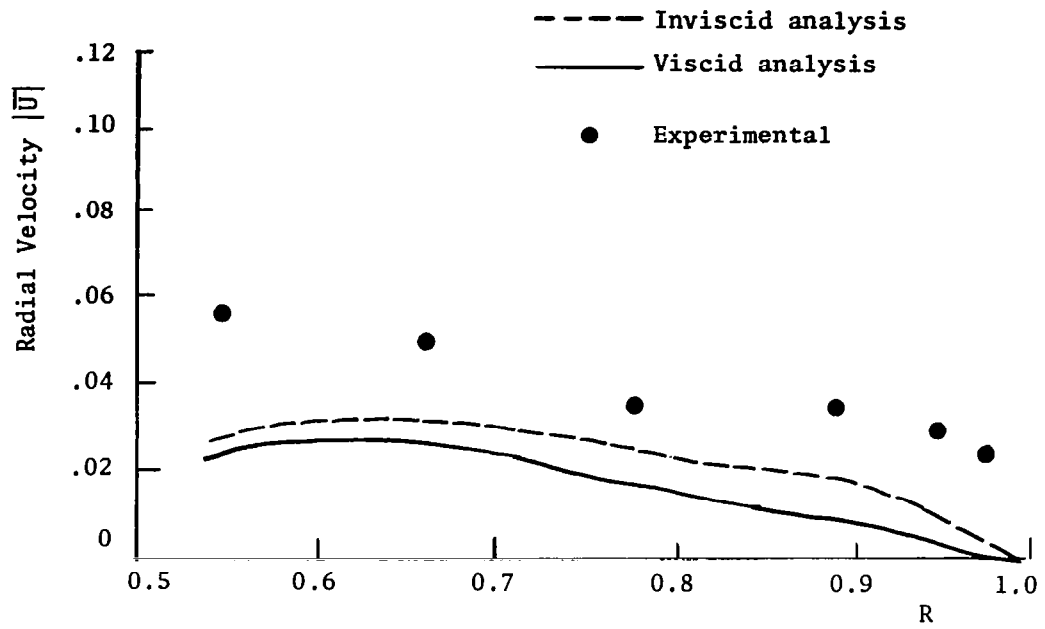
(a)  Station 1
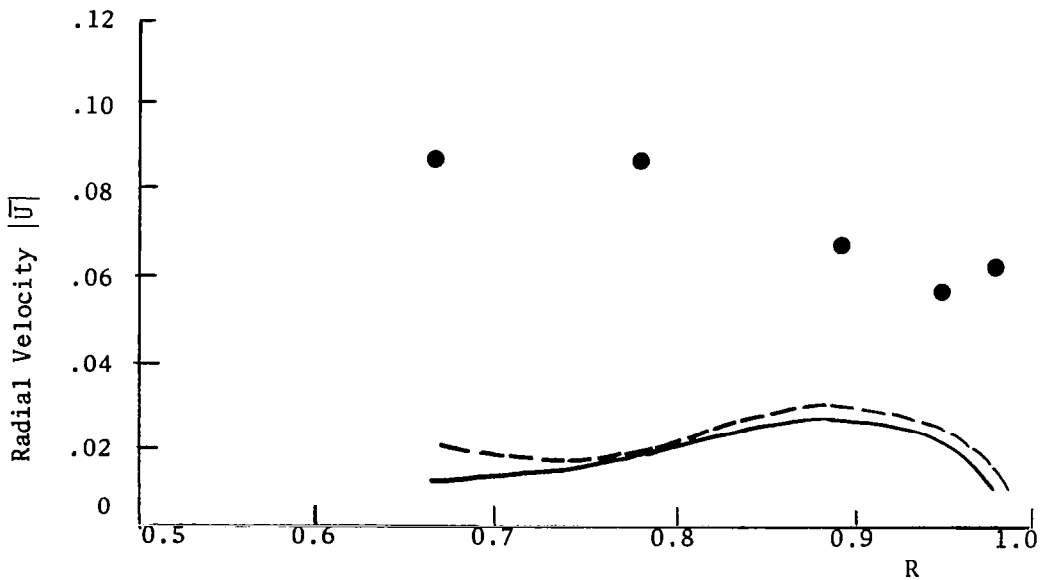
(b)  Station 2

Figure 29.  Radial Variation of Passage-Averaged
Radial Velocity at Stations 1 and 2
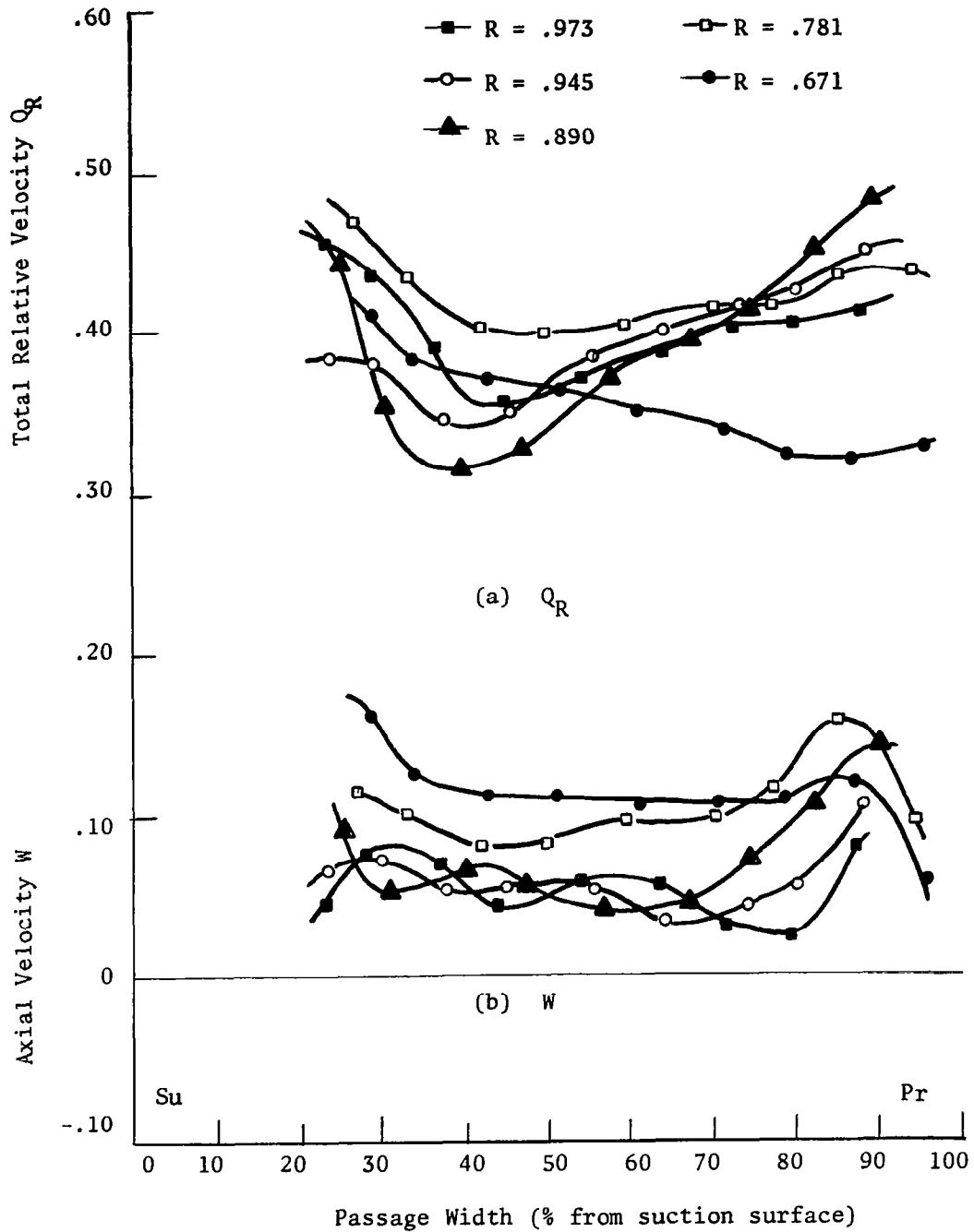
Figure 30. Total Relative Velocity and Axial Velocity
Distributions at Station 2

The radial variation of passage-averaged total relative velocity is plotted in   Fig. 31.   The values of $\overline{Q_R}$ are considerably less than the design values, substantiating the effects of three-dimensionality on the inducer flow.  The difference between the design curve and experimental results increases noticeably near the tip, further defining the region of large flow losses discussed previously.  Comparison of Fig. 31 and Fig. 23 confirms the increase in size of the loss core within the blade passage as the flow proceeds downstream.  This observation is also consistent with the behavior of the $\overline{\psi_s}$   variations shown in Fig. 17.

The extent of boundary layer growth on both the pressure and suction surface can be vaguely discerned in Fig. 30a, extending to approximately 20% passage width on the suction surface and to approximately 10% passage width or less on the pressure surface.

Relative Tangential Velocity. -   Fig. 32a gives the variation of relative tangential velocity V across the passage width.   Deviations from the total relative velocity profiles of  Fig. 30a are slight, again indicating the dominance of tangential flow within the long, narrow inducer blade passages.  In  Fig. 33,  the radial variation of passage-averaged relative tangential velocity is plotted.  The region of large decrease in relative velocity can be easily discerned. Comments concerning total relative velocity in the previous section are also applicable here.  This plot shows a significant departure from design values at all radii, the difference increasing rapidly as the tip is approached.  These low relative velocities (or high absolute velocities) indicate an extremely large absolute stagnation pressure rise within the region and, thus, are an indication of the extent to
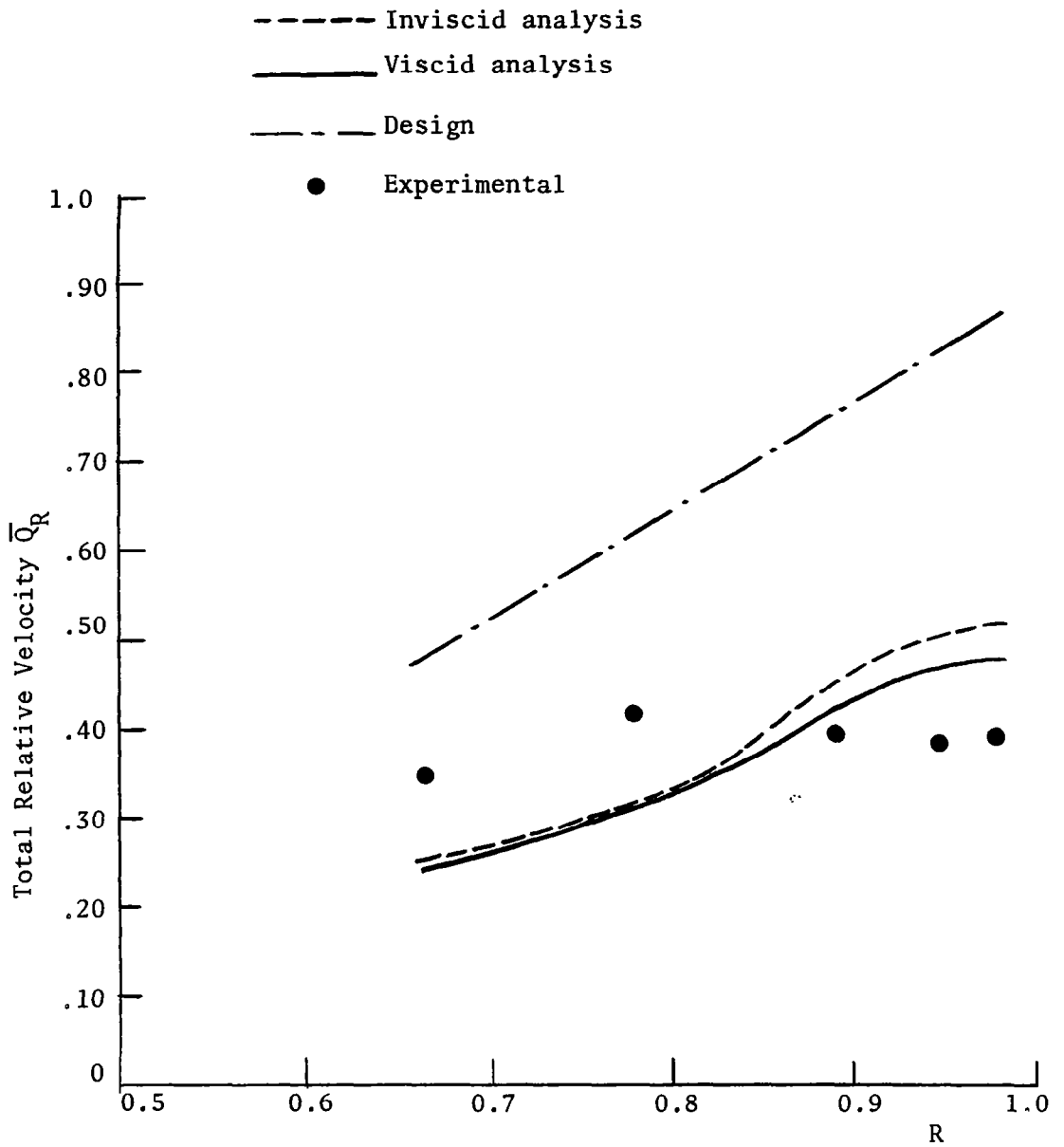
Figure 31.  Radial Variation of Passage-Averaged
Total Relative Velocity at Station 2
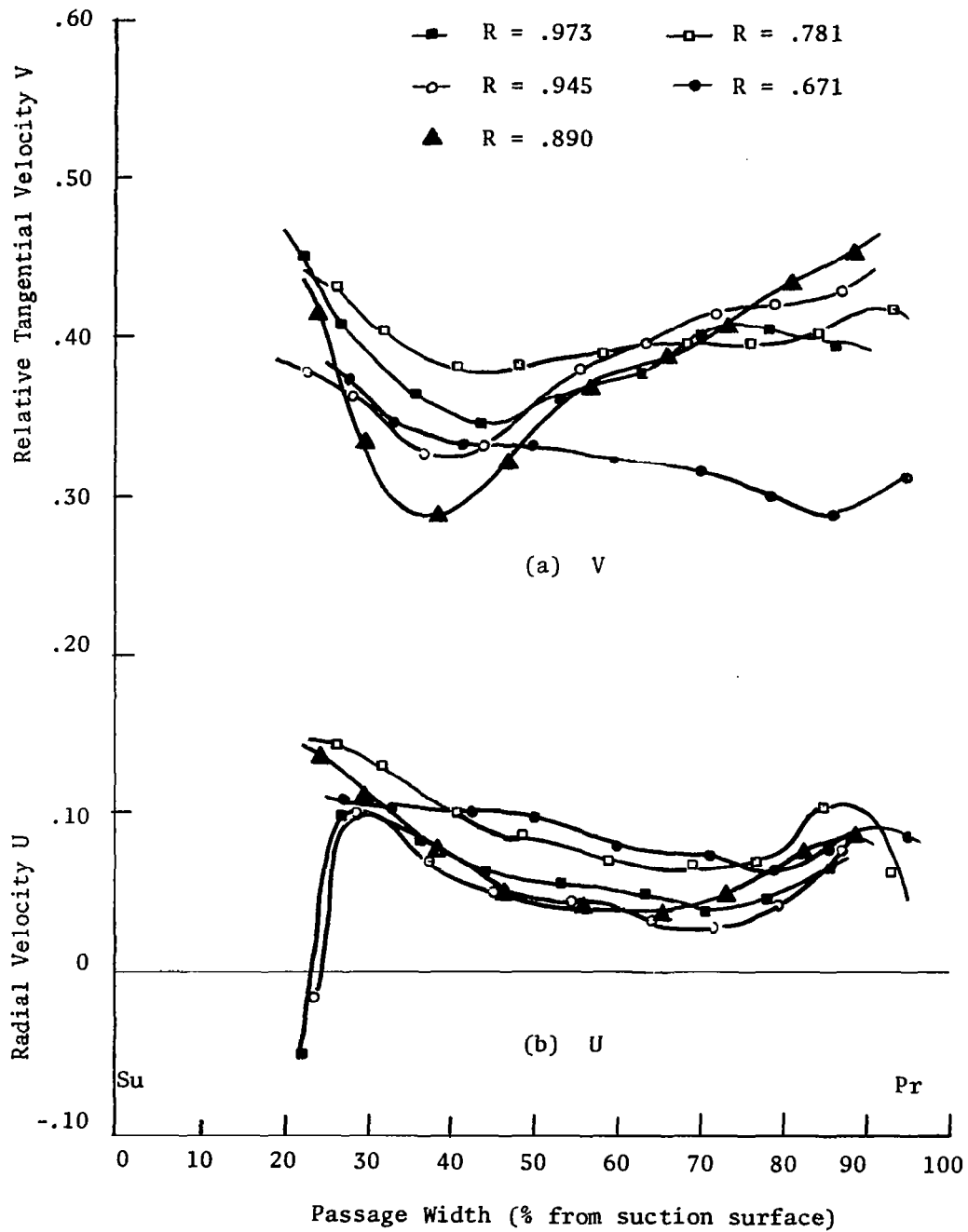
Figure 32.   Relative Tangential Velocity and Radial
Velocity Distributions at Station 2
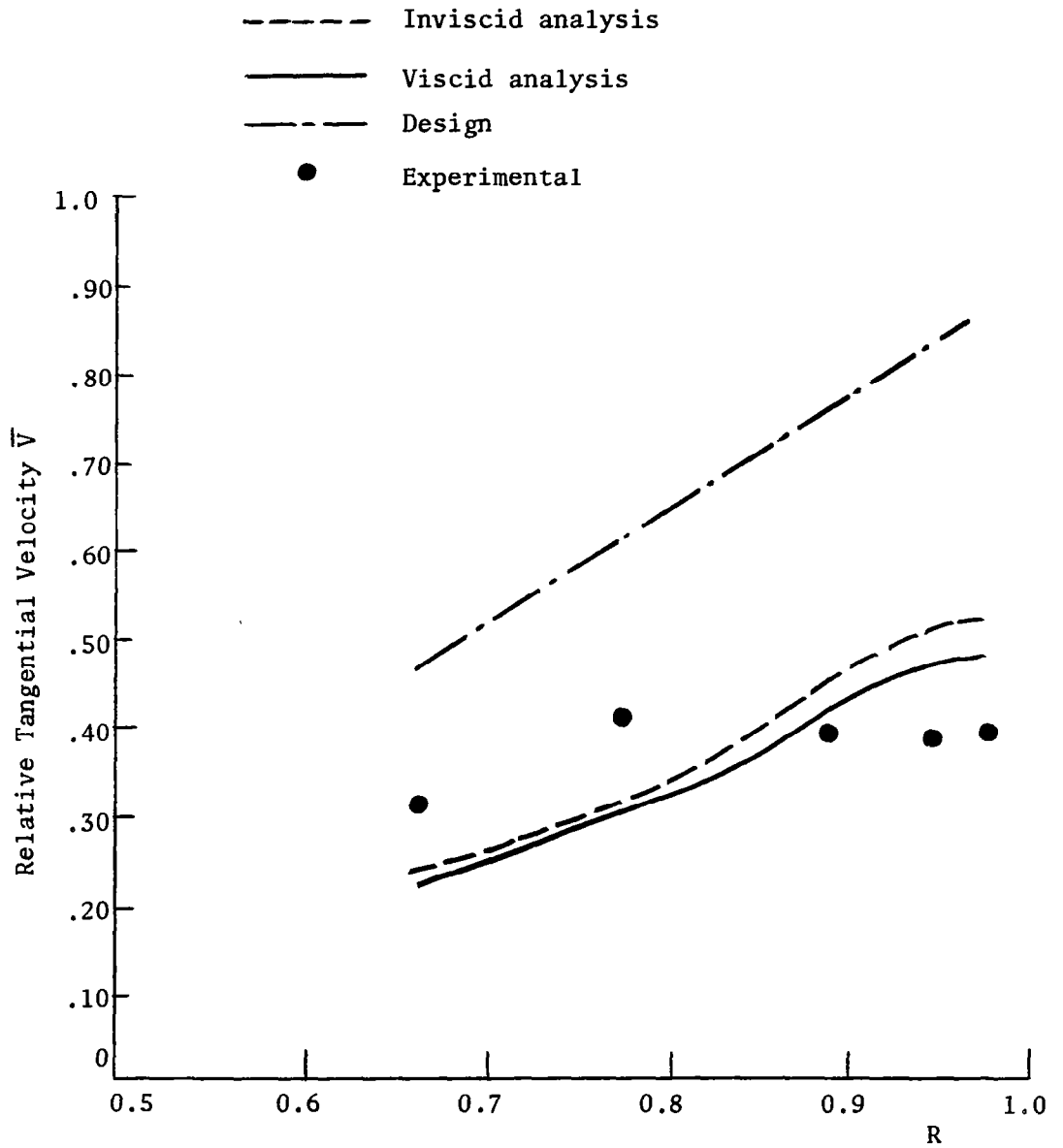
Figure 33. Radial Variation of Passage-Averaged Relative Tangential Velocity at Station 2

which complex viscid interactions are taking place. Comparison of Fig. 33 with Fig. 25 for station 1 clearly demonstrates the increase in size and severity of the loss core as the flow within the inducer passage proceeds downstream.

Axial Velocity.- The tangential variation of axial velocity W is given in Fig. 30b for the various experimental radii. Overall magnitudes are, of course, higher than those measured at station 1 (Fig. 26) due to the converging annulus. Again, as in station 1, the radial distribution of passage-averaged axial velocity (Fig. 27b) shows larger values occurring near the hub indicating the continuing presence of the blade blockage effect. It is interesting to note that the opposite trend was found in Ref. 20 at locations downstream of the trailing edge where no blade blockage effects should be present. This implies that significant changes occur in the axial velocity profile as the flow leaves the rotating inducer channel and proceeds downstream. These changes may be responsible, in part, for the backflow region previously reported in Ref. 10 near the hub trailing edge and confirmed by the blade limiting streamline angle measurements of this report. Due to physical restraints, rotating hotwire measurements were not conducted close enough to the inducer hub to permit detection of backflows near the hub surface. The decrease in axial velocity near the tip, as shown in Fig. 27b, indicates the continuing presence of the annulus wall boundary layer scraping effect. The effect, however, is not as severe as at station 1 where negative axial velocities were measured (Fig. 27a). Application of the continuity equation (equation 55) to the experimental results of Fig. 27b indicates good agreement with the design value.

An examination of Fig. 30b reveals a well-defined pressure surface boundary layer at R = .671 and R = .781 which extends approximately 15% of the passage width. It appears that the boundary layer is thicker in this region than at the tip locations. Conversely, the suction surface boundary layer is well-defined near the tip at R = .973 and R = .945, extending approximately 30% of the passage width and indicating that the suction surface boundary layer increases in thickness as the tip is approached.

Radial Velocity.- The variation of radial velocity U across the passage is shown in Fig. 32b. The overall magnitudes appear larger than at station 1. Thus, the three-dimensional flow effects will be greater at station 2 and therefore accounts for the greater deviation of the flow from the two-dimensional design values which has been observed at this location (Fig. 31). Fig. 32b indicates negative radial velocities for the radii near the tip at approximately 25% from the suction surface. The radially inward flow at this location agrees with the previous discussions on boundary layer interaction and flow mixing which result in the velocity deficiencies and flow loss experienced in this region. Fig. 29b shows the radial variation of passage-averaged radial velocity. The significant radial flows are evident and this reflects the extent of three-dimensionality in the flow. As in station 1, the radial velocities are of the same order of magnitude as the axial velocities. Fig. 29b indicates that the radial velocities are higher near the hub, and comparison with Fig. 29a confirms the increase in radial velocities as the flow proceeds from station 1 to station 2. Both of these results confirm the observations of the blade limiting streamline angle measurements discussed in a previous section.

It is apparent from the discussions of radial flows at stations 1 and 2 that radial velocities are significant within the inducer passages and, thus, any serious attempt to predict inducer flows must rely on a three-dimensional analysis.

## Turbulence Intensities and Stresses

The distributions of tangential, axial and radial turbulence intensities at station 2, nondimensionalized with respect to local total relative velocity, are shown in isocontour form in Figs. 34, 35, and 36 respectively. The contours for all three intensity components are essentially the same, showing a "pocket" or "core" of high turbulence centered at approximately 40% passage width and R = .890. This coincides with the location of the maximum total relative velocity deficiency noted in Fig. 30a. The turbulence intensities are generally higher than those encountered in stationary passage. The peak intensities occur in the mixing region near the tip, where the two boundary layers merge and generate considerable flow mixing. The flow energy dissipated during this process is responsible for the velocity deficiencies encountered near the tip region in Fig. 30a. Another concentration of high turbulence is noted near the hub pressure surface and is an indication of the proximity to the pressure surface boundary layer. The radial turbulence intensities $\sqrt{\overline{u^2}}$ are generally higher than those in the axial and tangential directions, an indication of the violent radial motions occurring within the long narrow passages of the inducer. An isocontour plot of total turbulence energy at station 2, defined as

$$q^2 = \overline{u^2} + \overline{v^2} + \overline{w^2} \tag{56}$$
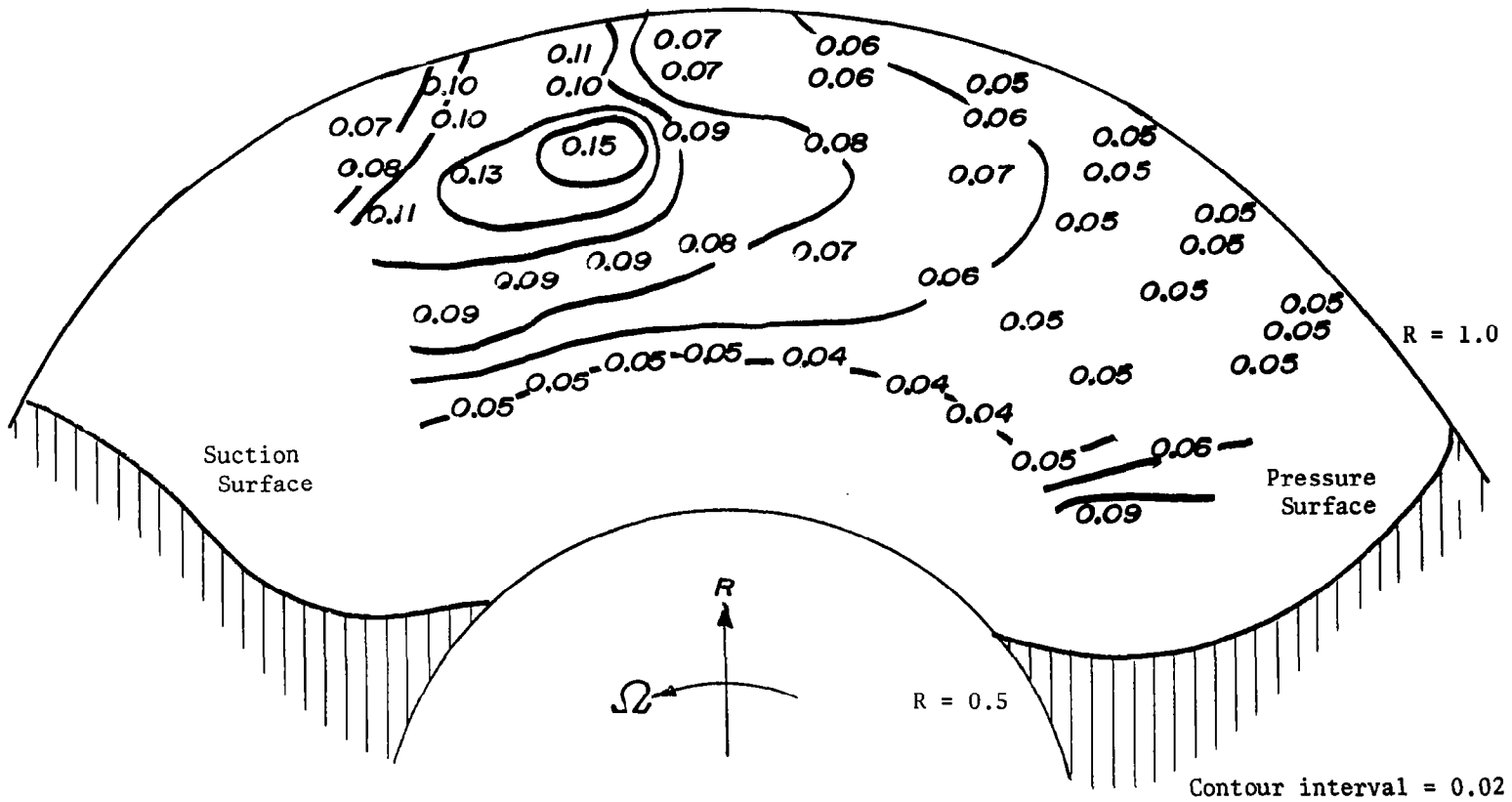
Figure 34. Tangential Turbulence Intensity ($\sqrt{\overline{v^2}}/Q_R$) at Station 2
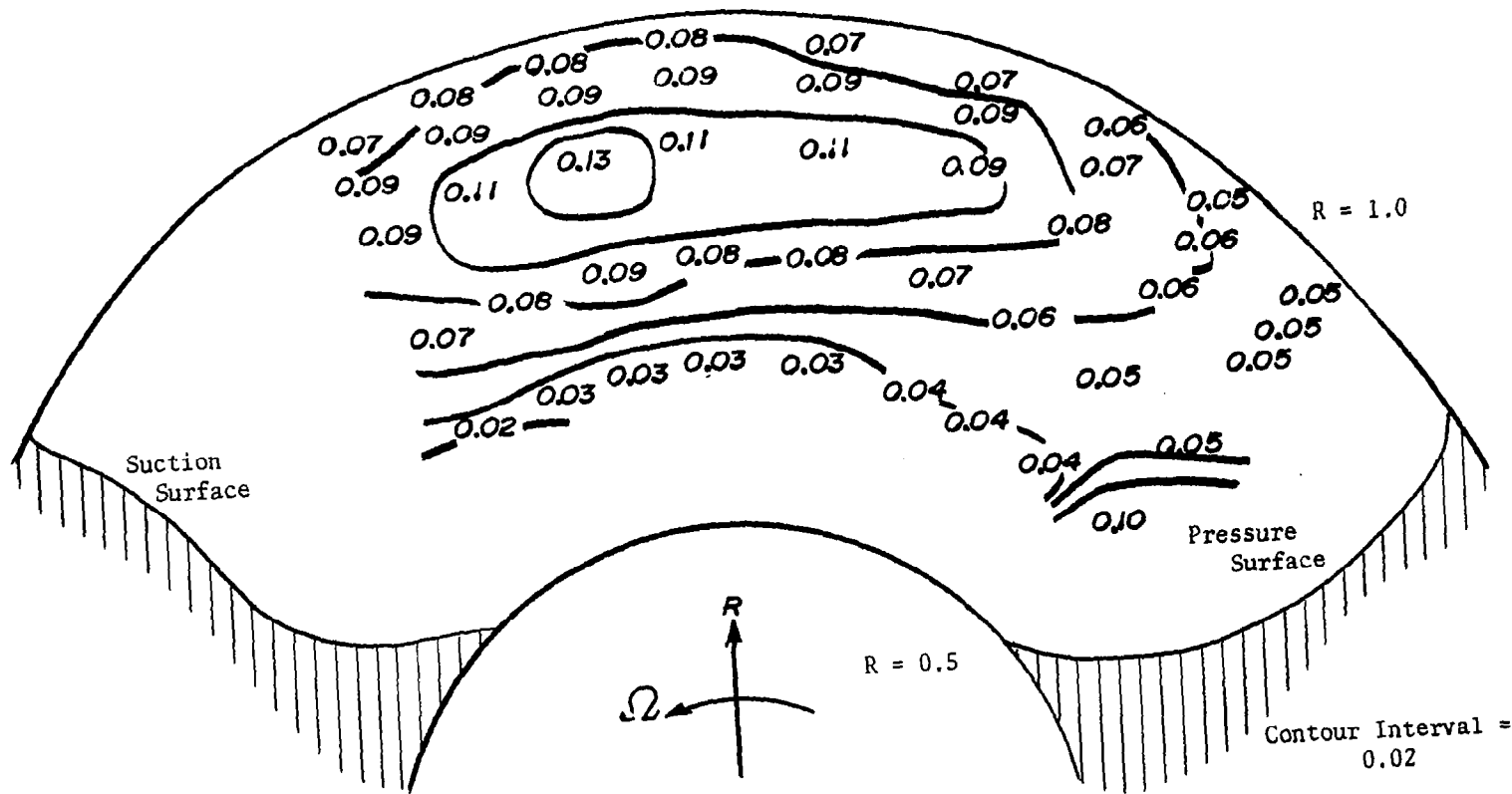
Figure 35. Axial Turbulence Intensity ($\sqrt{\overline{w^2}}/Q_R$) at Station 2
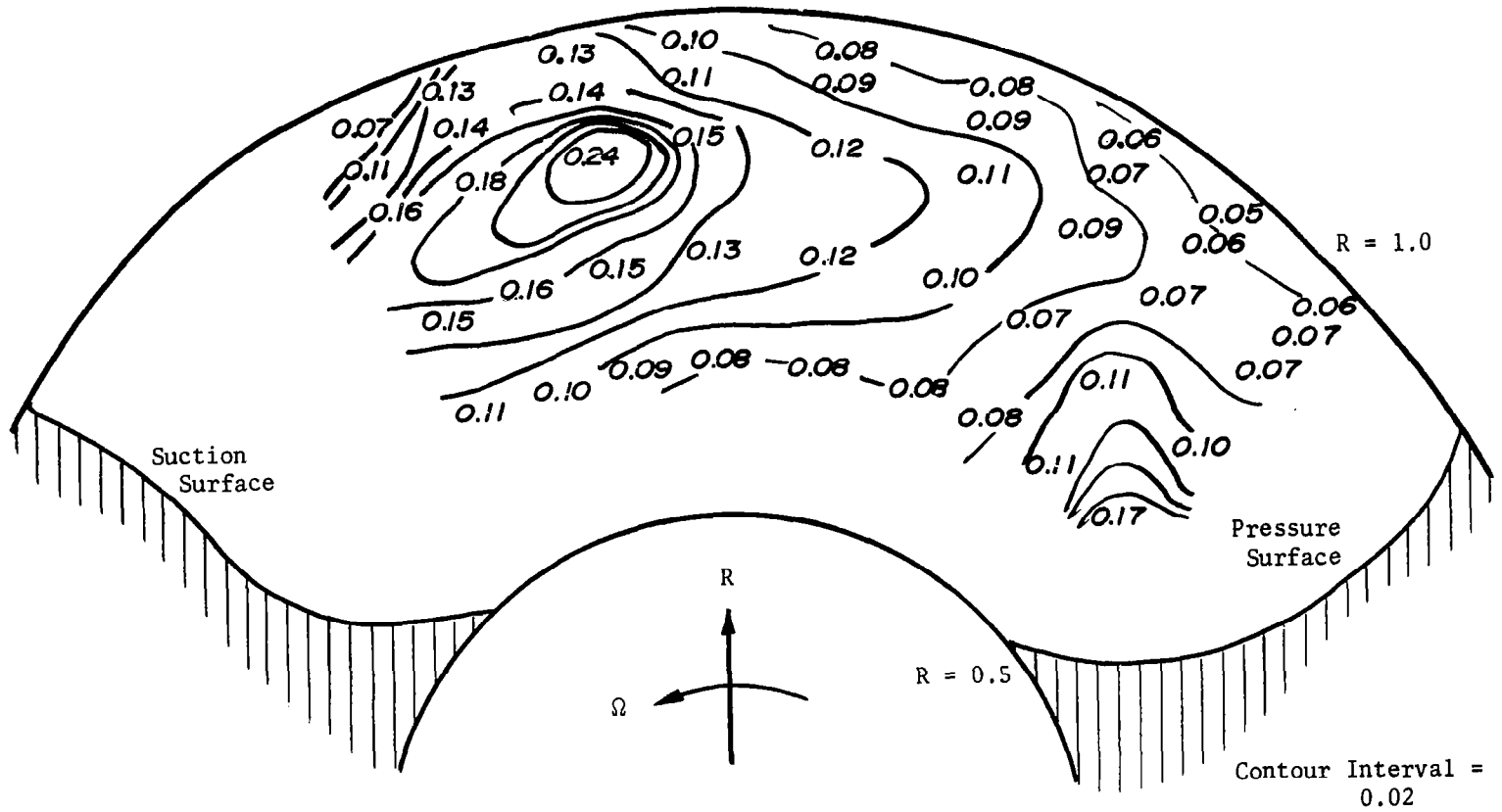
Figure 36. Radial Turbulence Intensity $(\sqrt{\overline{u^2}}/Q_R)$ at Station 2

is given in Fig. 37. It essentially reflects the observations
stated above, indicating high turbulence energy regions near the tip
at approximately 40% passage width and near the hub pressure surface.
It should be remarked that all the measurements reported here were
taken away from the blade surfaces. The maximum turbulence intensities
and stresses are likely to occur near the blade surfaces. High turbu-
lence intensities measured away from the blade surfaces and reported
here reflect the extent of turbulent mixing even near the mid-passage.
The classical assumption that the viscous and turbulence effects are
confined to very thin regions near the blade surfaces is evidently
inapplicable to inducers and hence, a fully three-dimensional treatment
is needed for the prediction of inducer flows.

The distributions of turbulence velocity correlations $\overline{uv}$, $\overline{uw}$ and
$\overline{uw}$ at station 2, nondimensionalized with respect to $Q_R^2$, are given in
isocontour form in Figs. 38, 39, and 40 respectively. These
correlations are indicative of the stresses occurring within the
inducer passage. Concentrations in stress intensities are similar to
the turbulence intensity contours discussed previously. The maximum
stresses occur in the mixing region near the tip at approximately 40%
passage width. The radial stresses are by far the most dominant and
emphasize the significant extent of three-dimensionality and complex
viscous interaction occurring within the inducer channel, especially in
the mixing region. As mentioned previously, the stresses shown in
Figs. 38-40 represent values away from the blade surfaces. Stress
values near the blade surface are likely to be high. The higher stress
values noted near the hub pressure surface in Figs. 38-40 are an indi-
cation of the proximity to the pressure surface boundary layer.
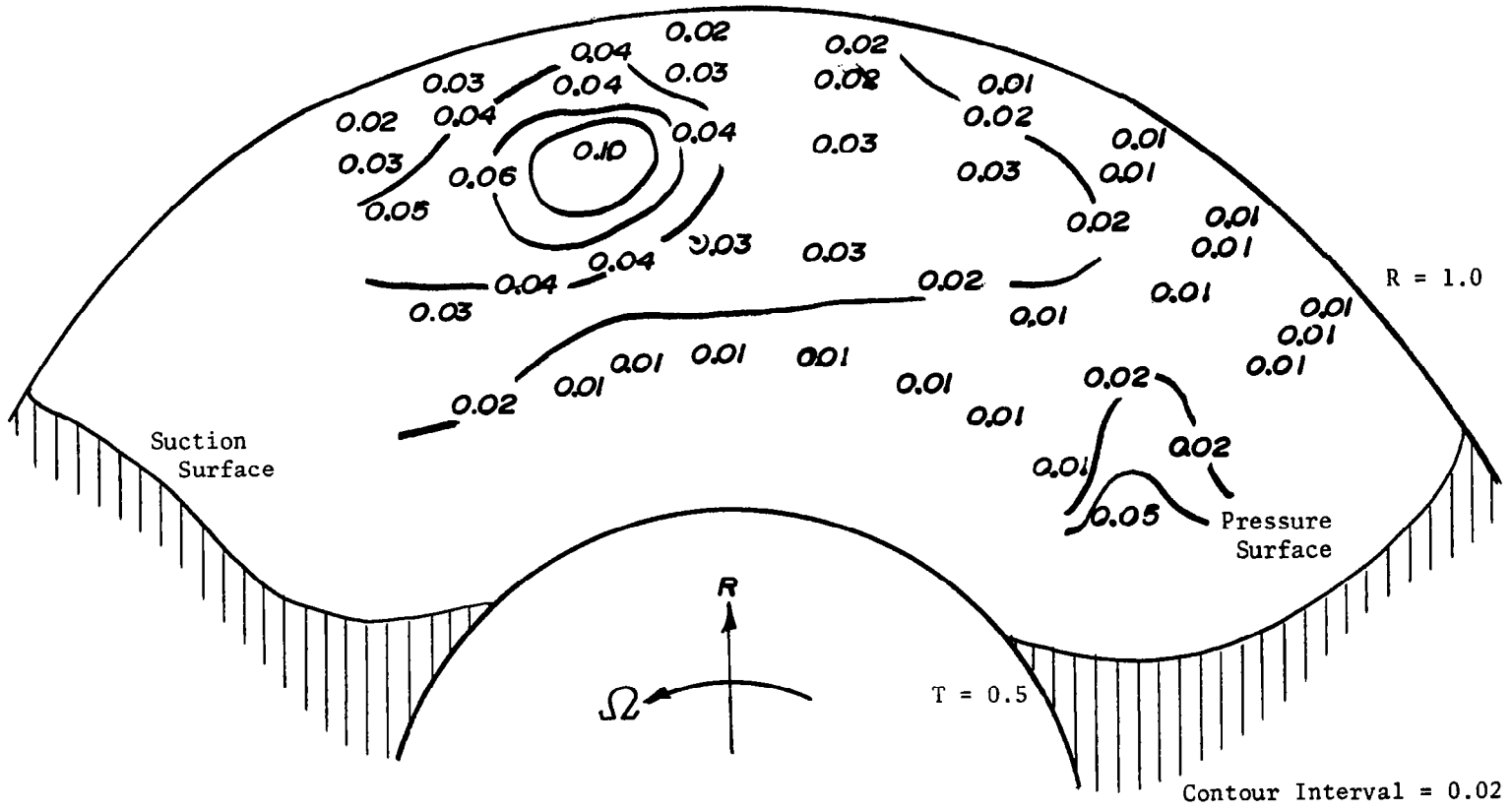
Figure 37. Total Turbulence Energy ( $\overline{q^2}/Q_R^2$ ) at Station 2
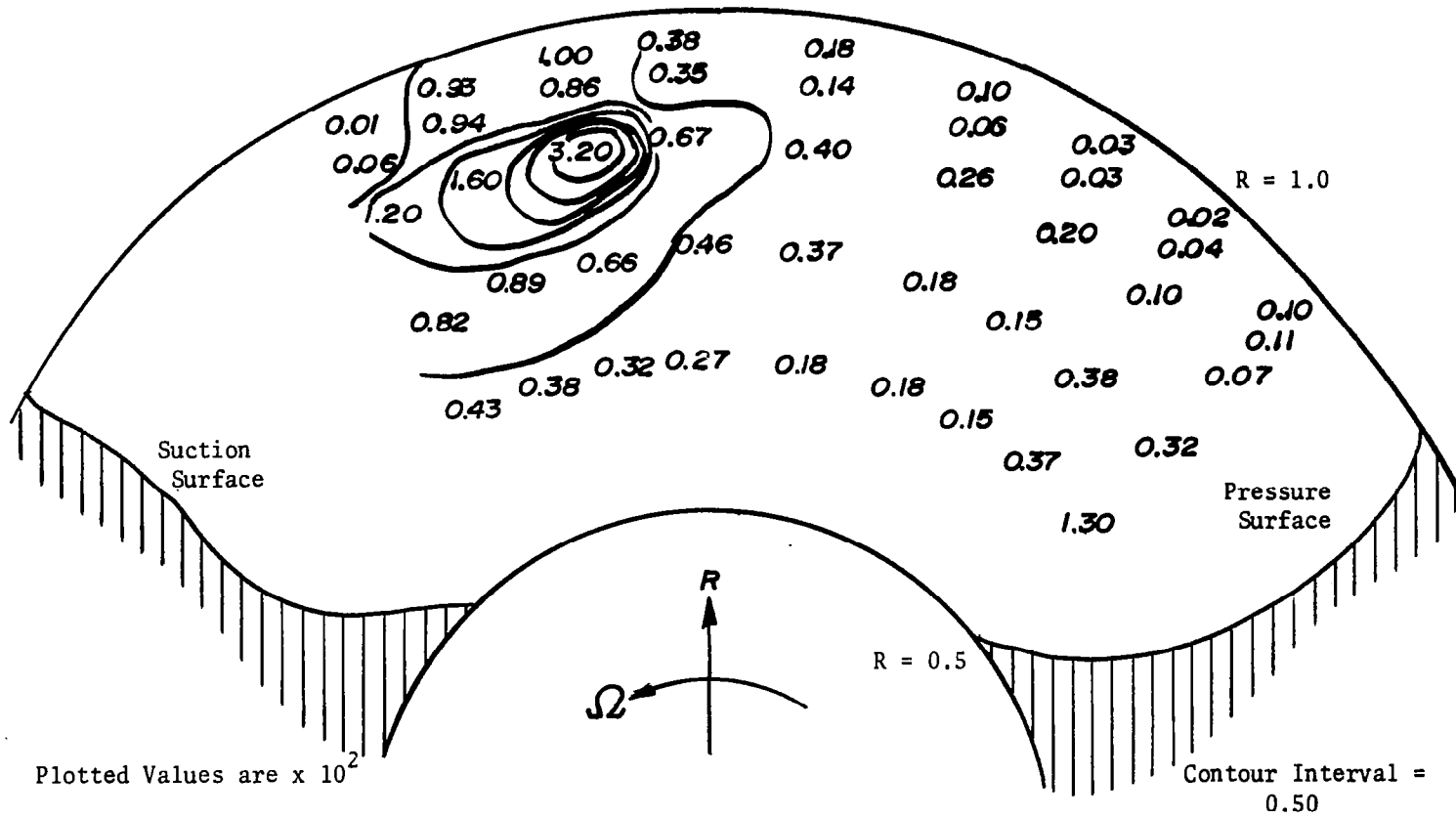
Figure 38. Turbulence Velocity Correlation ($\overline{uv}/Q_R^2$) at Station 2
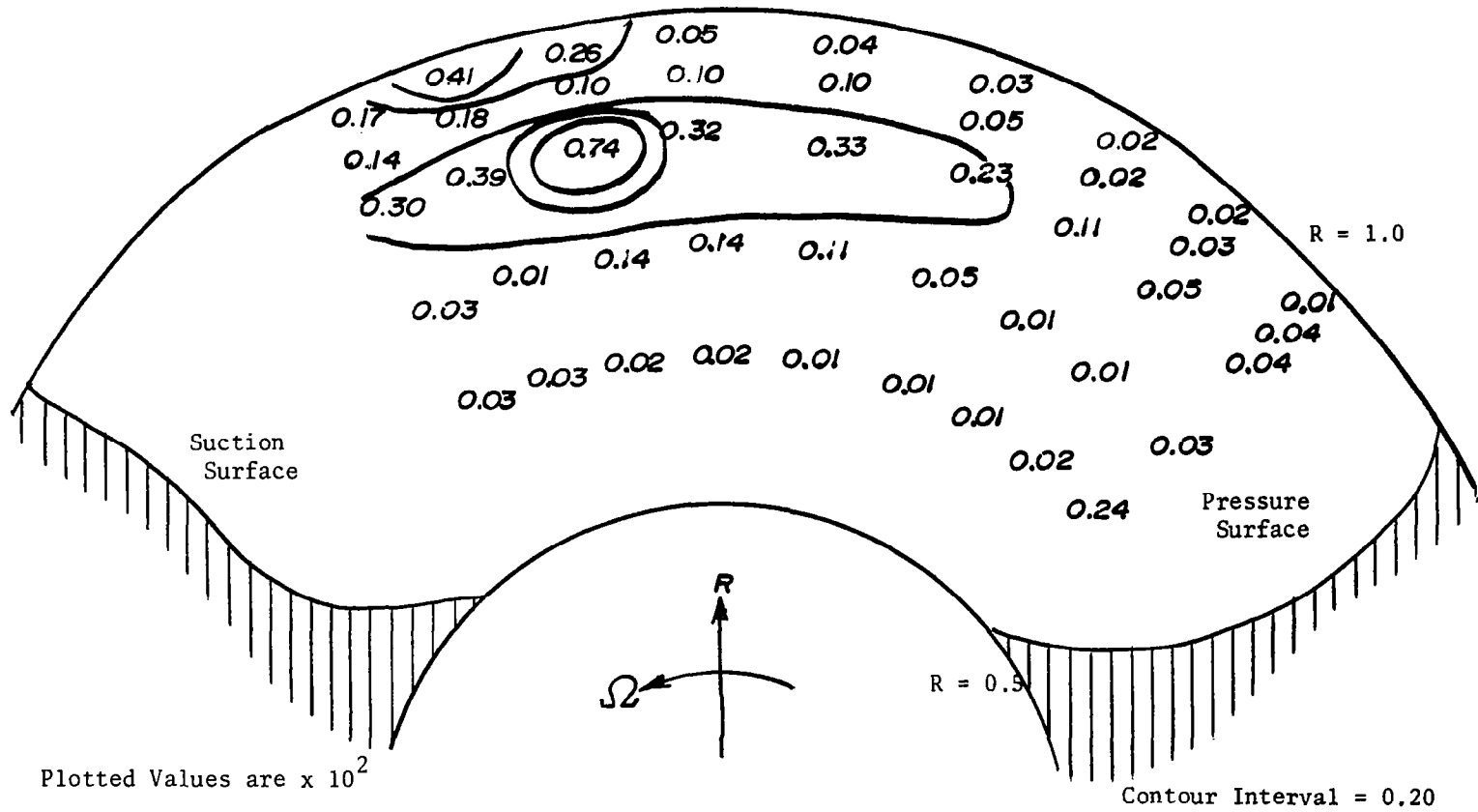
Figure 39. Turbulence Velocity Correlation $(\overline{uw}/Q_R^2)$ at Station 2
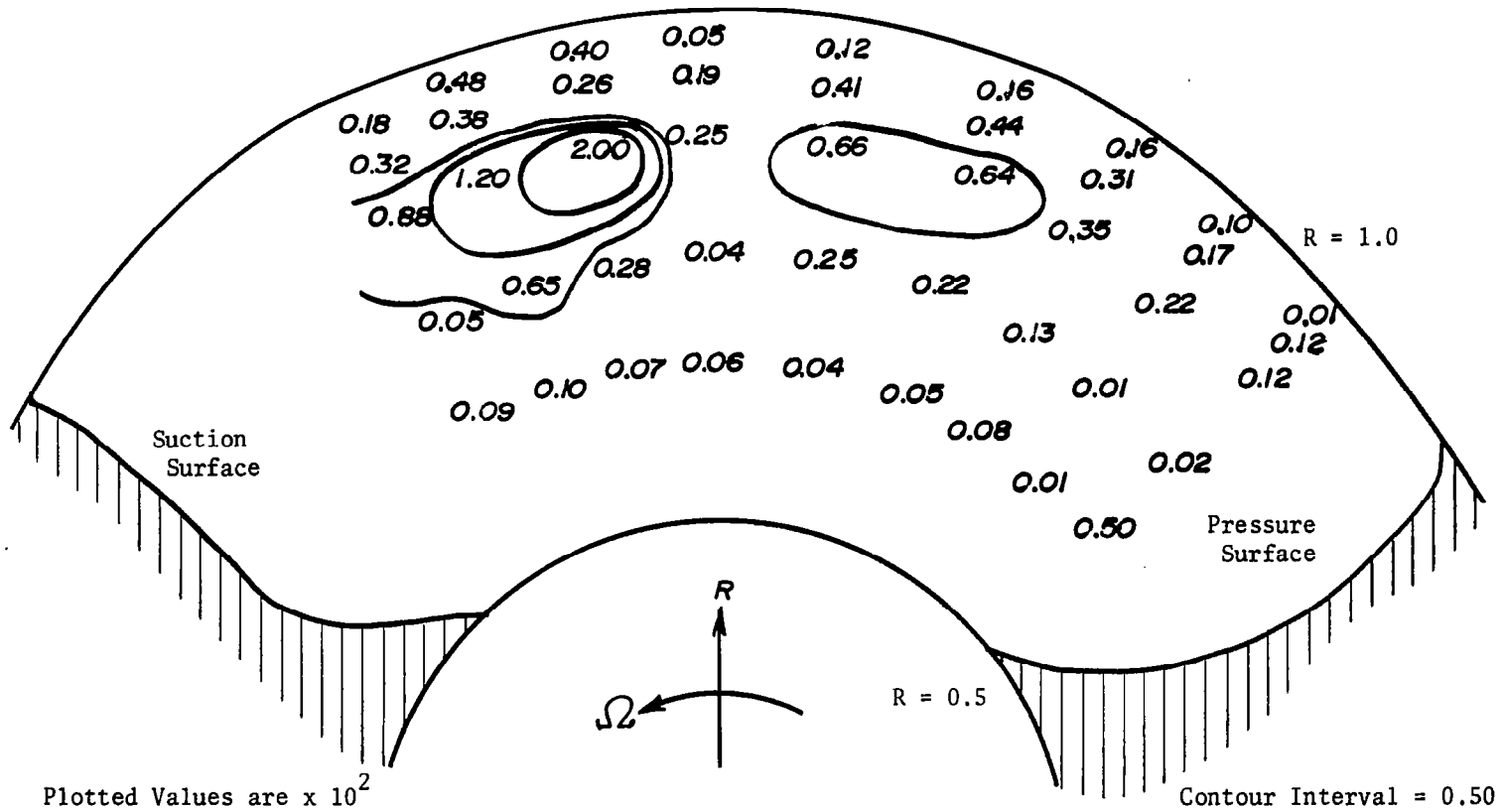
Figure 40. Turbulence Velocity Correlation $(\overline{uw}/Q_R{}^2)$ at Station 2

The distribution of turbulence stress/intensity ratios $(\overline{uv}/q^2)$, $(\overline{vw}/q^2)$ and $(\overline{uw}/q^2)$ are shown in isocontour form in Figs. 41, 42, and 43 respectively. The magnitudes of $\overline{uv}/q^2$ vary from 0.01 in isolated points to 0.32 in the high loss mixing region. The contours generally follow those of $\overline{uv}$ shown in Fig. 38, with ratios averaging approximately 0.25 applicable in the regions of higher stress. The values of $\overline{vw}/q^2$ range from 0.01 to 0.12, the higher magnitudes generally occurring in the high stress areas. The distribution of $\overline{uw}/q^2$ indicates two regions where the ratios are high, corresponding to approximately 40% and 65% passage width at R = .890. The magnitudes of $\overline{uw}/q^2$ vary from 0.01 to 0.25, the higher values limited to the two regions defined above.

## Comparison of Experimental and Theoretical Results

The Cooper-Bosch exact analysis program incorporating the modifications mentioned in the chapter entitled "Theoretical Analysis" was run for the three-bladed Penn State inducer geometry. Both inviscid and viscid cases were considered. The inviscid program was run for approximately 75 relaxation cycles, resulting in a total RMS residual of 0.077. The viscid program was run for approximately 50 cycles and produced a total RMS residual of 0.200. In this section, the results of the inviscid and viscid analyses will be discussed and compared with the experimental results described earlier in this chapter.
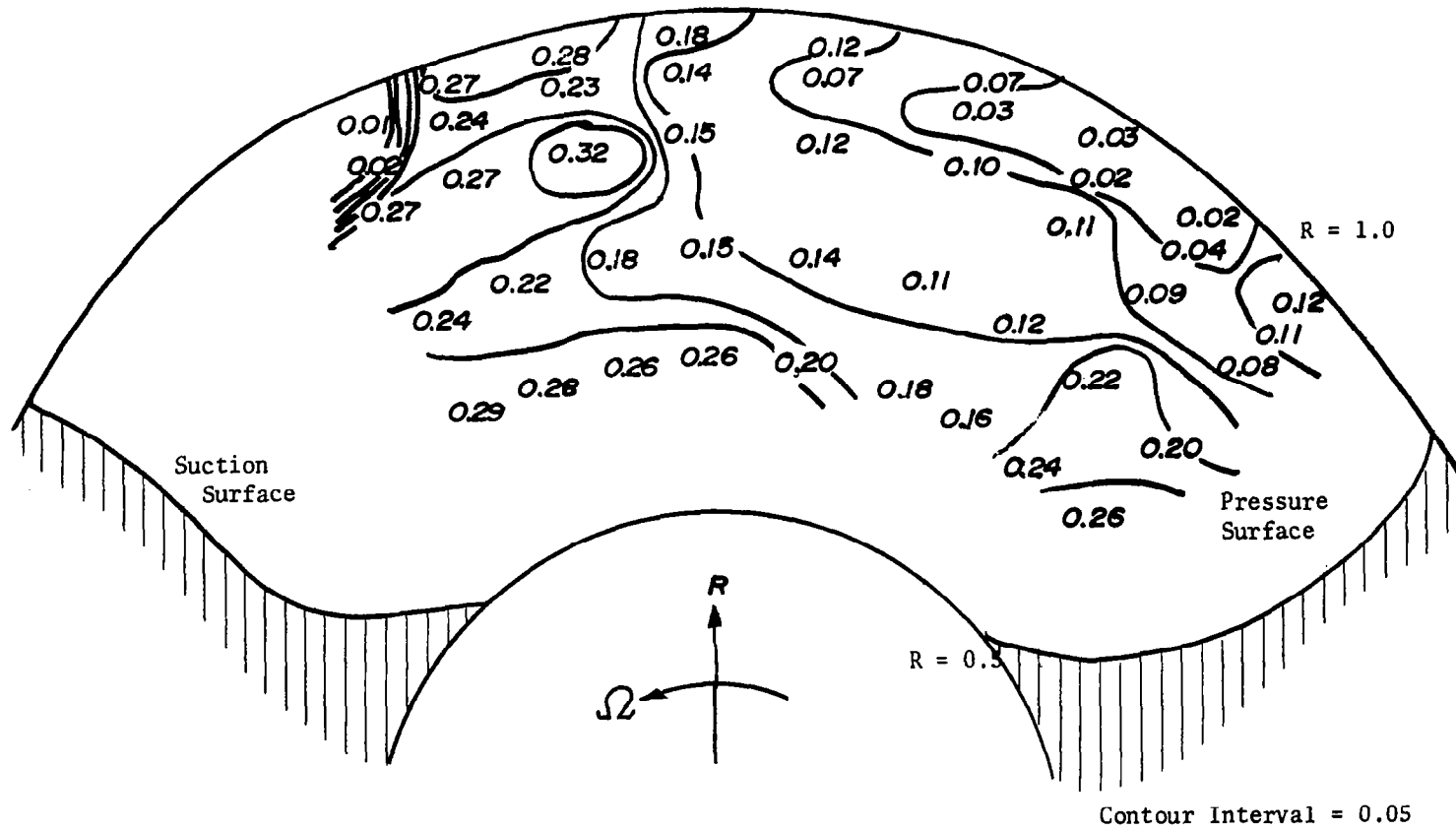
Figure 41. Turbulence Ratio ($\overline{uv}/q^2$) at Station 2
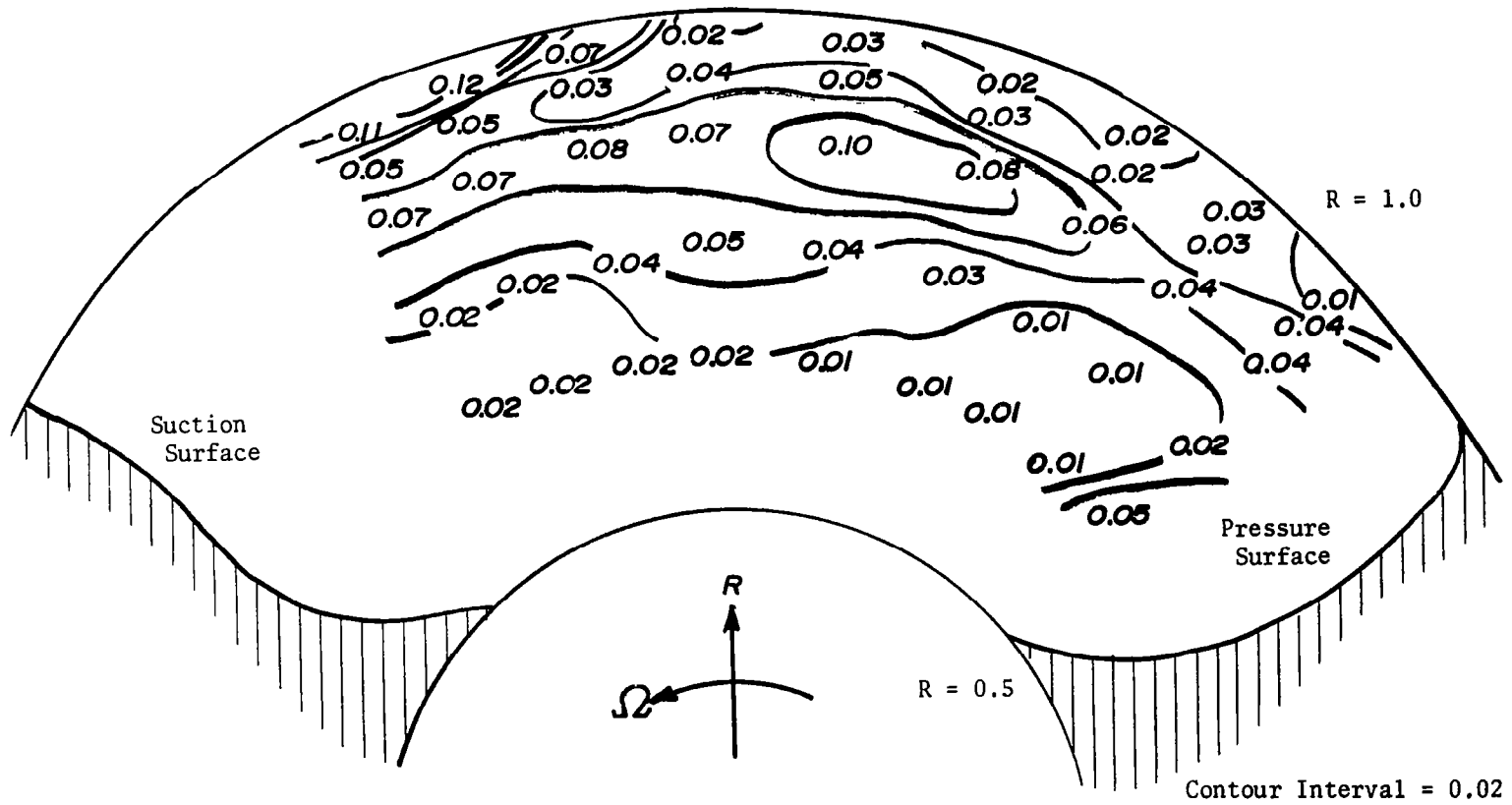
Figure 42.  Turbulence Ratio $(\overline{vw}/q^2)$ at Station 2

107
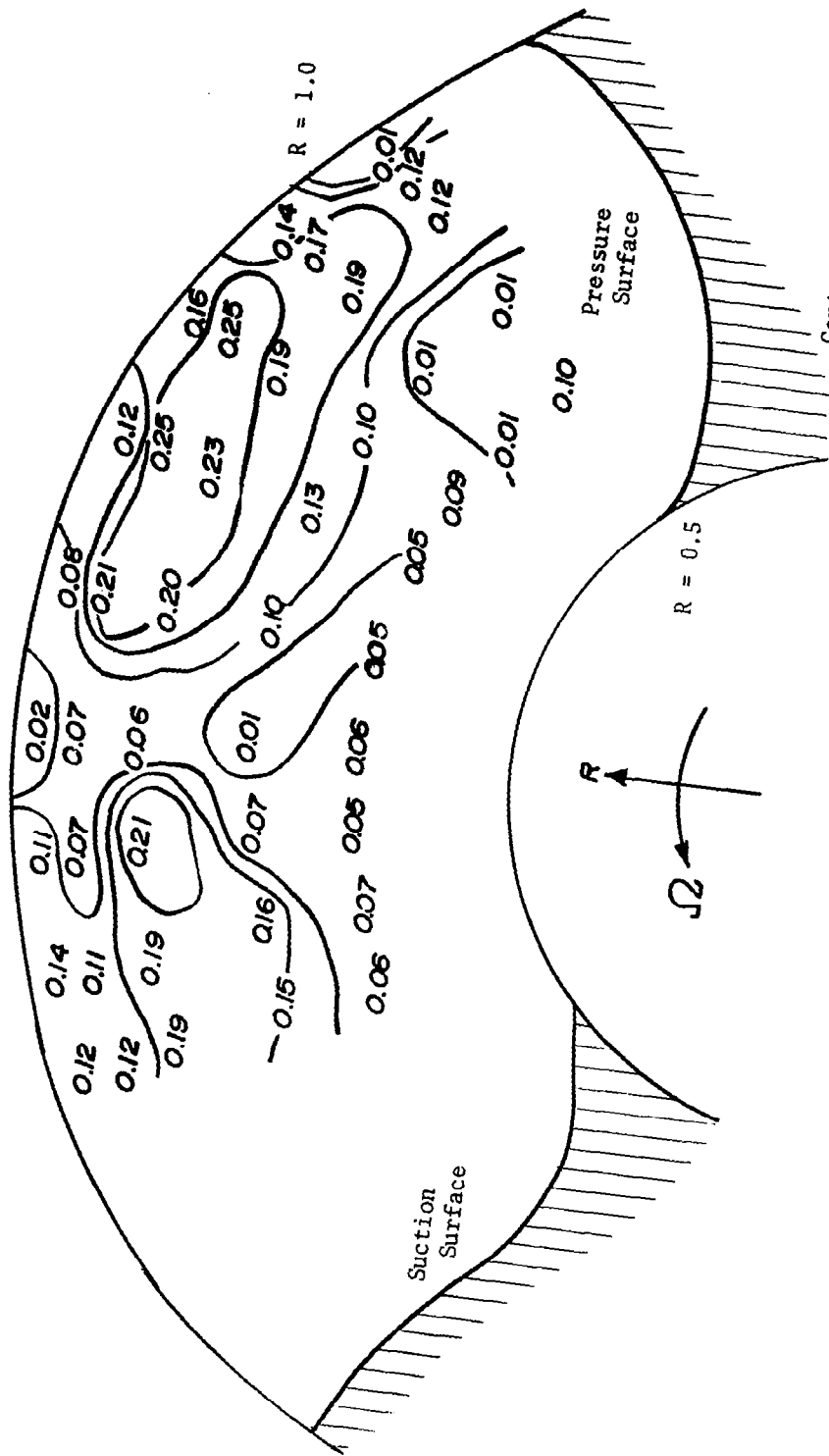


Figure 43. Turbulence Ratio ($\overline{uw}/q^2$) at Station 2

Blade Static Pressure

The inducer blade static pressure distributions derived from the exact inviscid analysis are plotted in Figs. 12-16 at the locations corresponding to the experimental $\psi_s$ measuring stations. As can be seen, the results agree remarkably well at all radial stations and especially for those near the hub (radial stations 1 and 2). Close to the hub, where three-dimensional viscid effects are not prevalent, the difference between the experimental and theoretical results should not be large. Near the tip region, the experimental pressure surface $\psi_s$ distributions agree closely with the numerical analysis while the suction surface $\psi_s$ distributions show the most discrepancy. The radial variation of $\overline{\psi_s}$ plotted in Fig. 17 shows the larger deviation between the experimental and theoretical results near the tip which is expected from previous discussions and reflects the region where the secondary flow effects are concentrated. The chordwise gradients of pressure and suction surface $\psi_s$ in Figs. 12-16 appear similar for both experimental and theoretical results.

The $\psi_s$ distributions obtained from the viscid analysis program are also plotted in Figs. 12-16. The general shape of the viscid analysis $\psi_s$ distribution closely resembles that of the inviscid analysis. Greatest variation between viscid and inviscid analyses are shown at the tip (radial station 5), where the viscous effects are dominant. The radial variations of $\overline{\psi_s}$ in Fig. 17 verify this observation. The deviation between inviscid and viscid $\overline{\psi_s}$ near the tip appears greater at station 2 than at station 1.

Mean Velocities at Station 1

Total Relative Velocity.- The inviscid analysis results for total

relative velocity $Q_R$ across the inducer passage are plotted in Fig.

44 for the radii corresponding to those used in the experimental investi-

gation. The similarity of the analytical solution with experiment can

be seen by comparing the theoretical results with Fig. 22. As in the

experimental results, the velocities increase from hub to tip. Inviscid

turning effects resulting in higher velocity near the suction surface

are also evident. Overall magnitudes of the velocities are lower than

those found from experimentation. Thus, although the static pressure

distributions have been found to be comparable, the velocities

predicted are lower than the measured values and seems to indicate loss

in kinetic energy. The radial variation of passage-averaged total

relative velocity $\overline{Q_R}$ found from the inviscid analysis is compared in

Fig. 23. The difference between the inviscid results and design

values of $\overline{Q_R}$ appears to increase from hub to tip. This tends to indi-

cate that three-dimensional inviscid effects are larger near the tip,

a result which has been shown experimentally.

The total relative velocity distribution obtained from the viscid

analysis is shown in Fig. 45. The imposition of the boundary condi-

tion which defines the relative velocity on the inducer blade surface

as zero enables the viscid program to provide a crude approximation for

the pressure and suction surface boundary layers. The magnitudes of

$Q_R$ are similar to those found from the inviscid analysis. A slight

velocity deficiency is noted near the tip at approximately 50%

passage width. This agrees with the experimental results of Fig. 22

and indicates an area of high viscous loss. A closer comparison of

110
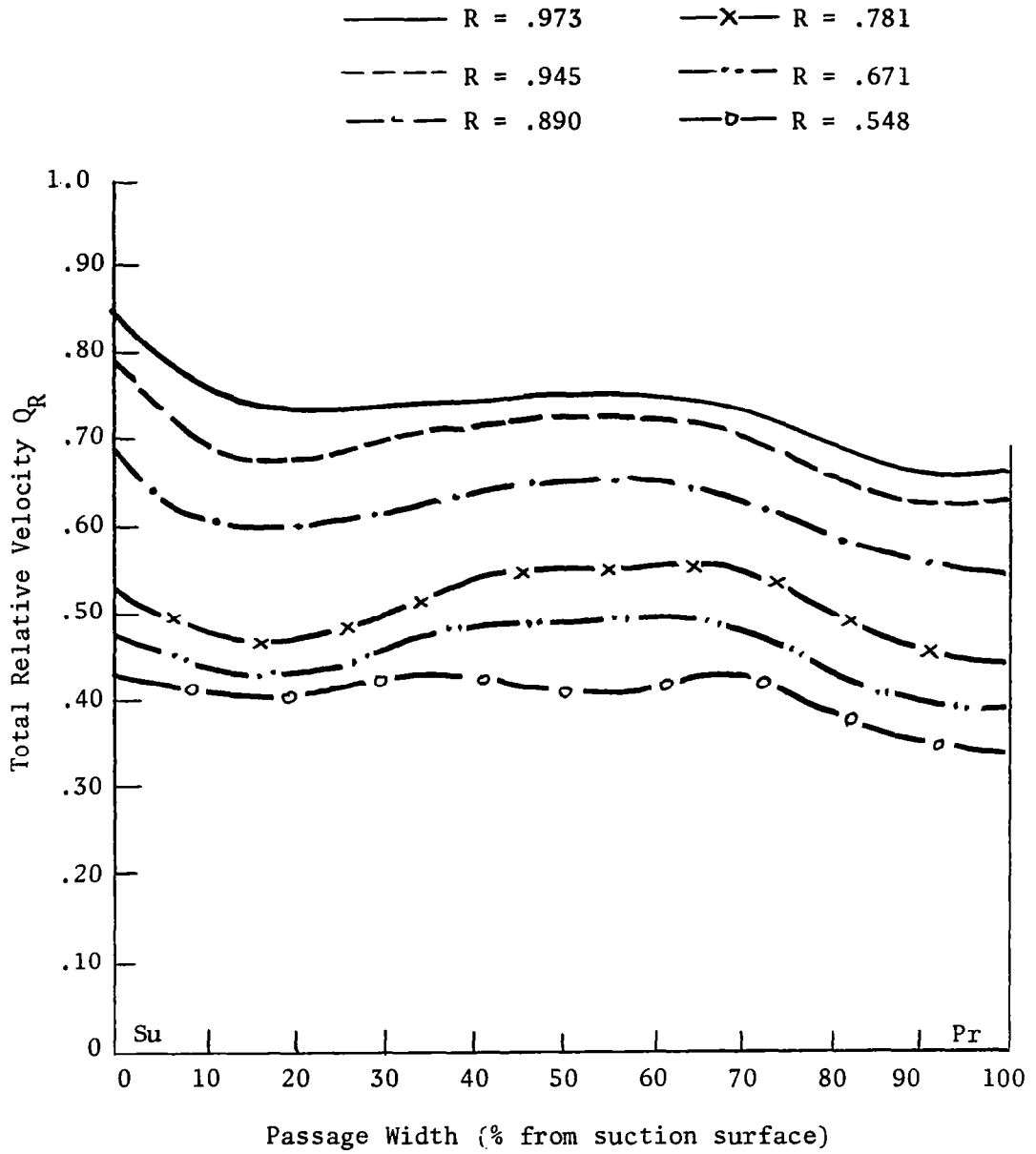


Figure 44. Inviscid Analysis Results for Total Relative Velocity
Distribution at Station 1
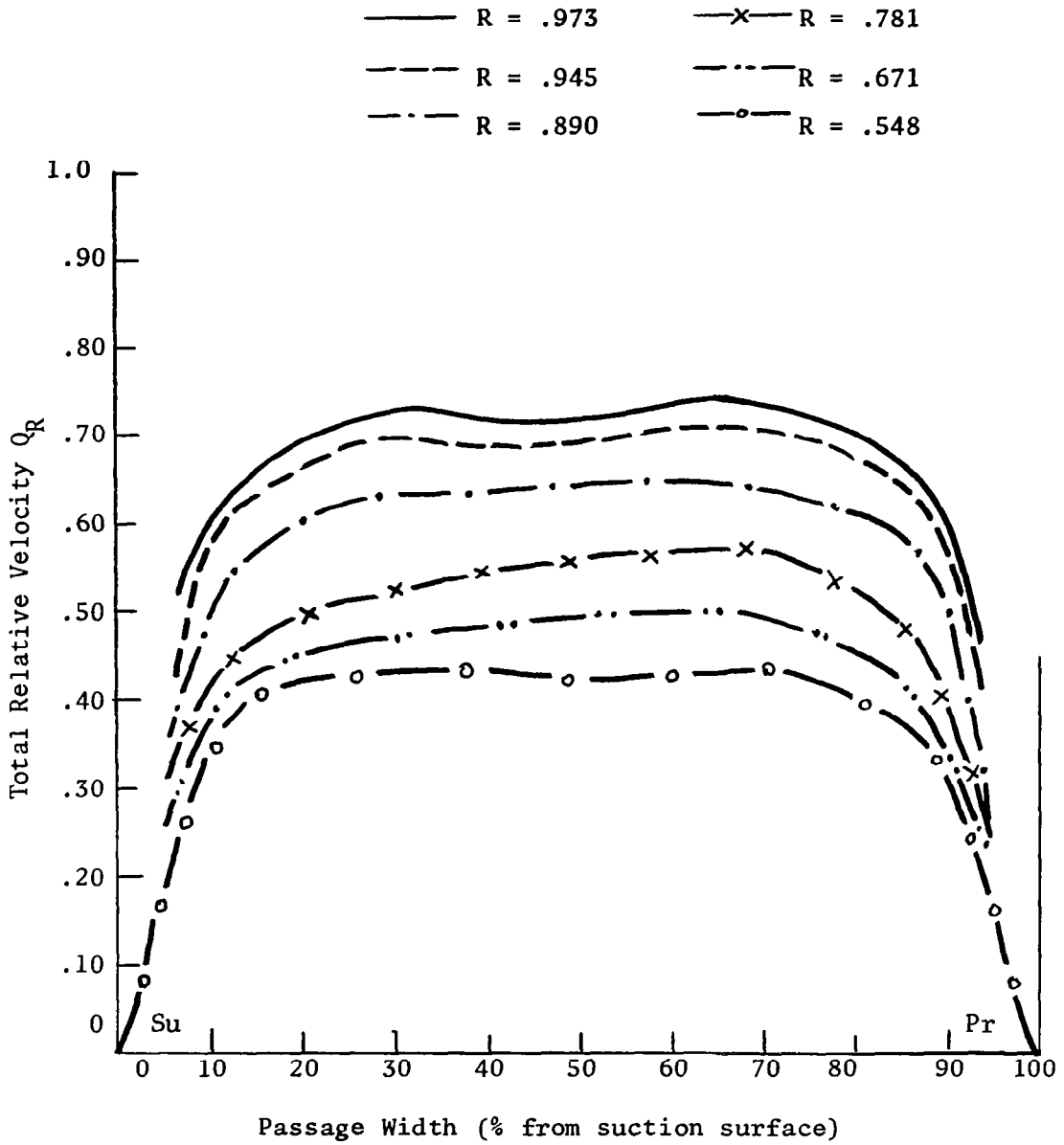
Figure 45. Viscid Analysis Results for Total Relative Velocity
Distribution at Station 1

results can be made by examining Fig. 46 for R = .973 and Fig. 47 for R = .548. The viscid results seem to agree with experiment qualitatively. The radial variation of $\overline{Q_R}$ in Fig. 23 shows that, near the tip, the viscid analysis velocities are lower than those derived from the inviscid analysis.

Relative Tangential Velocity.- The relative tangential velocity distributions obtained from the inviscid and viscid analyses are not included here, since the magnitude and shape of these curves closely approximate the total relative velocity distributions of Figs. 44 and 45 and illustrates the dominance of the tangential component inside the inducer channel.

Axial Velocity.- The axial velocities predicted from viscid and inviscid analysis at R = .973 and R = .548 are shown compared with experimental results in Fig. 48. The predictions were found to be very similar at all radii. The predictions are good at R = .548 and poor at R = .973, thus indicating the dominance of viscous effects near the tip. No comments can be made with regard to the accuracy of viscid results, since the measurements close to the proximity of the wall are not available. The passage-averaged velocities $\overline{W}$ are compared with experimental results in Fig. 27. The predictions are good up to R = .9, the discrepancy increases considerably beyond this radius.

Radial Velocity.- The radial velocity predicted from the theoretical analyses is found to be very small at this station. The radial variation of passage-averaged radial velocity $\overline{U}$, plotted in Fig. 29, indicates that the theoretical predictions are significantly lower than

113
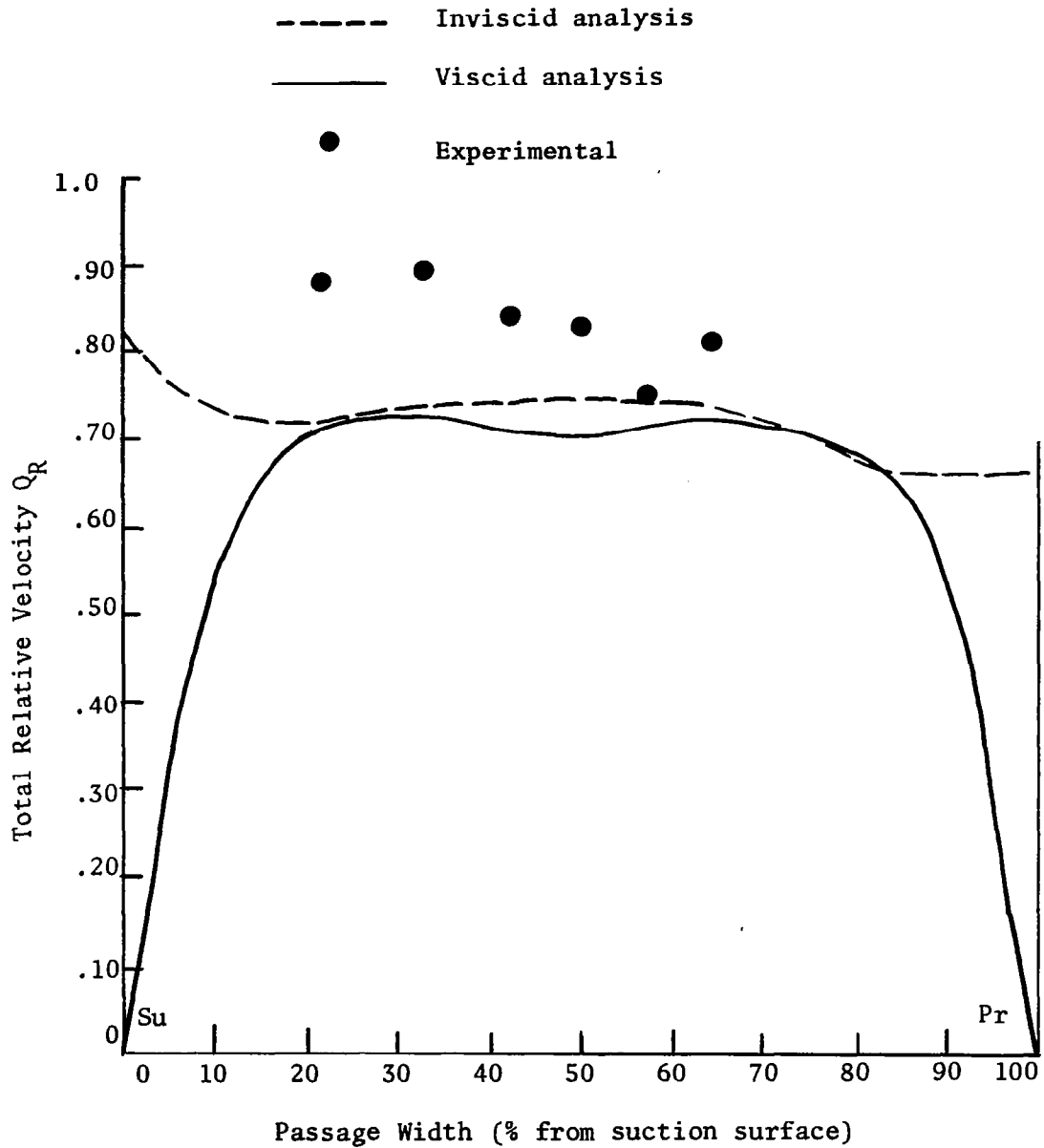


Figure 46.  Comparison of Total Relative Velocity
Distributions at Station 1, R = .973

114
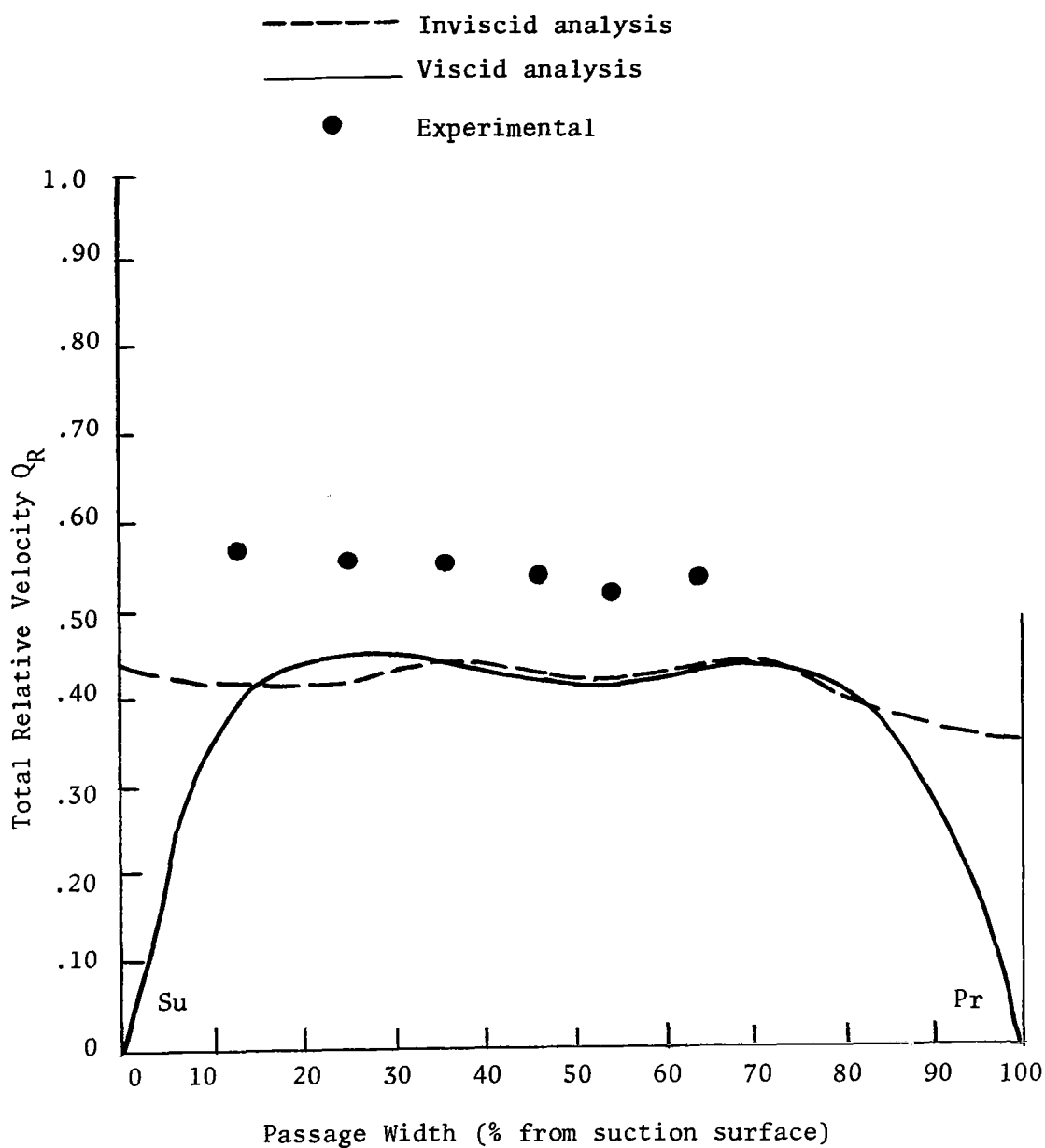


Figure 47. Comparison of Total Relative Velocity
Distributions at Station 1, R = .548
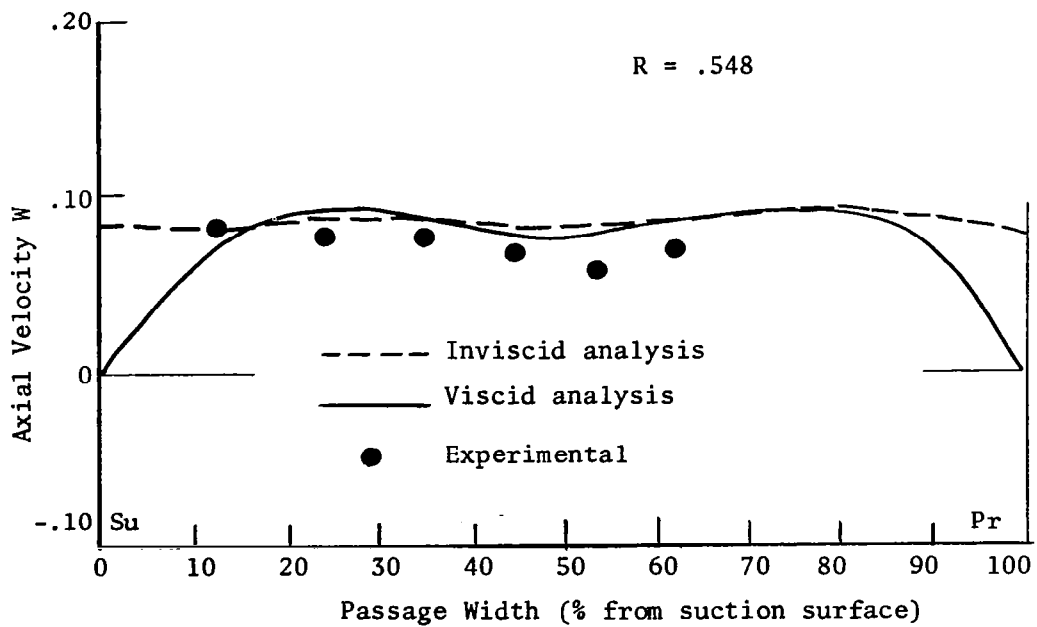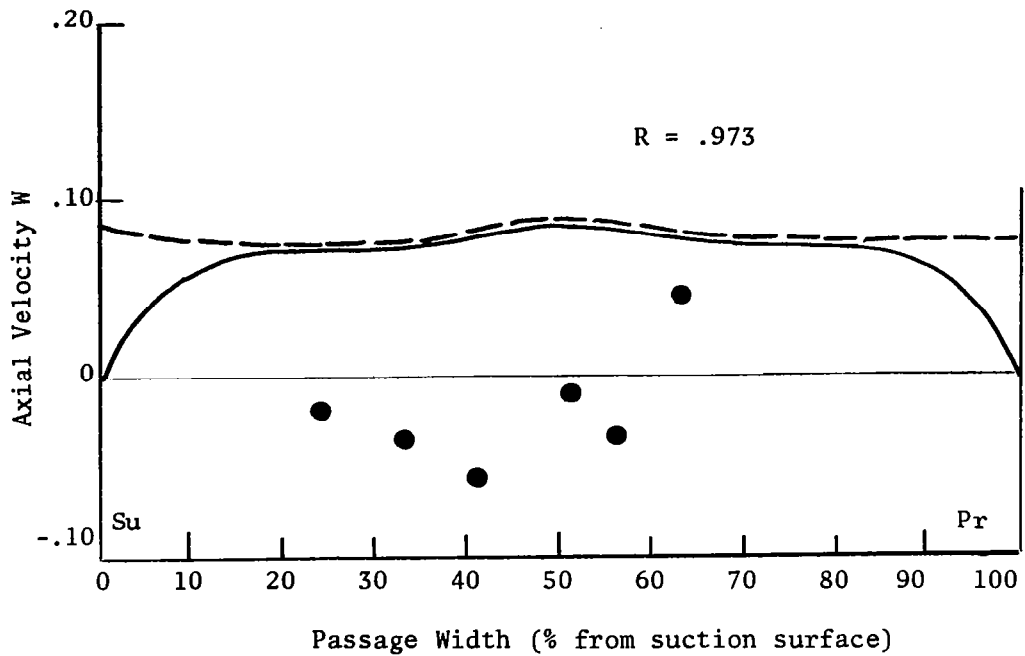
Figure 48.  Comparison of Axial Velocity Distributions
at Station 1, R = .973 and R = .548

116

the experimental results and emphasizing the substantial three-
dimensionality which exists in the real inducer flow.


Mean Velocities at Station 2

Total Relative Velocity.- Inviscid analysis results for the total
relative velocity distribution are plotted in Fig. 49. Magnitudes of
$Q_R$ near the tip are comparable to those found experimentally (Fig. 30a),
whereas near the hub the inviscid velocities are significantly lower
than those shown for the experimental results of Fig. 30a. The latter
observation is consistent with the results for the $Q_R$ distribution at
station 1. The radial variation of passage-averaged total relative
velocity predicted from the inviscid analysis is shown in Fig. 31. The
difference between the inviscid results and design values of $\overline{Q_R}$ appears
to increase from hub to tip, indicating the larger three-dimensional
inviscid effects existing near the tip and confirmed by experimentation.
Comparison of inviscid results from Fig. 31 with those of Fig. 23 for
station 1 indicates that the deviation between the inviscid and design
velocities has increased from station 1 to station 2. This supports
the contention that the three-dimensional inviscid effects increase in
severity as the flow proceeds downstream inside the inducer channel.
The agreement between the measured and predicted $\overline{Q_R}$ is reasonably good
(Fig. 31).

The viscid analysis prediction for the total relative velocity
distribution is shown in Fig. 50. It is a striking departure from the
inviscid analysis distribution (Fig. 49), especially near the tip
where the viscous effects are known to be appreciable. The viscid
analysis also provides crude approximations for the suction and pressure
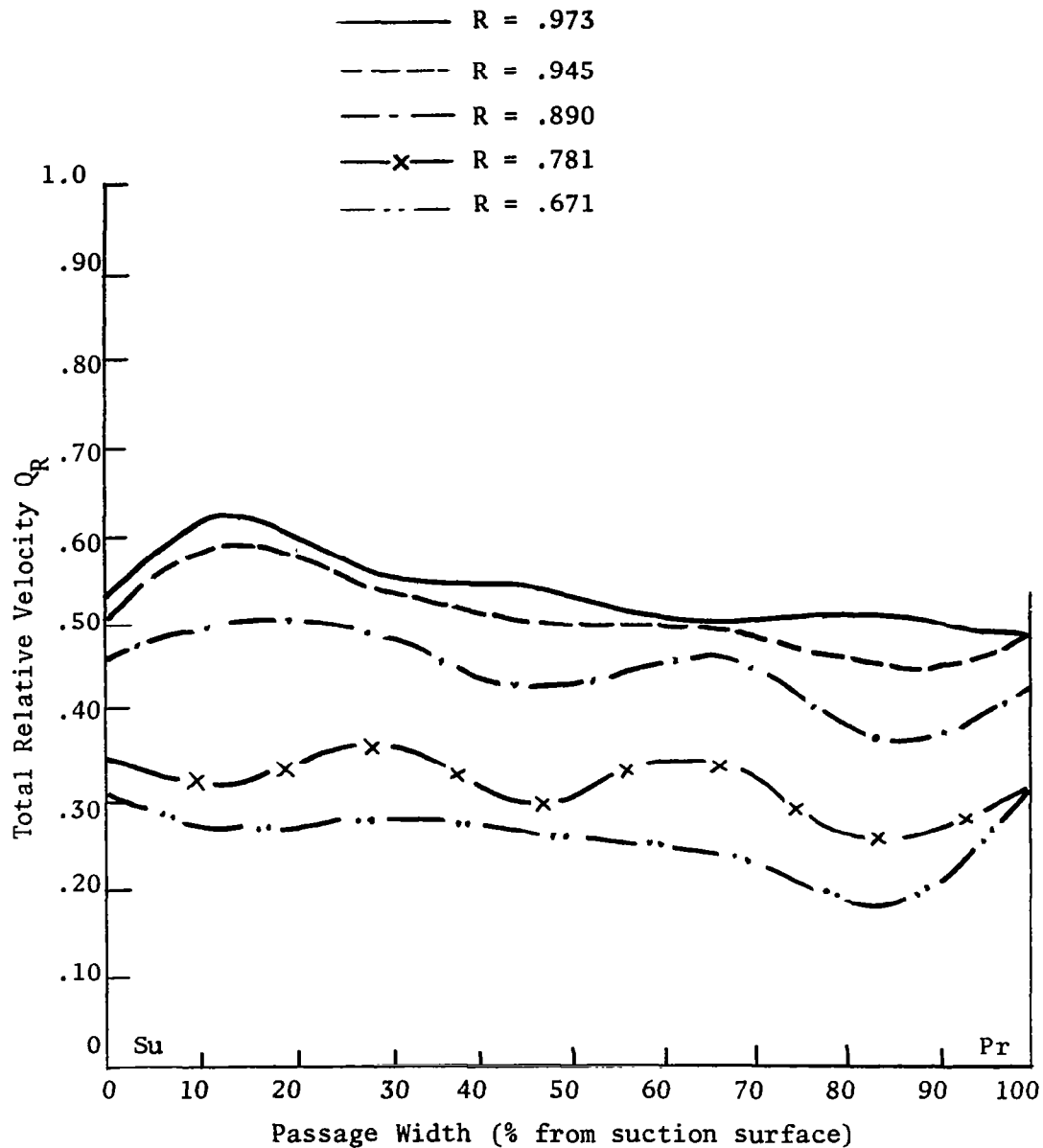
Figure 49.  Inviscid Analysis Results for Total Relative
Velocity Distribution at Station 2

118
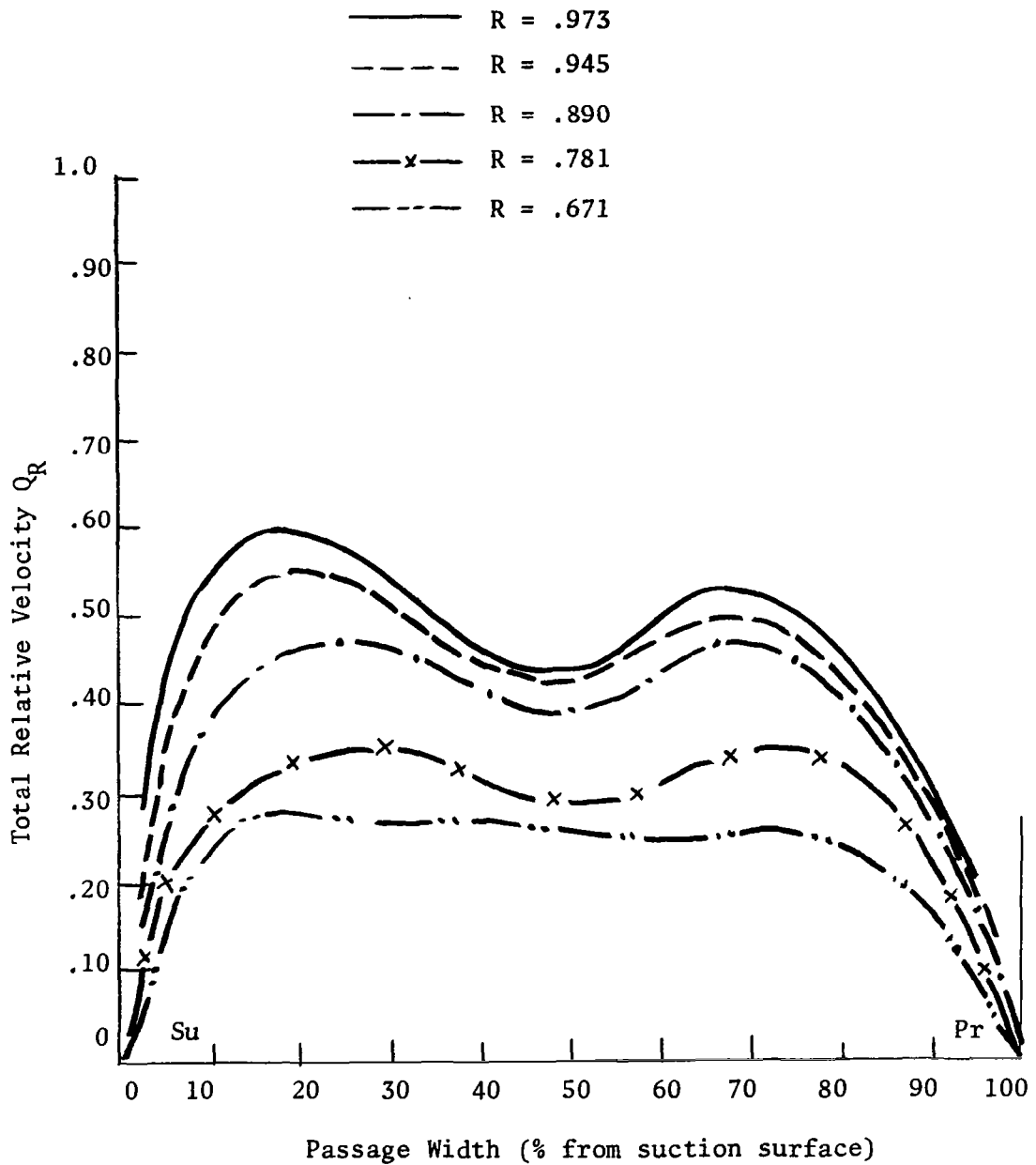


Figure 50.  Viscid Analysis Results for Total Relative Velocity
Distribution at Station 2

surface boundary layers. A large velocity deficiency near the tip is predicted at approximately 50% passage width and agrees favorably with the experimental $Q_R$ profiles plotted in Fig. 30a. It is apparent that the velocity deficiency noted near the tip at station 1 (Fig. 45) has grown considerably as the flow proceeded downstream to station 2, indicating an increase in size and intensity of the viscous loss region and substantiating the experimental results discussed previously. The blade boundary layer development predicted by the viscid analysis can be seen in Fig. 50. The suction surface boundary layer appears thicker than the pressure surface boundary layer at all radii, increasing in thickness from hub to tip. This observation is consistent with experimental results and conforms with previous discussions on boundary layer interaction and flow mixing near the tip. The radial variation of $\overline{Q_R}$ derived from the viscid analysis is plotted in Fig. 31. The deviation between viscid and inviscid velocities near the tip can be attributed to the large viscous losses which are known to exist in this region. Comparisons of the total relative velocity distributions at R = .973 and R = .548 are given in Fig. 51 and Fig. 52 respectively. It appears that the viscid analysis distribution provides better approximations to the experimentally derived velocity profiles.

Relative Tangential Velocity.- Relative tangential velocity distributions predicted by the inviscid and viscid analyses closely resemble the total relative velocity distributions indicated in Fig. 49 and 50 respectively. Comments in the previous section relating to total relative velocity are also applicable here. The tangential velocity continues to dominate the flow within the rotating inducer passage,

120
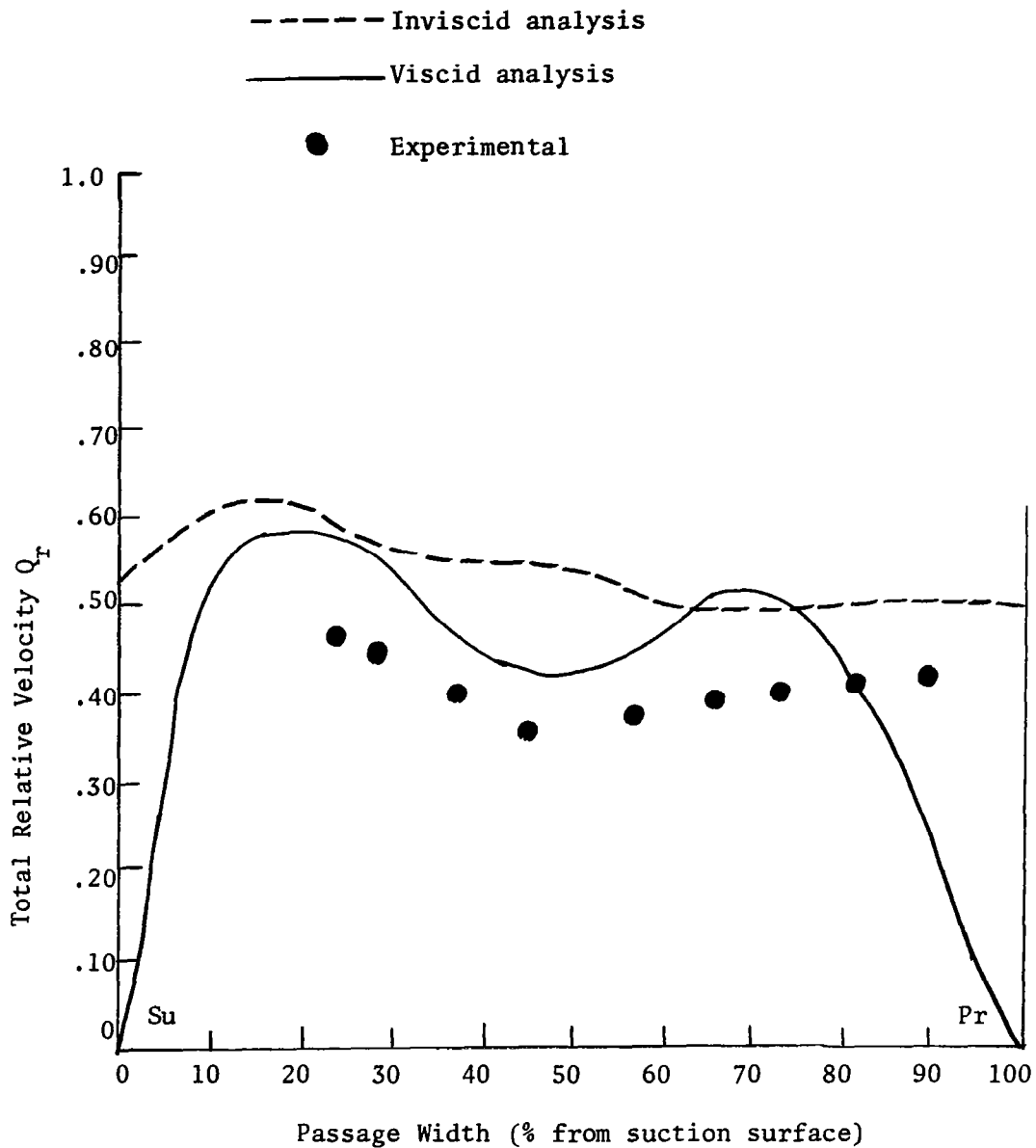


Figure 51. Comparison of Total Relative Velocity Distributions
at Station 2, R = .973
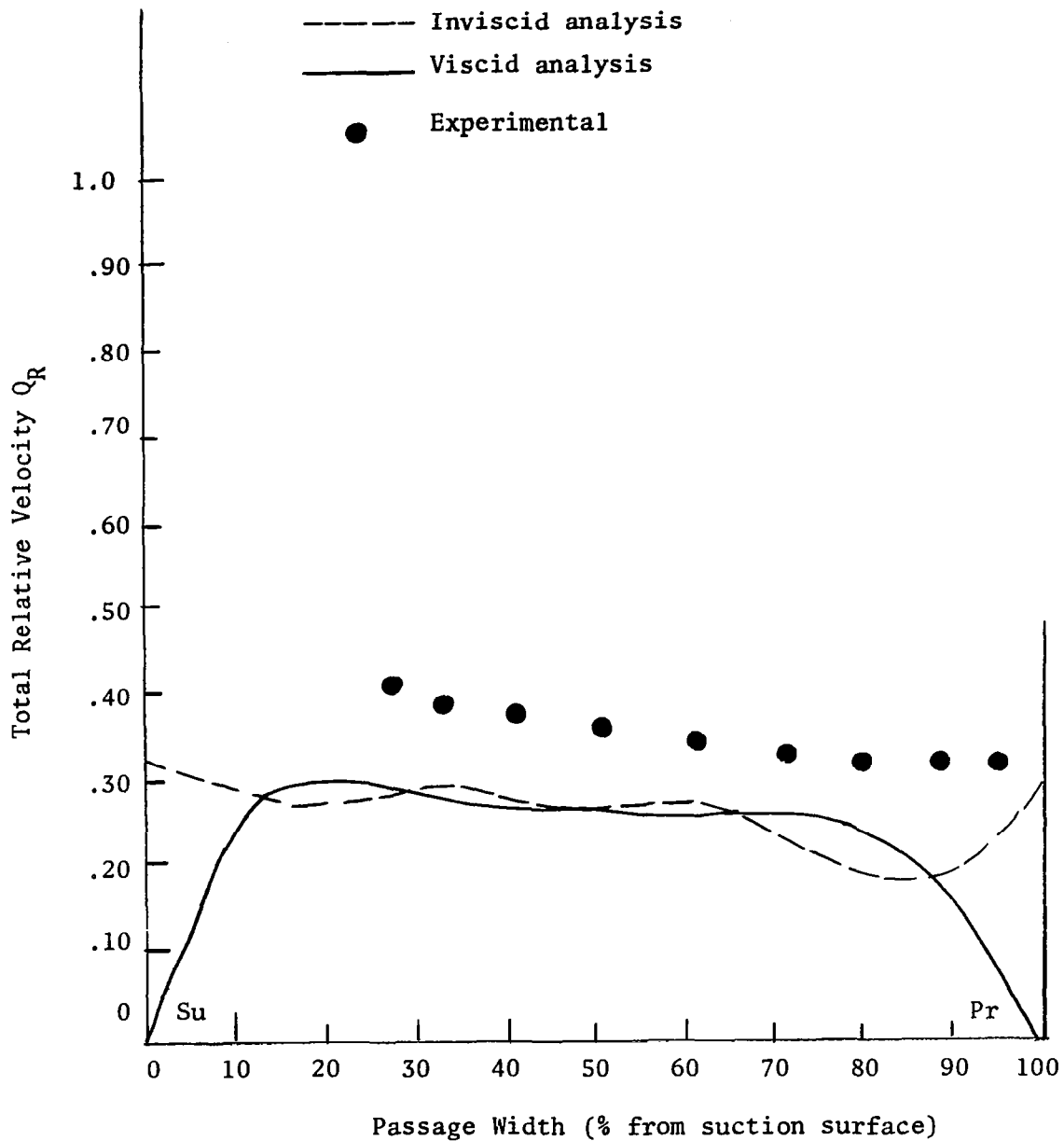
Figure 52. Comparison of Total Relative Velocity
Distributions at Station 2, R = .671

although the influence of radial and axial velocities is greater than
that at station 1, especially near the hub. The three-dimensionality
of the flow is appreciable. The radial variation of passage-averaged
relative tangential velocity derived from the inviscid analysis is
shown in Fig. 33. The influence of three-dimensional inviscid
effects on the flow, reflected in the difference between inviscid
results and design, appears to increase in magnitude near the tip. The
high absolute tangential velocities predicted from the inviscid
analysis are indicative of the high stagnation pressure rise through
the inducer passage. The lower values of viscid analysis $\overline{V}$, when
compared to those predicted from the inviscid analysis (Fig. 33), can
be attributed to the viscous losses and secondary flows which prevail
at this location. The higher values of absolute tangential velocity
predicted from the viscid analysis are consistent with the increased
effects of complex viscous interactions near the tip.

Axial Velocity.- Fig. 53 shows the axial velocity distribution
predicted from the inviscid analysis. There is a definite decrease in
axial velocity from hub to tip, which appears to indicate the presence
of the blade blockage effect within the flow passage. This observation
is consistent with the experimental results plotted in Fig. 30b. The
radial variation of $\overline{W}$ predicted from the inviscid analysis (Fig. 27)
agrees almost exactly with the experimental distributions. Continuity
has been satisfied within the exact analysis program.

The viscid analysis results for the axial velocity distributions
are shown in Fig. 54 and indicate the approximate profiles for the
pressure and suction surface boundary layers. The axial velocity
profile decreases in magnitude from hub to tip and tends to confirm
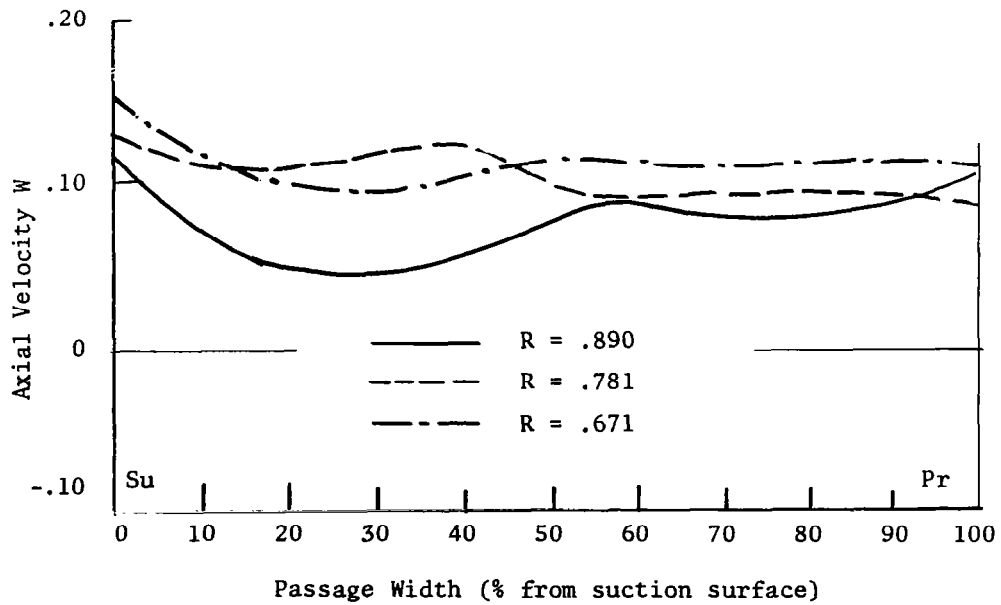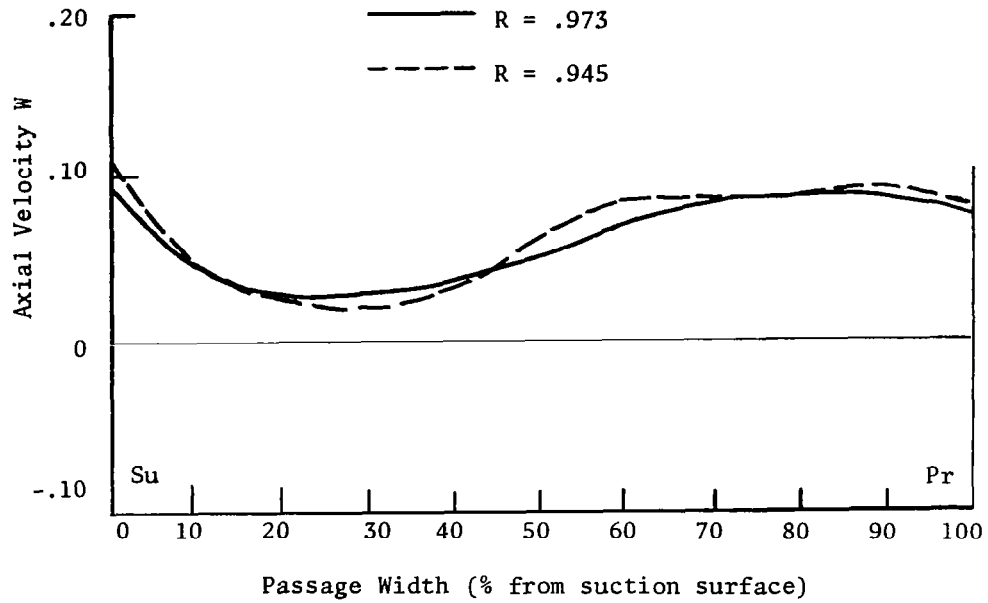
Figure 53.   Inviscid Analysis Results for Axial Velocity
Distribution at Station 2
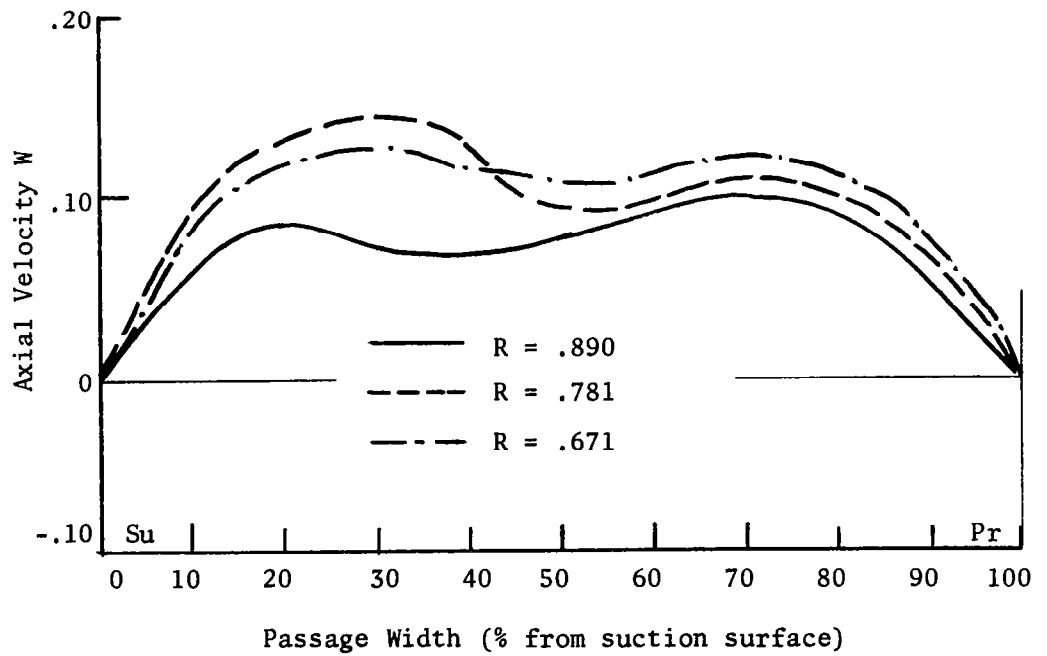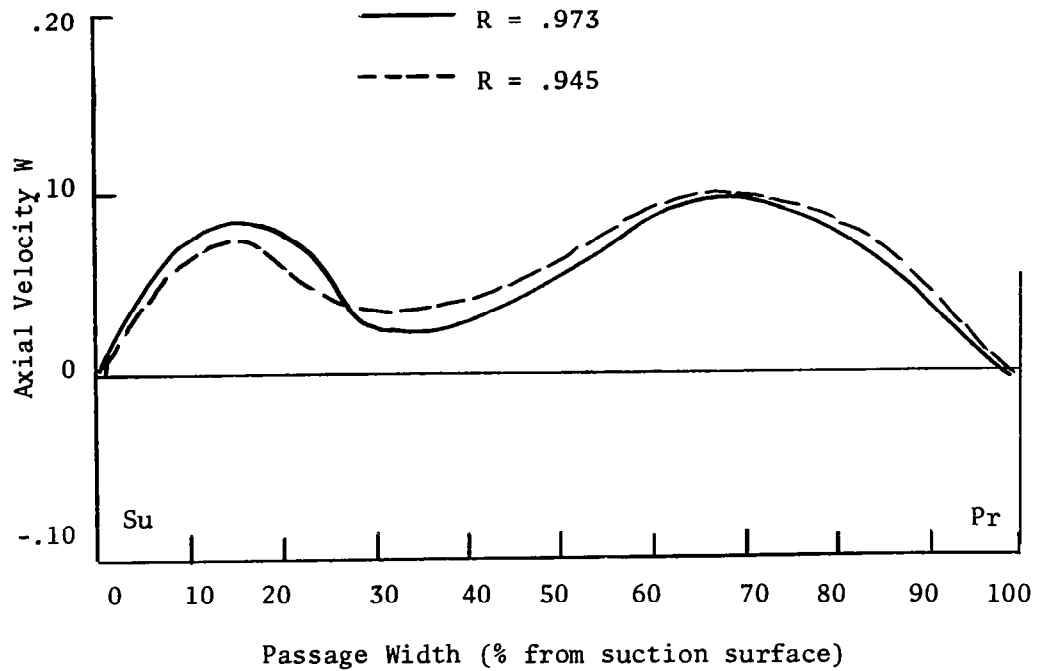
Figure 54. Viscid Analysis Results for Axial Velocity Distribution
at Station 2

the presence of the blade blockage effect at this location. The radial

variation of viscid analysis $\overline{W}$ in Fig. 27b conforms almost precisely

with the experimental results. Comparisons of the axial velocity

distributions at R = .973 and R = .671 are given in Fig. 55. The

axial velocity profiles predicted from the viscid analysis appear to

more closely approximate the experimental distributions.

Radial Velocity.- The inviscid analysis results for the radial

velocity distribution at station 2 are given in Fig. 56. The tip

region appears to exhibit the lowest radial velocities, which is

consistent with the experimental results plotted in Fig. 32b. The

blade limiting streamline angle measurements also substantiate this

observation. The magnitudes of the inviscid analysis radial velocities

are significantly lower than the corresponding values of experimental

radial velocity, indicating the considerable three-dimensionality of

the real flow existing within the inducer blade passages. The radial

velocity plotted in Fig. 56   appears to decrease across the inducer

passage from suction surface to pressure surface, a condition which is

found to exist experimentally (Fig. 32b). A region of radially

inward flow near the tip at approximately 50% passage width is noted

from the inviscid analysis radial velocity profiles. The existence

of radially inward flow in this area has been found experimentally and

is consistent with previous discussions on flow mixing effects in this

region.

The viscid analysis results for the radial velocity distribution is

shown in  Fig. 57.  Little difference is noted from the inviscid

distribution except at the pressure and suction surfaces where the

velocities are fixed at zero. The region of radially inward flow near
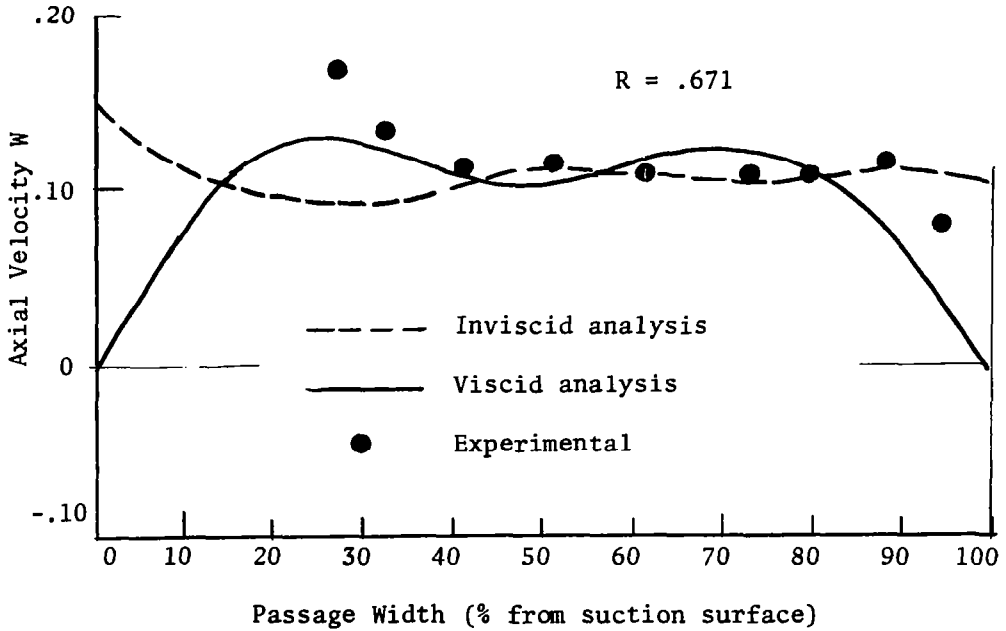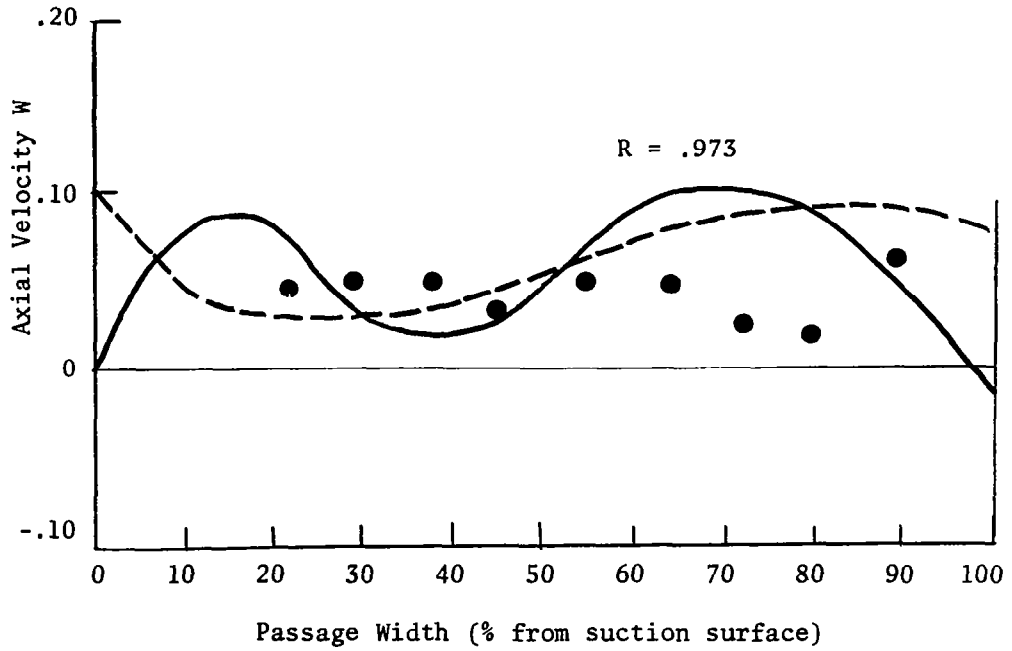
Figure 55.  Comparison of Axial Velocity Distributions at
Station 2, R = .973 and R = .671
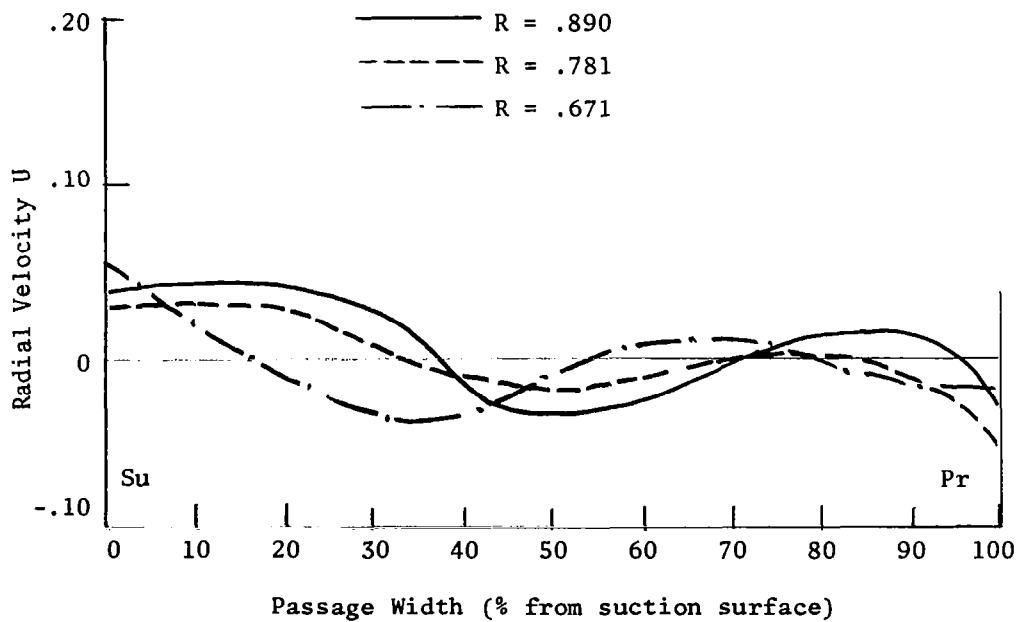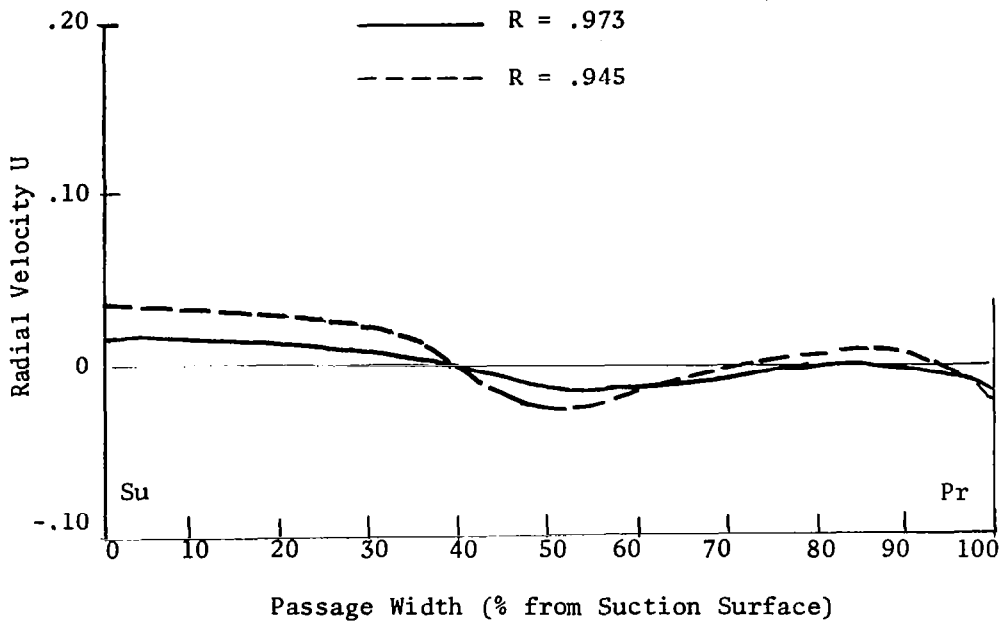
Figure 56. Inviscid Analysis Results for Radial Velocity
Distribution at Station 2
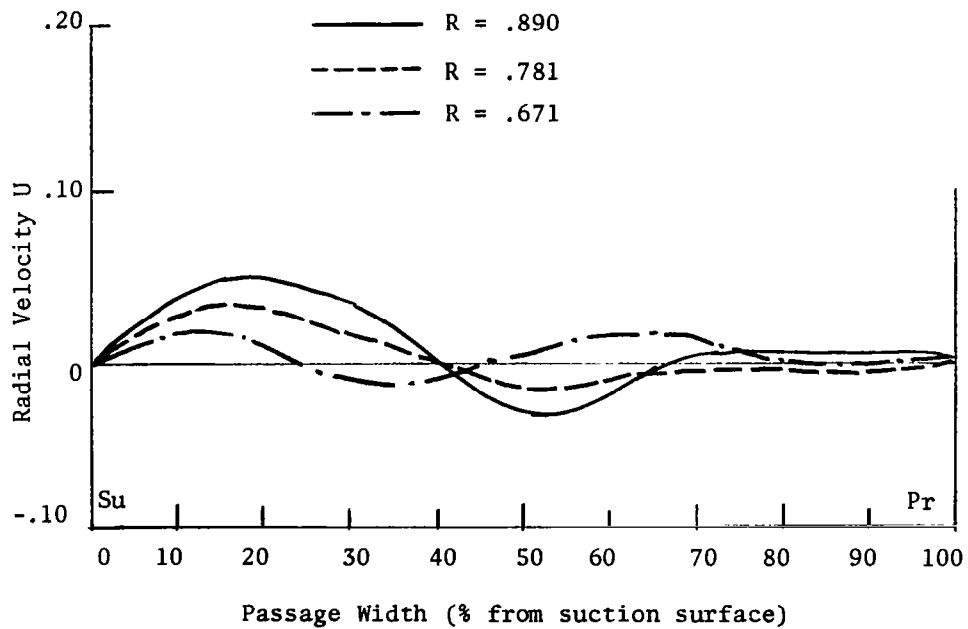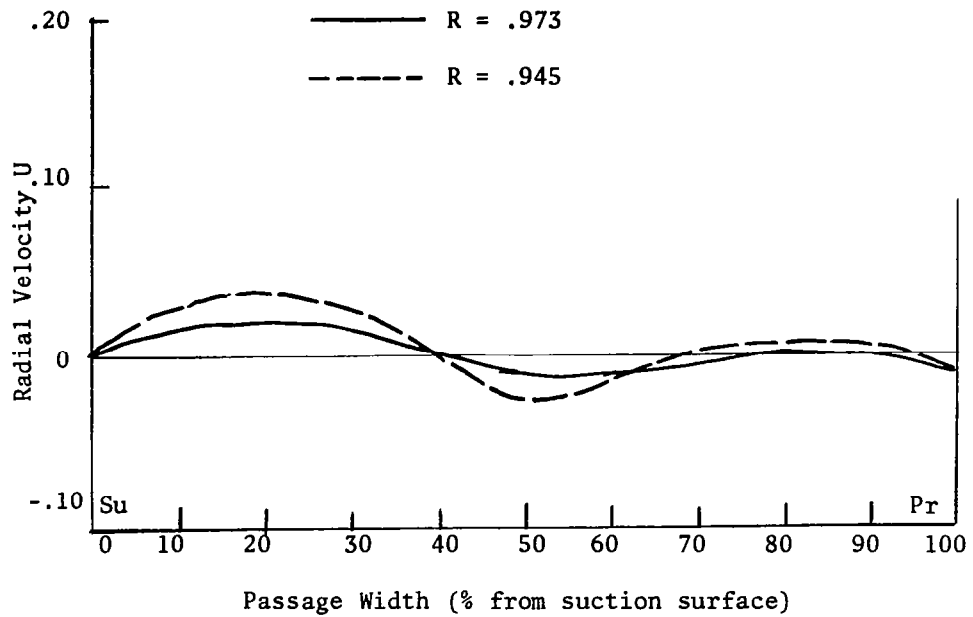
Figure 57.   Viscid Analysis Results for Radial Velocity
Distribution at Station 2

the tip is similar to that found with the inviscid analysis. The radial variation of passage-averaged radial velocity derived from the viscid analysis (Fig. 29) reflects the significantly higher radial velocities found experimentally.

130

## DISCUSSIONS AND CONCLUSIONS

A brief summary of conclusions reached by the analytical and experimental investigation reported in this thesis are as follows:

1) Preliminary investigations into the use of the quasi-three-dimensional Douglas-Neumann method indicate that it appears to provide a better initialization of velocity and pressure parameters needed for the Cooper-Bosch exact solution.

2) Modifications to the Cooper-Bosch program to automatically unload the trailing edge station and incorporate dominant viscid effects have been made in subroutines "Main", "Dloss", and "Resid". Preliminary testing of these modifications indicate that the inviscid analysis has been improved and a satisfactory viscous capability has been provided.

3) The viscid analysis is, at best, approximate due to the various assumptions and simplifications made. In particular, the viscid boundary conditions imposed on the solution are rather drastic, since the grid geometry spacing used in the exact analysis is relatively large. More tangential grid stations would be needed, especially close to the blade surface, to better define the shape of the blade boundary layer.

4) The ammonia trace technique provides a satisfactory method for determining blade limiting streamline angles within the rotating inducer blade passages. The blade limiting streamline angle measurements provide several observations which have either been noted in previous investigations or have been found from other experimental results contained in this thesis. These include: an increase in $\alpha$ from the leading edge to the trailing edge indicating the existence of higher radial velocities as the flow proceeds downstream within the

inducer channel; higher values of $\alpha$ near the hub indicating higher radial velocities in this region; negative values of $\alpha$ at the pressure surface tip (up to 45% chord) indicating radially inward flow due to the presence of the annulus wall boundary layer scraping effect; values of $\alpha$ greater than $90^\circ$ near the hub trailing edge indicating the existence of a backflow region in this area; higher values of $\alpha$ throughout the inducer channel in comparison with the results of a single blade reported in Ref. 14 and indicating appreciable radial velocities existing within the inducer passage, especially near the blade surface. In addition, the blade limiting streamline measurements will provide valuable information on boundary layer and Reynolds stress characteristics for future investigations.

5) The experimental blade static pressure distributions confirm the trailing edge loading characteristic inherent in the inducer blade design. The magnitudes of $\psi_s$ are considerably higher than design values, indicating the significant effect of three-dimensionality in the inducer flow. The static pressure distributions display small negative $\psi_s$ values near the leading edge of the suction surface. The agreement between theory and experiment is good, especially near the hub where flow mixing and viscous loss effects are minimal.

6) The rotating triaxial hotwire probe utilized in this study has yielded satisfactory velocity profiles and turbulence quantities. Comparison of velocities derived from this method show good agreement with those found from rotating pressure probe measurements in Ref. 7. It can be concluded that hotwire anemometry can be an extremely useful tool in the study of the relative flow parameters in a rotating environment.

7) Total relative velocity measurements indicate a substantial velocity deficiency near the tip at mid-passage which expands significantly as the flow proceeds downstream toward the inducer trailing edge. This indicates the considerable extent of flow mixing due to boundary layer interaction, radially inward and outward flow, annulus wall effect, etc. which is prevalent at this location inside the long narrow passages of the inducer. The position of this "loss core" appears to drift closer to the blade suction surface as the flow proceeds toward the inducer exit. An increased difference between the experimental results and the two-dimensional design curves near the tip for the radial distribution of passage-averaged total relative velocity further indicates the regions where significant three-dimensional effects and flow losses exist. The velocity distributions determined from the theoretical analysis are similar to those derived from experimentation. The presence of the velocity deficiencies near the tip has been predicted by the viscid analysis program.

8) The high values of absolute tangential velocity which are found to exist near the inducer tip indicate a region of large absolute stagnation pressure rise caused by the effects of complex viscous interactions. The size and severity of this region increases significantly as the flow proceeds downstream inside the inducer blade channel. This observation is also predicted from the three-dimensional theoretical analysis.

9) The higher values of axial velocity near the hub indicate the significant effect of blade blockage within the inducer flow passage. A slight backflow was found to exist at the extreme tip location of flow station 1 and can be attributed to the annulus wall

boundary layer scraping effect identified in the $\varepsilon_w$ measurements. The agreement between the experimental results and theoretical analysis is extremely good. The viscid analysis results appear to more closely approximate the experimental axial velocity distributions than the inviscid program.

10) The measured magnitudes of radial velocity are found to be on the same order as those of axial velocity within the inducer passage. This is similar to the results of Ref. 20 which were made slightly downstream of the inducer trailing edge. The large values of radial velocity confirm the highly three-dimensional characteristic of inducer flow and emphasize the necessity of a suitable three-dimensional theory for accurate flow analysis. The radial velocities are generally found to decrease in magnitude from hub to tip and increase in magnitude from leading edge to trailing edge. These observations are consistent with the $\varepsilon_w$ measurements mentioned previously. A region of radially inward flow is found to exist near the mid-passages of the tip region and correspond to the locations of the velocity deficiencies noted in the $Q_R$ distributions. These measurements support the explanation for the existence of the large flow losses in this region due to extensive flow mixing and complex viscous interations. The magnitudes of radial velocity predicted from the theoretical analysis are significantly lower than the experimental results. The radially inward flow found experimentally near the tip mid-passage has been predicted with the three-dimensional theoretical analysis.

11) Turbulence levels within the blade passage, indicated from the experimental results of this thesis, are generally high near the tip regions. A growing core of high turbulence is evident near the tip

134

mid-passage corresponding to the region of velocity deficiency

mentioned in item 7) above. High turbulence levels are also recorded

near the hub pressure surface and indicate the influence of the pres-

sure surface boundary layer. The radial component of turbulence

intensities appears to have the largest magnitudes, reaching calculated

values of up to 24% in the mixing region. The total turbulence energy

contours are similar to those of the turbulence intensities.

12) The locations of high turbulence stresses are concentrated in

the high turbulence intensity areas of the mixing region and near the

hub pressure surface. Values of $\overline{uv}$ appear to be higher in the mixing

region than the corresponding values of $\overline{vw}$ and $\overline{uw}$. The high stress

regions are indications of areas subjected to complex viscous inter-

actions.

13) Experimental velocity and turbulence results of Ref. 20

show nearly uniform distributions slightly downstream of the inducer

trailing edge. Thus it appears that considerable wake diffusion occurs

immediately after the trailing edge to decay the turbulence core and

blade blockage effects reported in this thesis.

The hotwire analysis developed in this investigation was an

initial attempt to determine the three components of velocity,

turbulence intensity and Reynolds stresses in a rotating reference

frame. Certain improvements and refinements can be made to the

experimental techniques to reduce the errors encountered in the experi-

mental measurement. In particular, the following are recommended:

a) The use of linearizing circuits in conjunction with the hotwire

anemometer for measurement of flow parameters when turbulence levels are

excessively high (greater than 20%). The linearizing assumptions used for the hotwire equation derivation would then be valid.

b) The use of a multiplying circuit instead of the sum-and-difference circuit to obtain the direct measurement of $\overline{e_1 e_2}$ terms for the hotwire equations. This would minimize the experimental errors encountered in the hotwire signal handling.

c) The necessity of having identical resistances for all hotwire sensors of the probe so the same calibration curve applies to all. This is extremely important in fluctuation velocity measurements where arithmetic operation of hotwire signals is involved.

d) The necessity of precise measurement of hotwire angles with respect to the R-$\theta$-Z coordinate system. The velocities and turbulence quantities calculated by the analysis described in the chapter "Derivation of the Hotwire Equations" are sensitive to the direction cosine coefficients used in the equations.

e) The use of a precise traversing mechanism to survey the flow field and assure uniform orientation of the hotwire probe in the R-$\theta$-Z coordinate system.

This thesis has attempted to present a detailed description of analytical and experimental investigations on flow through a three-bladed axial flow inducer. Although the investigations are performed on an axial flow inducer of a specific configuration, certain methods and techniques which have been developed are applicable to all types of turbomachinery. In particular, the equations and method of solution used in the exact analysis program are completely general and are not restricted solely to the solution of inducer fluid flow. Similarly, the experimental techniques used in conjunction with the rotating three-

sensor hotwire anemometer can be applied to most turbomachinery applications where relative velocity measurements are desired.

REFERENCES

1. Acosta, A. J., "An Experimental Study of Cavitating Inducers,"
   Second Symposium on Naval Hydrodynamics, Washington, D. C.,
   August 1958.

2. Anand, A. K., et al., "Investigation of Boundary Layer and
   Turbulence Characteristics Inside the Passages of an Axial Flow
   Inducer," NASA Report CR-121248, July 1973.

3. Carnahan, B., Luther, H. A., and Wilkes, J. O., Applied Numerical
   Methods, New York, Wiley and Sons, Inc., 1969.

4. Cooper, P., and Bosch, H., "Three Dimensional Analysis of Inducer
   Fluid Flow," NASA Report CR-54836, TRW ER-6673A, February 1966.

5. Giesing, J. P., "Extension of the Douglas-Neumann Program to
   Problems of Lifting, Infinite Cascades," Douglas Aircraft
   Division Report LB-31653, July 1964.

6. Hinze, J. O., Turbulence, An Introduction to Its Mechanism and
   Theory, New York, McGraw Hill, 1961.

7. Lakshminarayana, B., "Investigation and Analysis of Flow
   Phenomena in Axial Flow Inducers," J. Fluids Engr., December 1973.

8. Lakshminarayana, B., "Investigation and Analysis of Flow
   Phenomena in Axial Flow Inducers," NASA Report CR-107267,
   October 1969.

9. Lakshminarayana, B., "Experimental and Analytical Investigation of
   Flow Through a Rocket Pump Inducer," Fluid Mechanics and Design of
   Turbomachinery, NASA SP 304, 1974.

10. Lakshminarayana, B., "Visualization Study of Flow in Axial Flow
    Inducers," J. Basic Engr., December 1972, pp. 777-787.

11. Lakshminarayana, B. and Anand, A. K., "Solidity Effects in Axial
    Flow Inducers," Second International J.S.M.E. Conference on Fluid
    Machinery and Fluidics, Tokyo, September 1972.

12. Lakshminarayana, B. and Poncet, A., "A Method of Measuring Three
    Dimensional Rotating Wakes Behind Turbomachinery Rotors," ASME
    Paper 73-FE-31, 1973. (To be published in J. Fluids Engr.)

13. Lakshminarayana, B. and White, M. T., "Airfoil in a Contracting or
    Diverging Stream," J. of Aircraft, Vol. 9, No. 5, May 1972,
    pp. 354-360.

138

14. Lakshminarayana, B., Jabbari, A., and Yamaoka, H., "Turbulent Boundary Layer on a Rotating Helical Blade," J. Fluid Mech. Vol. 51, Part 3, 1972, pp. 545-569.

15. McCafferty, H. G., "Errors in Measuring the Fluctuating Flow at the Discharge of an Inducer," M.S. Thesis, Department of Aerospace Engineering, The Pennsylvania State University, June 1967.

16. Meng, P. R., and Moore, R. D., "Hydrogen Cavitation Performance of 80.6° Helical Inducer Mounted in Line with Stationary Centerbody," NASA TM X-1935, 1970.

17. Montgomery, J. C., "Analytical Performance Characteristics and Outlet Flow Conditions of Constant and Variable Lead Helical Inducers for Cryogenic Pumps," NASA TN D-583, March 1961.

18. Mullan, P. J., "An Investigation of Cavitating Inducers for Turbopumps," Gas Turbine Laboratory, Massachusetts Institute of Technology, Report No. 53, May 1959.

19. Osborn, W. M., "Investigation of a Liquid-Fluorine Inducer and Main-Stage Pump Combination Designed for a Suction Specific Speed of 20.000," NASA TM X-1070, March 1965.

20. Poncet, A. and Lakshminarayana, B., "Investigations of Three Dimensional Flow Characteristics in a Three Bladed Rocket Pump Inducer," NASA Report CR-2290, 1973.

21. Sandercock, D. M., and Anderson, D. A., "Cavitation and Non Cavitation Performance of an 80.6° Flat Plate Helical Inducer at Three Rotational Speeds," NASA Technical Note D-1439, November 1962.

22. Schwarz, W. H., and Friehe, C. A., "Deviations from the Cosine Law for Yawed Cylindrical Anemometer Sensors," J. of Applied Mech., Paper No. 68-WA/APM-16, 1968.

23. Soltis, R. F., Anderson, D. A., and Sandercock, D. M., "Investigation of the Performance of a 78° Flat Plate Helical Inducer," NASA Technical Note D-1170, March 1962.

24. Soltis, R. F., Urasek, D. C., Miller, M. J., "Blade Element Performance of a Tandem-Bladed Inducer Tested in Water," NASA Technical Note D-5562, November 1969.

25. Wislicenus, G. F., Fluid Mechanics of Turbomachinery, Dover, Vol. II, 1965, pp. 646-683.

APPENDIX A

Flow Chart Diagrams of Exact Analysis Program

Incorporating Viscid and Inviscid Modifications

Read input data - revise if necessary

Yes

$\nu = 0.0$ ?

No

Set U, V, W = 0 on blade

31

Calculate initial outlet air angles

Calculate JACOBian coefficients

Yes

$\nu = 0.0$ ?

No

669

Read reference $C_f$ vs. $R_e$ curves

Develop $C_f$ vs. $R_e$ equations

670

Calculate all point densities in STATE

Calculate local STAR residual

Sequentially ADJust local variables except where fixed by boundary conditions

381

Do for
K = 2, KMAX
J = 1, JMAX
I = 1, IMAX

"DO LOOP"

No

Last cycle ?    Yes

No

Converged ?    Yes    Output routine

467

Calculate RMS residual

End

500

Calculate all point RESIDuals

Calculate $\tau_r$, $\tau_\theta$, $\tau_z$ in DLOSS

No

Yes    $\nu = 0.0$ ?

152

Initialize $\Delta U$, $\Delta V$, $\Delta W$, $\Delta p$ for next cycle

Recalculate downstream point RESIDuals

Recalculate downstream JACOBian coef.

Yes

No    Unload trailing edge ?

Flow Chart Diagram for Main Analysis Program.

```
┌──────────────┐        ┌──────────────────┐
│  Subroutine  │   99   │ Satisfy          │
│    RESID     │───────▶│ boundary         │
│              │        │ conditions,if    │
└──────────────┘        │ applicable       │
                        └──────────────────┘
                                 │
                                 ▼
     No            ┌──────────────────┐
  ◀────────────────│    Trailing      │
  │                │    edge?         │
  │                └──────────────────┘
  │                         │
  │                        Yes
  │                         ▼
  │                ┌──────────────────┐
  │                │ Satisfy          │
  │                │ Kutta            │
  │                │ Condition        │
  │                └──────────────────┘
  │                         │
  │                  401    ▼
  │                ┌──────────────────┐
  └───────────────▶│ Calculate all    │
                   │ derivatives      │
                   │ ∂   ∂   ∂        │
                   │ ──, ──, ──       │
                   │ ∂α  ∂β  ∂γ       │
                   └──────────────────┘
                            │
                            ▼
                   ┌──────────────────┐
                   │ Convert          │
                   │ derivatives to   │
                   │ cylindrical      │
                   │ coordinates      │
                   │ ∂   ∂   ∂        │
                   │ ──, ──, ──       │
                   │ ∂r  ∂θ  ∂z       │
                   └──────────────────┘
                            │
                            ▼
┌──────────────┐   No   ┌──────────────────┐
│ Calculate τr,│◀───────│    ν = 0.0       │
│ τθ, τz  in   │        │      ?           │
│    DLOSS     │        └──────────────────┘
└──────────────┘                │
       │                       Yes
       │              391       ▼
       ▼             ┌──────────────┐        ⎛        ⎞
┌──────────────┐     │  Calculate   │        │ Return │
│Calculate loss│────▶│Point Residual│───────▶│        │
│terms Fr, Fθ, │     └──────────────┘        ⎝        ⎠
│Fz            │
└──────────────┘
```
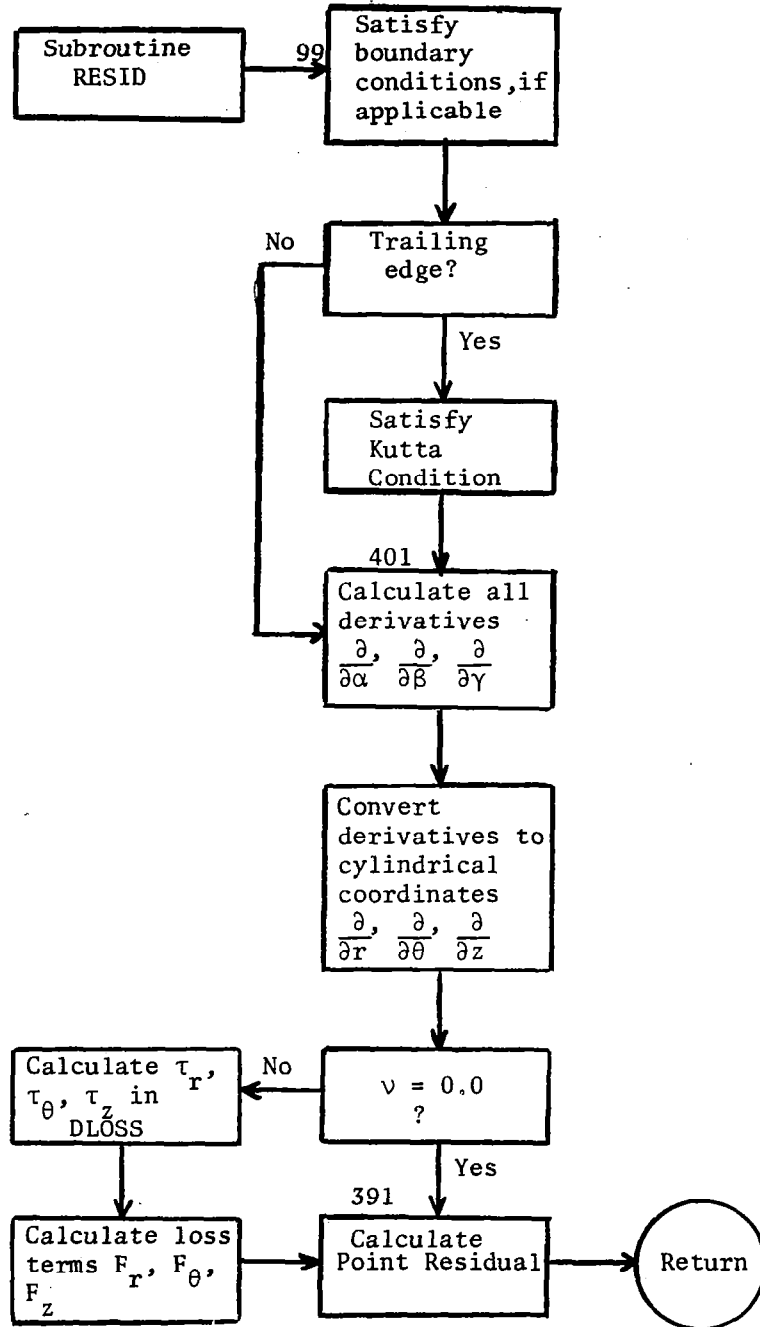
Flow Chart Diagram for Subroutine RESID

```
┌──────────────┐         ┌──────────────┐
│              │         │ Find passage-│
│  Subroutine  │────────▶│  averaged    │
│    DLOSS     │         │  velocity    │
│              │         │              │
└──────────────┘         └──────────────┘
                                 │
                                 ▼
                         ┌──────────────┐
                         │ Calculate R_e;│
                         │ Find C_f from │
                         │ interpolation │
                         │ of input      │
                         │ curves        │
                         └──────────────┘
                                 │
                                 ▼
                         ┌──────────────┐
                         │ Calculate    │
                         │ values of    │
                         │ wall shear   │
                         │ stress τ_w   │
                         └──────────────┘
                                 │
                                 ▼
                         ┌──────────────┐
                         │ Calculate    │
                         │ shear stress │
                         │ components   │
                         │ τ_r,τ_θ,τ_z at│
                         │ grid point   │
                         │ (I,J,K)      │
                         └──────────────┘
                                 │
                                 ▼
                            ╭─────────╮
                            │ Return  │
                            ╰─────────╯
```

Flow Chart Diagram for Subroutine DLOSS

# APPENDIX B

## Fortran Listing of Exact Analysis Program

## Incorporating Viscid and Inviscid Modifications

```
C
C      THREE DIMENSIONAL FLOW ANALYSIS IN PENN STATE INDUCER  JULY 1973
C
C      ORIGINAL PROGRAM DEVELOPED BY P. COOPER AND H. BOSCH OF
C          TRW ACCESSORIES DIVISION, CLEVELAND, OHIO
C
C      MODIFICATIONS MADE BY C. GORTON AT PENN STATE DURING SUMMER 1973
C
       IMPLICIT LOGICAL*1 ($)
       COMMON U(7,7,39),V(7,7,39),W(7,7,39),P(7,7,39),D(7,7,39),R(7,7,39)
      1,T(7,7,39),Z(7,7,39),FR,FT,FZ,DMAX(4),DELX(4),NSEQ(4),RES(8,8,40),
      2AR(7,7,39),AT(7,7,39),AZ(7,7,39),BR(7,7,39),BT(7,7,39),BZ(7,7,39),
      3CR(7,7,39),CT(7,7,39),CZ(7,7,39),XH,RSTAR,
      4TT,PSAT,DLIQ,REV,A,M,NVAR,NTR,IRSTAR,DX,I,J,K,II,JJ,KK,IMAX,JMAX,K
      5MAX,VISC,NBD,KLE,KTE,WRE(7,7,39)
       COMMON /$$LOSS/ TAUR(7,7,26),TAUT(7,7,26),TAUZ(7,7,26),TAU(7,7,26)
       COMMON/$$CFRE/ SLOPEP(25),SLOPES(25),BP(25),BS(25)
       COMMON /$$STRT/ KSTART
       DIMENSION CFS(2),CFP(2)
       DIMENSION THETA(3),REREF1(3),REREF2(3),CFREFP(2,3),CFREFS(2,3)
       DIMENSION DEV(7),DEL(7)
C
C      READ INITIAL DATA FROM TAPE
C
       READ(91)IMAX,JMAX,KMAX,KLE,KTE
       READ(91)(((R(I,J,K),I=1,IMAX),J=1,JMAX),K=1,KMAX)
       READ(91)(((T(I,J,K),I=1,IMAX),J=1,JMAX),K=1,KMAX)
       READ(91)(((Z(I,J,K),I=1,IMAX),J=1,JMAX),K=1,KMAX)
       READ(91)KOUNT,NUM,M,(NSEQ(L),L=1,4)
       READ(91)(DMAX(L),L=1,4),A,CRIT,E
       READ(91)REV,DLIQ,PSAT,TT,VISC
       READ(91)(((U(I,J,K),I=1,IMAX),J=1,JMAX),K=1,KMAX)
       READ(91)(((V(I,J,K),I=1,IMAX),J=1,JMAX),K=1,KMAX)
       READ(91)(((W(I,J,K),I=1,IMAX),J=1,JMAX),K=1,KMAX)
       READ(91)(((P(I,J,K),I=1,IMAX),J=1,JMAX),K=1,KMAX)
       REWIND 91
C
       JPRES=1
       JSUC=JMAX
       NBD=1
       NTR=0
       ANR=4*IMAX*JMAX*KMAX
C
C      UPDATE TAPE DATA
C
       READ(5,1004)KOUNT,NUM,M,(NSEQ(L),L=1,4)
       READ(5,1002)(DMAX(L),L=1,4),A,CRIT,E
       READ(5,1002)REV,DLIQ,PSAT,TT,VISC
       IF(VISC)32,31,32
C
C      IF VISCOSITY IS CONSIDERED, SET U,V,W EQUAL TO ZERO ON BLADE
C
    32 DO 17 K=KLE,KTE
       DO 17 I=1,IMAX
```

```
      DO 17 J=1,JMAX
      IF((J-1)*(JMAX-J))31,18,17
   18 U(I,J,K)=0.0
      V(I,J,K)=0.0
      W(I,J,K)=0.0
   17 CONTINUE
C
C     CALCULATE INITIAL OUTLET AIR ANGLES
C
   31 DO 121 I=1,IMAX
      IF(VISC)19,20,19
   20 DEL(I)=ATAN(V(I,JPRES,KTE)/W(I,JPRES,KTE))
      GO TO 21
   19 DEL(I)=ATAN(V(I,JPRES,KTE+1)/W(I,JPRES,KTE+1))
   21 DEL(I)=ABS(DEL(I))
      DDEL=DEL(I)*180./3.14159
  121 CONTINUE
C
C     CONVERT COORDINATE SYSTEMS
C
      KSTART=1
      CALL JACOB
      PRINT 1000
      NMAX=KOUNT+NUM
      PRINT 1007,IMAX,JMAX,KMAX,M,A,REV,DLIQ,PSAT,TT,VISC
      PRINT 1006,(NSEQ(L),L=1,4)
C
C     READ IN CF VS. RE CURVES FOR VARIOUS REFERENCE THETA LOCATIONS
C
      IF(VISC)669,670,669
  669 READ(5,700)NCURVE
      DO 710 I=1,NCURVE
      READ(5,720)THETA(I),REREF1(I),CFREFP(1,I),CFREFS(1,I),REREF2(I),CF
     1REFP(2,I),CFREFS(2,I)
      THETA(I)=THETA(I)*3.14159/180.
  710 CONTINUE
C
C     DEVELOP EQUATIONS OF CF VS. RE CURVES FOR ALL BLADE K VALUES
C
      DO 750 K=KLE,KTE
      I=IMAX
      DO 755 J1=1,2
      IF(J1.EQ.2)GO TO 756
C
C     J1=1  PRESSURE SURFACE           J1=2  SUCTION SURFACE
C
      J=1
      GO TO 757
  756 J=JMAX
  757 THET=ABS(T(I,J,K)-T(I,J,KLE))
C
C     SEARCH THETA REFERENCE VALUES
C
      DO 760 KK=1,NCURVE
```

```
      II=KK
      IF(THET.GT.THETA(II))GO TO 759
      IF(II.EQ.1)GO TO 762
      GO TO 761
  762 II=II+1
  761 RATIO=(THET-THETA(II-1))/(THETA(II)-THETA(II-1))
      GO TO 765
  759 IF(II.EQ.NCURVE)GO TO 761
  760 CONTINUE
  765 DO 740 JJ=1,2
      GO TO (780,785),J1
  780 CFP(JJ)=CFREFP(JJ,II-1)+RATIO*(CFREFP(JJ,II)-CFREFP(JJ,II-1))
      GO TO 740
  785 CFS(JJ)=CFREFS(JJ,II-1)+RATIO*(CFREFS(JJ,II)-CFREFS(JJ,II-1))
  740 CONTINUE
  755 CONTINUE
      JJ=1
      DENOM=ALOG10(REREF2(JJ))-ALOG10(REREF1(JJ))
      SLOPEP(K)=(ALOG10(CFP(JJ))-ALOG10(CFP(JJ+1)))/DENOM
      SLOPES(K)=(ALOG10(CFS(JJ))-ALOG10(CFS(JJ+1)))/DENOM
      BP(K)=CFP(JJ)*REREF1(JJ)**SLOPEP(K)
      BS(K)=CFS(JJ)*REREF1(JJ)**SLOPES(K)
  750 CONTINUE
C
C     CALCULATE POINT DENSITIES
C
C     INITIALIZE VALUES OF TAUR,TAUT,AND TAUZ IF NECESSARY
C
  670 DO 150 L=1,4
  150 DELX(L)=DMAX(L)
      DO 501 K=1,KMAX
      DO 501 J=1,JMAX
      DO 501 I=1,IMAX
      IF (TT)  502,503,502
  502 CALL STATE
      GO TO 120
  503 D(I,J,K)=DLIQ
  120 IF(VISC)385,501,385
  385 IF((K.LT.KLE).OR.(K.GT.KTE))GO TO 501
      CALL DLOSS
  501 CONTINUE
C
C     USE FRICTION VALUES TO FIND INITIAL FR,FT,FZ, AND RESIDUALS
C
      DO 140 K=1,KMAX
      DO 140 J=1,JMAX
      DO 140 I=1,IMAX
      IF (D(I,J,K))  500,500,500
  500 CALL RESID
  140 CONTINUE
      PRINT 1012
C
C     CALCULATE TOTAL ROOT-MEAN-SQUARE RESIDUAL
C
```

```
467 RT=0.0
    RESMAX=0.0
    RESMIN=RES(1,1,1)
    DO 368 K=1,KMAX
    DO 368 J=1,JMAX
    DO 368 I=1,IMAX
    IF(RES(I,J,K)-RESMAX)403,403,402
402 RESMAX=RES(I,J,K)
    GO TO 368
403 IF(RES(I,J,K)-RESMIN)404,368,368
404 RESMIN=RES(I,J,K)
368 RT=RT+RES(I,J,K)
    RMS=SQRT(RT/ANR)
    RESMAX=SQRT(RESMAX/4.)
    RESMIN=SQRT(RESMIN/4.)
    PRINT 1013,KOUNT,NTR,RMS,RESMAX,RESMIN,(DMAX(L),L=1,4)
    DO 151 L=1,4
151 DMAX(L)=0.0
    IF (RESMAX-CRIT*E)  369,369,370
370 KOUNT=KOUNT+1
    NTR=0
    IF (KOUNT-NMAX)  360,360,371
C
C     START SUCCESSIVE VARIATIONS CYCLE
C
C     CHANGE OUTLET AIR ANGLE AND DOWNSTREAM COORDINATES IF NECESSARY
C
360 KBEGIN=2
    KEND=KTE
    NTR=0
    $DELTA=.FALSE.
381 DO 460 KK=KBEGIN,KEND
    DO 460 JJ=1,JMAX
    DO 460 II=1,IMAX
    IRSTAR=1
    CALL STAR
    DO 460 L=1,4
    NVAR=NSEQ(L)
    GO TO (111,222,333,450),NVAR
111 IF (KK-2)  460,460,611
611 IF ((II-1)*(IMAX-II))  460,460,450
222 IF (KK-2)  460,460,481
481 IF (KK-KMAX)  450,482,460
482 IF ((JJ-1)*(JMAX-JJ))  460,460,450
333 IF (KK-2)  460,485,486
485 IF ((JJ-1)*(JMAX-JJ))  460,460,471
471 IF ((II-1)*(IMAX-II))  460,472,450
472 IF (AZ(II,JJ,KK))  460,450,460
486 IF (KK-KMAX)  487,460,460
487 IF((JJ-1)*(JMAX-JJ))460,460,450
450 CALL ADJ
460 CONTINUE
    IF(KEND-KMAX)461,152,152
461 K2=KTE+1
```

146

```
      DO 510 I=1,IMAX
C
C     CHANGE EXIT AIR ANGLE IF GREATER THAN TWO PERCENT OF PREVIOUS
C         EXIT AIR ANGLE
C
      PCNT2=.02*DEL(I)
      IF(VISC)25,26,25
   26 DELNEW=ABS(ATAN(V(I,JPRES,KTE)/W(I,JPRES,KTE)))
      GO TO 27
   25 DELNEW=ABS(ATAN(V(I,JPRES,KTE+1)/W(I,JPRES,KTE+1)))
   27 ABDEL=ABS(DELNEW-DEL(I))
      IF(ABDEL-PCNT2)510,540,540
  540 DEL(I)=DELNEW
      DDEL=DEL(I)*180./3.14159
      $DELTA=.TRUE.
      WRITE(6,55)I,DDEL
      DO 515 K=K2,KMAX
      DO 515 J=1,JMAX
      T(I,J,K)=T(I,J,KTE)+(Z(I,J,KTE)-Z(I,J,K))*TAN(DEL(I)))/R(I,J,K)
  515 CONTINUE
  510 CONTINUE
C
C     RE-CALCULATE JACOBIAN COEFFICIENTS FOR COORDINATE TRANSFORMATION
C
      IF(.NOT.$DELTA)GO TO 521
      KSTART=KTE
      CALL JACOB
C
C     RECALCULATE RESIDUALS
C
      NBD=1
      KKTE=KTE-1
      DO 520 K=KKTE,KMAX
      DO 520 J=1,JMAX
      DO 520 I=1,IMAX
      CALL RESID
  520 CONTINUE
  521 KBEGIN=KTE
      KEND=KMAX
      GO TO 381
  152 DO 153 L=1,4
      IF (DMAX(L))  561,562,561
  561 DELX(L)=DMAX(L)
      GO TO 153
  562 DELX(L)=DELX(L)*A
  153 CONTINUE
      GO TO 467
C
C     ***     OUTPUT   ROUTINE     ***
C
   98 WRITE(92)IMAX,JMAX,KMAX,KLE,KTE
      WRITE(92)(((R(I,J,K),I=1,IMAX),J=1,JMAX),K=1,KMAX)
      WRITE(92)(((T(I,J,K),I=1,IMAX),J=1,JMAX),K=1,KMAX)
      WRITE(92)(((Z(I,J,K),I=1,IMAX),J=1,JMAX),K=1,KMAX)
```

```
      KOUNT=KOUNT-1
      WRITE(92)KOUNT,NUM,M,(NSEQ(L),L=1,4)
      WRITE(92)(DELX(L),L=1,4),A,CRIT,E
      WRITE(92)REV,DLIQ,PSAT,TT,VISC
      WRITE(92)(((U(I,J,K),I=1,IMAX),J=1,JMAX),K=1,KMAX)
      WRITE(92)(((V(I,J,K),I=1,IMAX),J=1,JMAX),K=1,KMAX)
      WRITE(92)(((W(I,J,K),I=1,IMAX),J=1,JMAX),K=1,KMAX)
      WRITE(92)(((P(I,J,K),I=1,IMAX),J=1,JMAX),K=1,KMAX)
      END FILE 92
      REWIND 92
      DO 2 I=1,IMAX
      DO 2 J=1,JMAX
      DO 2 K=1,KMAX
    2 WRE(I,J,K)=SQRT(U(I,J,K)*U(I,J,K)+V(I,J,K)*V(I,J,K)+W(I,J,K)*W(I,J
     1,K))
      PRINT 1000
      DO 97 K=1,KMAX
      PRINT 1005
   97 PRINT 1003,((I,J,K,U(I,J,K),V(I,J,K),W(I,J,K),P(I,J,K),WRE(I,J,K),
     1RES(I,J,K),I=1,IMAX),J=1,JMAX)
      GO TO 99
  369 PRINT 1014
      GO TO 98
  371 PRINT 1015
      GO TO 98
C
C     FORMAT STATEMENTS
C
   55 FORMAT(32X,'*** OUTLET AIR ANGLE FOR I=',I2,' CHANGED TO',F10.3)
  700 FORMAT(9X,I1)
  720 FORMAT(F10.1,F10.0,F10.5,F10.5,F10.0,F10.5,F10.5)
 1000 FORMAT (75H0   3 DIMENSIONAL ANALYSIS OF SECONDARY FLOW IN PENN ST
     1ATE 3 BLADE INDUCER )
 1002 FORMAT(8F10.7)
 1003 FORMAT(3I3,6F18.7)
 1004 FORMAT(7I5)
 1005 FORMAT (//2X,1HI,2X,1HJ,2X,1HK,9X,1HU,17X,1HV,17X,1HW,17X,1HP,17X,
     13HVEL,13X,3HRES/)
 1006 FORMAT (2X23HADJUSTMENT SEQUENCE IS ,4I1,38H WHERE U IS 1, V IS 2,
     1 W IS 3, P IS 4.///)
 1007 FORMAT (I3,1HX,I2,1HX,I2,5H GRID,6X,2HM=,I2,6X,2HA=,1PE10.4//5H RE
     1V=,1PE10.4,5X,5HDLIQ=,1PE10.4,5X,5HPSAT=,1PE10.4,5X,3HTT=,1PE10.4,
     15X,5HVISC=,1PE10.4/)
 1012 FORMAT(/6H RELAX,3X,5HNO OF,5X,9HTOTAL RMS,7X,7HMAX RMS,7X,7HMIN R
     1MS,16X,44HMAGNITUDE OF BIGGEST ACCEPTED ADJUSTMENT FOR/6H CYCLE,3X
     1,5HTRIES,3(6X,8HRESIDUAL),17X,1HU,13X,1HV,13X,1HW,13X,1HP/)
 1013 FORMAT (I6,I8,1P3E14.4,8X,1P4E14.4)
 1014 FORMAT (/20X,9HCONVERGED/)
 1015 FORMAT (/20X,33HMAXIMUM NUMBER OF CYCLES EXECUTED/)
C
C     END OF PROGRAM
C
   99 STOP
      END
```

```
      SUBROUTINE JACOB
      IMPLICIT LOGICAL*1 ($)
C
C     CALCULATION OF JACOBIAN COEFFICIENTS FOR GENERAL-TO-CYLINDRICAL
C         COORDINATE TRANSFORMATION
C
      COMMON U(7,7,39),V(7,7,39),W(7,7,39),P(7,7,39),D(7,7,39),R(7,7,39)
     1,T(7,7,39),Z(7,7,39),FR,FT,FZ,DMAX(4),DELX(4),NSEQ(4),RES(8,8,40),
     2AR(7,7,39),AT(7,7,39),AZ(7,7,39),BR(7,7,39),BT(7,7,39),BZ(7,7,39),
     3CR(7,7,39),CT(7,7,39),CZ(7,7,39),XH,RSTAR,
     4TT,PSAT,DLIQ,REV,A,M,NVAR,NTR,IRSTAR,DX,I,J,K,II,JJ,KK,IMAX,JMAX,K
     5MAX,VISC,NBD,KLE,KTE,WRE(7,7,39)
      COMMON /$$STRT/ KSTART
      DO 18 K=KSTART,KMAX
      DO 18 J=1,JMAX
      DO 18 I=1,IMAX
      IF (I-1)  3,3,4
    3 RA=R(I+1,J,K)-R(I,J,K)
      TA=T(I+1,J,K)-T(I,J,K)
      ZA=Z(I+1,J,K)-Z(I,J,K)
      GO TO 7
    4 IF (I-IMAX)  5,6,6
    5 RA=(R(I+1,J,K)-R(I-1,J,K))/2.
      TA=(T(I+1,J,K)-T(I-1,J,K))/2.
      ZA=(Z(I+1,J,K)-Z(I-1,J,K))/2.
      GO TO 7
    6 RA=R(I,J,K)-R(I-1,J,K)
      TA=T(I,J,K)-T(I-1,J,K)
      ZA=Z(I,J,K)-Z(I-1,J,K)
    7 IF (J-1)  8,8,9
    8 RB=R(I,J+1,K)-R(I,J,K)
      TB=T(I,J+1,K)-T(I,J,K)
      ZB=Z(I,J+1,K)-Z(I,J,K)
      GO TO 12
    9 IF (J-JMAX)  10,11,11
   10 RB=(R(I,J+1,K)-R(I,J-1,K))/2.
      TB=(T(I,J+1,K)-T(I,J-1,K))/2.
      ZB=(Z(I,J+1,K)-Z(I,J-1,K))/2.
      GO TO 12
   11 RB=R(I,J,K)-R(I,J-1,K)
      TB=T(I,J,K)-T(I,J-1,K)
      ZB=Z(I,J,K)-Z(I,J-1,K)
   12 IF (K-1)  13,13,14
   13 RC=R(I,J,K+1)-R(I,J,K)
      TC=T(I,J,K+1)-T(I,J,K)
      ZC=Z(I,J,K+1)-Z(I,J,K)
      GO TO 17
   14 IF (K-KMAX)  15,16,16
   15 RC=(R(I,J,K+1)-R(I,J,K-1))/2.
      TC=(T(I,J,K+1)-T(I,J,K-1))/2.
      ZC=(Z(I,J,K+1)-Z(I,J,K-1))/2.
      GO TO 17
   16 RC=R(I,J,K)-R(I,J,K-1)
      TC=T(I,J,K)-T(I,J,K-1)
```

```
      ZC=Z(I,J,K)-Z(I,J,K-1)
17 B=RA*(TB*ZC-TC*ZB)+RB*(TC*ZA-TA*ZC)+RC*(TA*ZB-TB*ZA)
      AR(I,J,K)=(TB*ZC-TC*ZB)/B
      BR(I,J,K)=(TC*ZA-TA*ZC)/B
      CR(I,J,K)=(TA*ZB-TB*ZA)/B
      AT(I,J,K)=(ZB*RC-ZC*RB)/B
      BT(I,J,K)=(ZC*RA-ZA*RC)/B
      CT(I,J,K)=(ZA*RB-ZB*RA)/B
      AZ(I,J,K)=(RB*TC-RC*TB)/B
      BZ(I,J,K)=(RC*TA-RA*TC)/B
18 CZ(I,J,K)=(RA*TB-RB*TA)/B
      RETURN
      END
```

```
      SUBROUTINE RESID
      IMPLICIT LOGICAL*1 ($)
C
C     CALCULATION OF POINT RESIDUAL
C
      COMMON U(7,7,39),V(7,7,39),W(7,7,39),P(7,7,39),D(7,7,39),R(7,7,39)
     1,T(7,7,39),Z(7,7,39),FR,FT,FZ,DMAX(4),DELX(4),NSEQ(4),RES(8,8,40),
     2AR(7,7,39),AT(7,7,39),AZ(7,7,39),BR(7,7,39),BT(7,7,39),BZ(7,7,39),
     3CR(7,7,39),CT(7,7,39),CZ(7,7,39),XH,RSTAR,
     4TT,PSAT,DLIQ,REV,A,M,NVAR,NTR,IRSTAR,DX,I,J,K,II,JJ,KK,IMAX,JMAX,K
     5MAX,VISC,NBD,KLE,KTE,WRE(7,7,39)
      COMMON /$$LOSS/ TAUR(7,7,26),TAUT(7,7,26),TAUZ(7,7,26),TAU(7,7,26)
      COMMON/$$CFRE/ SLOPEP(25),SLOPES(25),BP(25),BS(25)
      IF (NBD)  400,401,99
C
C     CHECK WALL BOUNDARY CONDITIONS
C
   99 IF (K-2)  401,100,103
C
C     ***     K=2     ***
C
  100 IF ((I-1)*(IMAX-I))  400,121,124
  121 IF ((J-1)*(JMAX-J))  400,102,122
  122 IF (AZ(I,J,K))  123,351,123
  123 W(I,J,K)=-U(I,J,K)*AR(I,J,K)/AZ(I,J,K)
      GO TO 351
  124 IF ((J-1)*(JMAX-J))  400,111,351
  102 DDD=(BT(I,J,K)/R(I,J,K))/(AR(I,J,K)*BZ(I,J,K)-BR(I,J,K)*AZ(I,J,K))
      W(I,J,K)=-V(I,J,K)*AR(I,J,K)*DDD
      GO TO 351
  103 IF (K-KMAX)  108,104,400
C
C     ***     K=KMAX     ***
C
  104 IF ((I-1)*(IMAX-I))  400,105,106
  105 U(I,J,K)=-W(I,J,K)*AZ(I,J,K)/AR(I,J,K)
  106 IF ((J-1)*(JMAX-J))  400,107,351
  107 V(I,J,K)=-R(I,J,K)*(U(I,J,K)*BR(I,J,K)+W(I,J,K)*BZ(I,J,K))/BT(I,J,
     1K)
      GO TO 351
  108 IF(K-KTE)12,8,8
C
C     ***     K.GE.KTE     ***
C
C     FORCE VELOCITIES AND PRESSURES TO SATISFY KUTTA CONDITION
C
    8 IF((J-1)*(JMAX-J))12,11,12
   11 P(I,J,K)=(P(I,1,K)+P(I,7,K))/2.
      U(I,J,K)=(U(I,1,K)+U(I,7,K))/2.
      V(I,J,K)=(V(I,1,K)+V(I,7,K))/2.
      W(I,J,K)=(W(I,1,K)+W(I,7,K))/2.
C
C     ***     K IS NEITHER 2 NOR KMAX     ***
C
```

151

```
     12 IF ((I-1)*(IMAX-I)) 400,109,110
    109 IF ((J-1)*(JMAX-J))  400,112,114
    110 IF ((J-1)*(JMAX-J))  400,111,351
    111 W(I,J,K)=-(U(I,J,K)*BR(I,J,K)+V(I,J,K)*BT(I,J,K)/R(I,J,K))/BZ(I,J,
       1K)
        GO TO 351
    112 DDD=(BT(I,J,K)/R(I,J,K))/(AR(I,J,K)*BZ(I,J,K)-BR(I,J,K)*AZ(I,J,K))
        W(I,J,K)=-V(I,J,K)*AR(I,J,K)*DDD
        U(I,J,K)=V(I,J,K)*AZ(I,J,K)*DDD
        GO TO 351
    114 U(I,J,K)=-W(I,J,K)*AZ(I,J,K)/AR(I,J,K)
    351 IF((K.LT.KLE).OR.(K.GT.KTE))GO TO 401
        IF(VISC)402,401,402
C
C       FOR VISCOUS SOLUTION, BLADE SURFACES HAVE ZERO VELOCITY
C
    402 IF((J-1)*(JMAX-J))400,403,401
    403 U(I,J,K)=0.0
        V(I,J,K)=0.0
        W(I,J,K)=0.0
C
C       CALCULATE ALL DERIVATIVES
C
    401 IF(I-1)400,354,353
    354 UA=(U(I+1,J,K)-U(I,J,K))
        VA=(V(I+1,J,K)-V(I,J,K))
        WA=(W(I+1,J,K)-W(I,J,K))
        PA=(P(I+1,J,K)-P(I,J,K))
        IF (TT)  511,357,511
    511 DA=(D(I+1,J,K)-D(I,J,K))
        GO TO 357
    353 IF (I-IMAX)  355,356,400
    356 UA=(U(I,J,K)-U(I-1,J,K))
        VA=(V(I,J,K)-V(I-1,J,K))
        WA=(W(I,J,K)-W(I-1,J,K))
        PA=(P(I,J,K)-P(I-1,J,K))
        IF (TT)  521,357,521
    521 DA=(D(I,J,K)-D(I-1,J,K))
        GO TO 357
    355 UA=(U(I+1,J,K)-U(I-1,J,K))/2.
        VA=(V(I+1,J,K)-V(I-1,J,K))/2.
        WA=(W(I+1,J,K)-W(I-1,J,K))/2.
        PA=(P(I+1,J,K)-P(I-1,J,K))/2.
        IF (TT)  531,357,531
    531 DA=(D(I+1,J,K)-D(I-1,J,K))/2.
    357 IF (J-1)  400,359,358
    359 UB=(U(I,J+1,K)-U(I,J,K))
        VB=(V(I,J+1,K)-V(I,J,K))
        WB=(W(I,J+1,K)-W(I,J,K))
        PB=(P(I,J+1,K)-P(I,J,K))
        IF (TT)  541,362,541
    541 DB=(D(I,J+1,K)-D(I,J,K))
        GO TO 362
    358 IF (J-JMAX)  360,361,400
```

```
  361 UB=(U(I,J,K)-U(I,J-1,K))
      VB=(V(I,J,K)-V(I,J-1,K))
      WB=(W(I,J,K)-W(I,J-1,K))
      PB=(P(I,J,K)-P(I,J-1,K))
      IF (TT)  551,362,551
  551 DB=(D(I,J,K)-D(I,J-1,K))
      GO TO 362
  360 UB=(U(I,J+1,K)-U(I,J-1,K))/2.
      VB=(V(I,J+1,K)-V(I,J-1,K))/2.
      WB=(W(I,J+1,K)-W(I,J-1,K))/2.
      PB=(P(I,J+1,K)-P(I,J-1,K))/2.
      IF (TT)  561,362,561
  561 DB=(D(I,J+1,K)-D(I,J-1,K))/2.
  362 IF (K-1)  400,364,363
  364 UC=(U(I,J,K+1)-U(I,J,K))
      VC=(V(I,J,K+1)-V(I,J,K))
      WC=(W(I,J,K+1)-W(I,J,K))
      PC=(P(I,J,K+1)-P(I,J,K))
      IF (TT)  571,367,571
  571 DC=(D(I,J,K+1)-D(I,J,K))
      GO TO 367
  363 IF (K-KMAX)  365,366,400
  366 UC=(U(I,J,K)-U(I,J,K-1))
      VC=(V(I,J,K)-V(I,J,K-1))
      WC=(W(I,J,K)-W(I,J,K-1))
      PC=(P(I,J,K)-P(I,J,K-1))
      IF (TT)  581,367,581
  581 DC=(D(I,J,K)-D(I,J,K-1))
      GO TO 367
  365 UC=(U(I,J,K+1)-U(I,J,K-1))/2.
      VC=(V(I,J,K+1)-V(I,J,K-1))/2.
      WC=(W(I,J,K+1)-W(I,J,K-1))/2.
      PC=(P(I,J,K+1)-P(I,J,K-1))/2.
      IF (TT)  591,367,591
  591 DC=(D(I,J,K+1)-D(I,J,K-1))/2.
C
C     CONVERT ALL DERIVATIVES FROM GENERAL TO CYLINDRICAL COORDINATES
C
  367 UR=AR(I,J,K)*UA+BR(I,J,K)*UB+CR(I,J,K)*UC
      UT=AT(I,J,K)*UA+BT(I,J,K)*UB+CT(I,J,K)*UC
      UZ=AZ(I,J,K)*UA+BZ(I,J,K)*UB+CZ(I,J,K)*UC
      VR=AR(I,J,K)*VA+BR(I,J,K)*VB+CR(I,J,K)*VC
      VT=AT(I,J,K)*VA+BT(I,J,K)*VB+CT(I,J,K)*VC
      VZ=AZ(I,J,K)*VA+BZ(I,J,K)*VB+CZ(I,J,K)*VC
      WR=AR(I,J,K)*WA+BR(I,J,K)*WB+CR(I,J,K)*WC
      WT=AT(I,J,K)*WA+BT(I,J,K)*WB+CT(I,J,K)*WC
      WZ=AZ(I,J,K)*WA+BZ(I,J,K)*WB+CZ(I,J,K)*WC
      PR=AR(I,J,K)*PA+BR(I,J,K)*PB+CR(I,J,K)*PC
      PT=AT(I,J,K)*PA+BT(I,J,K)*PB+CT(I,J,K)*PC
      PZ=AZ(I,J,K)*PA+BZ(I,J,K)*PB+CZ(I,J,K)*PC
      IF (TT)  370,375,370
  370 DR=AR(I,J,K)*DA+BR(I,J,K)*DB+CR(I,J,K)*DC
      DT=AT(I,J,K)*DA+BT(I,J,K)*DB+CT(I,J,K)*DC
      DZ=AZ(I,J,K)*DA+BZ(I,J,K)*DB+CZ(I,J,K)*DC
```

```
          GO TO 380
      375 DR=0.0
          DT=0.0
          DZ=0.0
      380 UU=U(I,J,K)
          VV=V(I,J,K)
          WW=W(I,J,K)
          DD=D(I,J,K)
          RR=R(I,J,K)
C
C         CALCULATE LOSS TERMS
C
          IF(VISC)385,390,385
      385 IF((K.LT.KLE).OR.(K.GT.KTE))GO TO 390
          CALL DLOSS
          IF(I-1)400,501,502
      501 TRA=TAUR(I+1,J,K)-TAUR(I,J,K)
          TTA=TAUT(I+1,J,K)-TAUT(I,J,K)
          TZA=TAUZ(I+1,J,K)-TAUZ(I,J,K)
          GO TO 503
      502 IF(I-IMAX)504,505,400
      505 TRA=TAUR(I,J,K)-TAUR(I-1,J,K)
          TTA=TAUT(I,J,K)-TAUT(I-1,J,K)
          TZA=TAUZ(I,J,K)-TAUZ(I-1,J,K)
          GO TO 503
      504 TRA=(TAUR(I+1,J,K)-TAUR(I-1,J,K))/2.
          TTA=(TAUT(I+1,J,K)-TAUT(I-1,J,K))/2.
          TZA=(TAUZ(I+1,J,K)-TAUZ(I-1,J,K))/2.
      503 IF(J-1)400,506,507
      506 TRB=TAUR(I,J+1,K)-TAUR(I,J,K)
          TTB=TAUT(I,J+1,K)-TAUT(I,J,K)
          TZB=TAUZ(I,J+1,K)-TAUZ(I,J,K)
          GO TO 508
      507 IF(J-JMAX)509,510,400
      510 TRB=TAUR(I,J,K)-TAUR(I,J-1,K)
          TTB=TAUT(I,J,K)-TAUT(I,J-1,K)
          TZB=TAUZ(I,J,K)-TAUZ(I,J-1,K)
          GO TO 508
      509 TRB=(TAUR(I,J+1,K)-TAUR(I,J-1,K))/2.
          TTB=(TAUT(I,J+1,K)-TAUT(I,J-1,K))/2.
          TZB=(TAUZ(I,J+1,K)-TAUZ(I,J-1,K))/2.
      508 IF(K-KLE)390,518,512
      518 TRC=TAUR(I,J,K+1)-TAUR(I,J,K)
          TTC=TAUT(I,J,K+1)-TAUT(I,J,K)
          TZC=TAUZ(I,J,K+1)-TAUZ(I,J,K)
          GO TO 513
      512 IF(K-KTE)514,515,390
      515 TRC=TAUR(I,J,K)-TAUR(I,J,K-1)
          TTC=TAUT(I,J,K)-TAUT(I,J,K-1)
          TZC=TAUZ(I,J,K)-TAUZ(I,J,K-1)
          GO TO 513
      514 TRC=(TAUR(I,J,K+1)-TAUR(I,J,K-1))/2.
          TTC=(TAUT(I,J,K+1)-TAUT(I,J,K-1))/2.
          TZC=(TAUZ(I,J,K+1)-TAUZ(I,J,K-1))/2.
```

154

```
  513 TRWZ=AZ(I,J,K)*TRA+BZ(I,J,K)*TRB+CZ(I,J,K)*TRC
      TTWZ=AZ(I,J,K)*TTA+BZ(I,J,K)*TTB+CZ(I,J,K)*TTC
      TZWT=AT(I,J,K)*TZA+BT(I,J,K)*TZB+CT(I,J,K)*TZC
      FR=-TRWZ/DD
      FT=-TTWZ/DD
      FZ=-TZWT/(DD*RR)
      GO TO 391
  390 FR=0.0
      FT=0.0
      FZ=0.0
C
C     CALCULATE POINT RESIDUALS
C
  391 R1=PR/DD+UU*UR+VV*UT/RR+WW*UZ-((VV+RR*REV)*(VV+RR*REV))/RR+FR
      R2=PT/(DD*RR)+UU*VR+VV*VT/RR+WW*VZ+UU*VV/RR+2.*UU*REV+FT
      R3=PZ/DD+UU*WR+VV*WT/RR+WW*WZ+FZ
      R4=UU/RR+UR+VT/RR+WZ+(UU*DR+VV*DT/RR+WW*DZ)/DD
      RES(I,J,K)=R1*R1+R2*R2+R3*R3+R4*R4
  400 RETURN
      END
```

```
      SUBROUTINE DLOSS
      IMPLICIT LOGICAL*1 ($)
C
C     CALCULATION OF LOSS TERMS IN MOMENTUM EQUATIONS
C
      COMMON U(7,7,39),V(7,7,39),W(7,7,39),P(7,7,39),D(7,7,39),R(7,7,39)
     1,T(7,7,39),Z(7,7,39),FR,FT,FZ,DMAX(4),DELX(4),NSEQ(4),RES(8,8,40),
     2AR(7,7,39),AT(7,7,39),AZ(7,7,39),BR(7,7,39),BT(7,7,39),BZ(7,7,39),
     3CR(7,7,39),CT(7,7,39),CZ(7,7,39),XH,RSTAR,
     4TT,PSAT,DLIQ,REV,A,M,NVAR,NTR,IRSTAR,DX,I,J,K,II,JJ,KK,IMAX,JMAX,K
     5MAX,VISC,NBD,KLE,KTE,WRE(7,7,39)
      COMMON /$$LOSS/ TAUR(7,7,26),TAUT(7,7,26),TAUZ(7,7,26),TAU(7,7,26)
      COMMON/$$CFRE/ SLOPEP(25),SLOPES(25),BP(25),BS(25)
      DIMENSION VEL(7)
C
C     OMEGA AND RTIP ARE SPECIFIC PARAMETERS OF PENN STATE INDUCER
C
      OMEGA=450.*3.14159/30.
      RTIP=18.25/12.
      DEN=D(I,J,K)
      JMIN=1
      UBAR=0.0
      UTIP=RTIP*OMEGA
C
C     FIND PASSAGE AVERAGED VELOCITY
C
      DO 100 J1=1,JMAX
      VEL(J1)=SQRT(U(I,J1,K)*U(I,J1,K)+V(I,J1,K)*V(I,J1,K)+W(I,J1,K)*W(I
     1,J1,K))
      UBAR=UBAR+VEL(J1)
  100 CONTINUE
      XJMAX=JMAX
      UBAR=UBAR/XJMAX
C
C     CALCULATE REYNOLDS NUMBER, FIND APPROPRIATE SKIN FRICTION
C         COEFFICIENT, THEN CALCULATE THE COMPONENTS OF SHEAR STRESS
C
      UU=UBAR*UTIP
      RR=R(I,J,K)*RTIP
      RE=UU*RR/VISC
      CF1=BP(K)/(RE**SLOPEP(K))
      CF2=BS(K)/(RE**SLOPES(K))
      TAU1=CF1*DEN*UBAR**2./2.
      TAU2=-CF2*DEN*UBAR**2./2.
      XNUM=J-JMIN
      XDEN=JMAX-JMIN
      RATIO=XNUM/XDEN
      TAU(I,J,K)=TAU1-RATIO*(TAU1-TAU2)
      IF(J-1)400,359,358
  359 DELU=(U(I,J+1,K)-U(I,J,K))
      DELV=(V(I,J+1,K)-V(I,J,K))
      DELW=(W(I,J+1,K)-W(I,J,K))
      DELVEL=(VEL(J+1)-VEL(J))
      GO TO 362
```

```
358 IF (J-JMAX)  360,361,400
361 DELU=(U(I,J,K)-U(I,J-1,K))
    DELV=(V(I,J,K)-V(I,J-1,K))
    DELW=(W(I,J,K)-W(I,J-1,K))
    DELVEL=(VEL(J)-VEL(J-1))
    GO TO 362
360 DELU=(U(I,J+1,K)-U(I,J-1,K))/2.
    DELV=(V(I,J+1,K)-V(I,J-1,K))/2.
    DELW=(W(I,J+1,K)-W(I,J-1,K))/2.
    DELVEL=(VEL(J+1)-VEL(J-1))/2.
362 TAUR(I,J,K)=TAU(I,J,K)*DELU/DELVEL
    TAUT(I,J,K)=TAU(I,J,K)*DELV/DELVEL
    TAUZ(I,J,K)=TAU(I,J,K)*DELW/DELVEL
400 RETURN
    END
```

```
      SUBROUTINE ADJ
      IMPLICIT LOGICAL*1 ($)
C
C     REDUCTION OF TOTAL RESIDUAL BY SUCCESSIVE VARIATIONS OF
C          PARAMETERS U, V, W, P
C
      COMMON U(7,7,39),V(7,7,39),W(7,7,39),P(7,7,39),D(7,7,39),R(7,7,39)
     1,T(7,7,39),Z(7,7,39),FR,FT,FZ,DMAX(4),DELX(4),NSEQ(4),RES(8,8,40),
     2AR(7,7,39),AT(7,7,39),AZ(7,7,39),BR(7,7,39),BT(7,7,39),BZ(7,7,39),
     3CR(7,7,39),CT(7,7,39),CZ(7,7,39),XH,RSTAR,
     4TT,PSAT,DLIQ,REV,A,M,NVAR,NTR,IRSTAR,DX,I,J,K,II,JJ,KK,IMAX,JMAX,K
     5MAX,VISC,NBD,KLE,KTE,WRE(7,7,39)
C
C     CURRENT VALUES OF ALL AFFECTED QUANTITIES TEMPORARILY STORED
C
      H1=RES(II,JJ,KK)
      IF (II-1) 1101,1101,1100
 1100 H2=RES(II-1,JJ,KK)
 1101 IF (II-IMAX) 1102,1103,1103
 1102 H3=RES(II+1,JJ,KK)
 1103 IF (JJ-1) 1105,1105,1104
 1104 H4=RES(II,JJ-1,KK)
 1105 IF (JJ-JMAX) 1106,1107,1107
 1106 H5=RES(II,JJ+1,KK)
 1107 IF (KK-1) 1109,1109,1108
 1108 H6=RES(II,JJ,KK-1)
 1109 IF (KK-KMAX) 1110,1111,1111
 1110 H7=RES(II,JJ,KK+1)
 1111 RHLD=RSTAR
      DX=DELX(NVAR)
      HU=U(II,JJ,KK)
      HV=V(II,JJ,KK)
      HW=W(II,JJ,KK)
      HP=P(II,JJ,KK)
      HD=D(II,JJ,KK)
C
C     SUCCESSIVELY APPLY TRIAL VARIATIONS TO U, V, W, P
C
    5 DO 480 MA=1,M
  420 GO TO (422,423,424,425),NVAR
  422 U(II,JJ,KK)=HU+DX
      GO TO 421
  423 V(II,JJ,KK)=HV+DX
      GO TO 421
  424 W(II,JJ,KK)=HW+DX
      GO TO 421
  425 P(II,JJ,KK)=HP+DX
      IF (TT) 461,421,461
  461 I=II
      J=JJ
      K=KK
      CALL STATE
  421 NTR=NTR+1
      IRSTAR=2
```

158

```
      CALL STAR
      IF (RHLD-RSTAR)  430,430,431
  431 IF (ABS(DX)-DMAX(NVAR))  457,457,920
  920 DMAX(NVAR)=ABS(DX)
      GO TO 457
  430 IF (DX)  433,457,432
  432 DX=-DX
      GO TO 420
  433 DX=-A*DX
  480 CONTINUE
C
C     RESTORE ALL AFFECTED QUANTITIES TO ORIGINAL VALUES
C
      U(II,JJ,KK)=HU
      V(II,JJ,KK)=HV
      W(II,JJ,KK)=HW
      P(II,JJ,KK)=HP
      D(II,JJ,KK)=HD
  445 RSTAR=RHLD
      RES(II,JJ,KK)=H1
      IF (II-1)  446,446,447
  447 RES(II-1,JJ,KK)=H2
  446 IF (II-IMAX)  449,448,448
  449 RES(II+1,JJ,KK)=H3
  448 IF (JJ-1)  450,450,451
  451 RES(II,JJ-1,KK)=H4
  450 IF (JJ-JMAX)  453,452,452
  453 RES(II,JJ+1,KK)=H5
  452 IF (KK-1)  454,454,455
  455 RES(II,JJ,KK-1)=H6
  454 IF (KK-KMAX)  456,457,457
  456 RES(II,JJ,KK+1)=H7
  457 RETURN
      END
```

```
      SUBROUTINE STAR
      IMPLICIT LOGICAL*1 ($)
C
C     CALCULATION OF LOCAL STAR RESIDUAL
C
      COMMON U(7,7,39),V(7,7,39),W(7,7,39),P(7,7,39),D(7,7,39),R(7,7,39)
     1,T(7,7,39),Z(7,7,39),FR,FT,FZ,DMAX(4),DELX(4),NSEQ(4),RES(8,8,40),
     2AR(7,7,39),AT(7,7,39),AZ(7,7,39),BR(7,7,39),BT(7,7,39),BZ(7,7,39),
     3CR(7,7,39),CT(7,7,39),CZ(7,7,39),XH,RSTAR,
     4TT,PSAT,DLIQ,REV,A,M,NVAR,NTR,IRSTAR,DX,I,J,K,II,JJ,KK,IMAX,JMAX,K
     5MAX,VISC,NBD,KLE,KTE,WRE(7,7,39)
      RSTAR=0.0
      IGO=0
      I=II
      J=JJ
      K=KK
      NBD=1
  389 GO TO (375,378),IRSTAR
  378 CALL RESID
  375 RSTAR=RSTAR+RES(I,J,K)
      NBD=0
  400 IGO=IGO+1
      GO TO (391,392,393,394,395,396,402),IGO
  391 I=II-1
      IF (I-1)   400,389,389
  392 I=II+1
      IF (I-IMAX)   389,389,400
  393 I=II
      J=JJ-1
      IF (J-1) 400,389,389
  394 J=JJ+1
      IF (J-JMAX)   389,389,400
  395 J=JJ
      K=KK-1
      IF (K-1)   400,389,389
  396 K=KK+1
      IF (K-KMAX)   389,389,400
  402 RETURN
      END
```

```
      SUBROUTINE STATE
      IMPLICIT LOGICAL*1 ($)
C
C     CALCULATION OF POINT DENSITY
C
      COMMON U(7,7,39),V(7,7,39),W(7,7,39),P(7,7,39),D(7,7,39),R(7,7,39)
     1,T(7,7,39),Z(7,7,39),FR,FT,FZ,DMAX(4),DELX(4),NSEQ(4),RES(8,8,40),
     2AR(7,7,39),AT(7,7,39),AZ(7,7,39),BR(7,7,39),BT(7,7,39),BZ(7,7,39),
     3CR(7,7,39),CT(7,7,39),CZ(7,7,39),XH,RSTAR,
     4TT,PSAT,DLIQ,REV,A,M,NVAR,NTR,IRSTAR,DX,I,J,K,II,JJ,KK,IMAX,JMAX,K
     5MAX,VISC,NBD,KLE,KTE,WRE(7,7,39)
      PSP=PSAT-P(I,J,K)
      IF (PSP)  101,101,102
  101 D(I,J,K)=DLIQ
      GO TO 103
  102 D(I,J,K)=DLIQ/(1.+TT*PSP)
  103 RETURN
      END
```

# APPENDIX C

## Fortran Listing of Program to Solve Hotwire Equations

```
C
C       ROTATING HOTWIRE MEASUREMENTS IN PENN STATE INDUCER  FALL 1973
C
C       PROGRAM DEVELOPED TO CALCULATE RELATIVE MEAN VELOCITIES,
C       TURBULENCE INTENSITIES AND STRESSES FROM THE EXPERIMENTAL DATA
C
        IMPLICIT LOGICAL*1 ($)
        DIMENSION FVOLT1(4,6,10),FVOLT2(4,6,10),FVOLT3(4,6,10)
        DIMENSION SLOPE1(4),SLOPE2(4),SLOPE3(4)
        DIMENSION FVEL1(6,10),FVEL2(6,10),FVEL3(6,10)
        DIMENSION V1(4,15),V2(4,15),V3(4,15)
        DIMENSION NPTS(15),CINCH(4,15),CALV1(4,15),CALV2(4,15),CVEL(4,15)
        DIMENSION VCHAN2(4,6,10),VEL1(6,10),VEL2(6,10)
        DIMENSION VCHAN3(4,6,10),VEL3(6,10),CALE3(4,15),CALV3(4,15)
        DIMENSION CALE1(4,15),CALE2(4,15),RRAD(6)
        DIMENSION THETA(10),RAD(6),VCHAN1(4,6,10)
        DIMENSION C(3,3),A(6,6),TEMP(10)
        REAL*8 CC(3,3),AA(6,6),D(3),B(6),DET
C
C       DEFINE PROGRAM CONSTANTS
C
        UTIP=450.*2.*3.14159*18.25/(60.*12.)
        FACT=SQRT(2.)/2.
        FACTOR=19./8.
        ATTEN=27.4
        RAT=3.14159/180.
C
C       READ IN CONVERGENCE CRITERIA
C
        READ(5,82)NREPS,EPS
C
C       READ IN HOTWIRE CONSTANTS FOR L/D
C
        READ(5,70)XK1,XK2,XK3
C
C       READ IN CALIBRATION CURVES
C
        READ(5,6)CALA1,CALA2,CALA3
        CALA1=CALA1*RAT
        CALA2=CALA2*RAT
        CALA3=CALA3*RAT
        READ(5,5)NCAL
        DO 100 I=1,NCAL
        READ(5,10)NPTS(I),TEMP(I)
        JJ=NPTS(I)
        DO 105 J=1,JJ
        READ(5,15)CINCH(I,J),CALE1(I,J),CALE2(I,J),CALE3(I,J)
        CVEL(I,J)=66.7*SQRT(CINCH(I,J))
C
C       APPLY TEMPERATURE CORRECTION TO CALIBRATION CURVES
C
        CVEL(I,J)=CVEL(I,J)*(1.0+0.001*(TEMP(J)-73.0))
        CALE1(I,J)=CALE1(I,J)*(1.0+0.0014*(TEMP(J)-73.0))
        CALE2(I,J)=CALE2(I,J)*(1.0+0.0014*(TEMP(J)-73.0))
```

```
      CALE3(I,J)=CALE3(I,J)*(1.0+0.0014*(TEMP(J)-73.0))
C
C     CORRECT CALIBRATION CURVE FOR SKEWED PROBE
C
      V1(I,J)=SQRT((CVEL(I,J)*COS(CALA1))**2.+XK1*XK1*(CVEL(I,J)*SIN(CAL
     1A1))**2.)
      V2(I,J)=SQRT((CVEL(I,J)*COS(CALA2))**2.+XK2*XK2*(CVEL(I,J)*SIN(CAL
     1A2))**2.)
      V3(I,J)=SQRT((CVEL(I,J)*COS(CALA3))**2.+XK3*XK3*(CVEL(I,J)*SIN(CAL
     1A3))**2.)
  105 CONTINUE
  100 CONTINUE
C
C     USE VOLTAGE SQUARED VS. ROOT VELOCITY CURVE FOR CALCULATIONS
C
      CALV1(I,J)=CALE1(I,J)**2.
      CALV2(I,J)=CALE2(I,J)**2.
      CALV3(I,J)=CALE3(I,J)**2.
      V1(I,J)=SQRT(V1(I,J))
      V2(I,J)=SQRT(V2(I,J))
      V3(I,J)=SQRT(V3(I,J))
  102 CONTINUE
  101 CONTINUE
      DO 103 I=1,NCAL
      SLOPE1(I)=(CALV1(I,4)-CALV1(I,2))/(V1(I,4)-V1(I,2))
      SLOPE2(I)=(CALV2(I,4)-CALV2(I,2))/(V2(I,4)-V2(I,2))
      SLOPE3(I)=(CALV3(I,4)-CALV3(I,2))/(V3(I,4)-V3(I,2))
  103 CONTINUE
C
C     SPECIFY RADIAL AND TANGENTIAL MEASUREMENT LOCIATIONS
C
      READ(5,20)NOR,NOT
      READ(5,25)(THETA(I),I=1,NOT)
      READ(5,32)(RAD(I),I=1,NOR)
      DO 112 I=1,NOR
      RRAD(I)=(18.25-RAD(I))/18.25
  112 CONTINUE
C
C     READ IN DIRECTION COSINES - THESE CAN BE CALCULATED WITHIN THE
C     PROGRAM IF CODED TO DO SO
C
      READ(5,70)A1,B1,C1
      READ(5,70)A2,B2,C2
      READ(5,70)A3,B3,C3
      READ(5,70)D1,E1,F1
      READ(5,70)D2,E2,F2
      READ(5,70)D3,E3,F3
      READ(5,70)G1,XH1,XI1
      READ(5,70)G2,XH2,XI2
      READ(5,70)G3,XH3,XI3
C
C     CALCULATE EQUATION COEFFICIENTS
C
      A4=XK1*XK1*A1*A1+A2*A2+A3*A3
```

```
      B4=XK1*XK1*B1*B1+B2*B2+B3*B3
      C4=XK1*XK1*C1*C1+C2*C2+C3*C3
      D4=2.*(XK1*XK1*A1*B1+A2*B2+A3*B3)
      E4=2.*(XK1*XK1*A1*C1+A2*C2+A3*C3)
      F4=2.*(XK1*XK1*B1*C1+B2*C2+B3*C3)
C
      A5=XK2*XK2*D1*D1+D2*D2+D3*D3
      B5=XK2*XK2*E1*E1+E2*E2+E3*E3
      C5=XK2*XK2*F1*F1+F2*F2+F3*F3
      D5=2.*(XK2*XK2*D1*E1+D2*E2+D3*E3)
      E5=2.*(XK2*XK2*D1*F1+D2*F2+D3*F3)
      F5=2.*(XK2*XK2*E1*F1+E2*F2+E3*F3)
C
      A6=XK3*XK3*G1*G1+G2*G2+G3*G3
      B6=XK3*XK3*XH1*XH1+XH2*XH2+XH3*XH3
      C6=XK3*XK3*XI1*XI1+XI2*XI2+XI3*XI3
      D6=2.*(XK3*XK3*G1*XH1+G2*XH2+G3*XH3)
      E6=2.*(XK3*XK3*G1*XI1+G2*XI2+G3*XI3)
      F6=2.*(XK3*XK3*XH1*XI1+XH2*XI2+XH3*XI3)
C
      C(1,1)=SQRT(A4)
      C(1,2)=D4/(2.*C(1,1))
      C(1,3)=E4/(2.*C(1,1))
      C(2,1)=SQRT(A5)
      C(2,2)=D5/(2.*C(2,1))
      C(2,3)=E5/(2.*C(2,1))
      C(3,1)=SQRT(A6)
      C(3,2)=D6/(2.*C(3,1))
      C(3,3)=E6/(2.*C(3,1))
C
C     READ IN MEAN AND FLUCTUATING VOLTAGES, FIND CORRESPONDING VELOCITIES
C
      DO 115 J=1,NOT
      READ(5,40)IPRO,JRAD
      DO 110 I=1,JRAD
      IF(IPRO.EQ.9)GO TO 140
      IPROBE=IPRO
      READ(5,46)VCH1,VCH2,VCH3,EXTEMP
      READ(5,45)FV1SQ,FV2SQ,FV3SQ
      READ(5,75)FV1P2,FV1M2,FV1P3,FV1M3,FV2P3,FV2M3
      GO TO 145
  140 READ(5,47)VCH1,VCH2,VCH3,EXTEMP,IPROBE
      READ(5,45)FV1SQ,FV2SQ,FV3SQ
      READ(5,75)FV1P2,FV1M2,FV1P3,FV1M3,FV2P3,FV2M3
  145 VCHAN1(IPROBE,I,J)=VCH1
      VCHAN2(IPROBE,I,J)=VCH2
      VCHAN3(IPROBE,I,J)=VCH3

      APPLY TEMPERATURE CORRECTION TO EXPERIMENTAL DATA

      TCORR=1.0+0.0028*(EXTEMP-73.0)
      VCHAN1(IPROBE,I,J)=TCORR*VCHAN1(IPROBE,I,J)**2.
      VCHAN2(IPROBE,I,J)=TCORR*VCHAN2(IPROBE,I,J)**2.
      VCHAN3(IPROBE,I,J)=TCORR*VCHAN3(IPROBE,I,J)**2.
```

164

```
        JJ=NPTS(IPROBE)
        DO 120 K=1,JJ
        IF(VCHAN1(IPROBE,I,J).GT.CALV1(IPROBE,K))GO TO 120
        RATIO=(VCHAN1(IPROBE,I,J)-CALV1(IPROBE,K-1))/(CALV1(IPROBE,K)-CALV
       11(IPROBE,K-1))
        VEL1(I,J)=V1(IPROBE,K-1)+RATIO*(V1(IPROBE,K)-V1(IPROBE,K-1))
        VEL1(I,J)=VEL1(I,J)**2.
        K1=K
        GO TO 121
   120 CONTINUE
        RATIO=(VCHAN1(IPROBE,I,J)-CALV1(IPROBE,JJ-1))/(CALV1(IPROBE,JJ)-CA
       1LV1(IPROBE,JJ-1))
        VEL1(I,J)=V1(IPROBE,JJ-1)+RATIO*(V1(IPROBE,JJ)-V1(IPROBE,JJ-1))
        VEL1(I,J)=VEL1(I,J)**2.
        K1=99
   121 JJ=NPTS(IPROBE)
        DO 125 K=1,JJ
        IF(VCHAN2(IPROBE,I,J).GT.CALV2(IPROBE,K))GO TO 125
        RATIO=(VCHAN2(IPROBE,I,J)-CALV2(IPROBE,K-1))/(CALV2(IPROBE,K)-CALV
       12(IPROBE,K-1))
        VEL2(I,J)=V2(IPROBE,K-1)+RATIO*(V2(IPROBE,K)-V2(IPROBE,K-1))
        VEL2(I,J)=VEL2(I,J)**2.
        K2=K
        GO TO 122
   125 CONTINUE
        RATIO=(VCHAN2(IPROBE,I,J)-CALV2(IPROBE,JJ-1))/(CALV2(IPROBE,JJ)-CA
       1LV2(IPROBE,JJ-1))
        VEL2(I,J)=V2(IPROBE,JJ-1)+RATIO*(V2(IPROBE,JJ)-V2(IPROBE,JJ-1))
        VEL2(I,J)=VEL2(I,J)**2.
        K2=99
   122 JJ=NPTS(IPROBE)
        DO 130 K=1,JJ
        IF(VCHAN3(IPROBE,I,J).GT.CALV3(IPROBE,K))GO TO 130
        RATIO=(VCHAN3(IPROBE,I,J)-CALV3(IPROBE,K-1))/(CALV3(IPROBE,K)-CALV
       13(IPROBE,K-1))
        VEL3(I,J)=V3(IPROBE,K-1)+RATIO*(V3(IPROBE,K)-V3(IPROBE,K-1))
        VEL3(I,J)=VEL3(I,J)**2.
        K3=K
        GO TO 135
   130 CONTINUE
        RATIO=(VCHAN3(IPROBE,I,J)-CALV3(IPROBE,JJ-1))/(CALV3(IPROBE,JJ)-CA
       1LV3(IPROBE,JJ-1))
        VEL3(I,J)=V3(IPROBE,JJ-1)+RATIO*(V3(IPROBE,JJ)-V3(IPROBE,JJ-1))
        VEL3(I,J)=VEL3(I,J)**2.
        K3=99
C
C     USE NEWTON-RAPHSON METHOD TO CALCULATE MEAN VELOCITIES
C
C     FIND INITIAL VALUES OF VELOCITY USING LINEAR EQUATIONS
C
   135 D(1)=VEL1(I,J)
        D(2)=VEL2(I,J)
        D(3)=VEL3(I,J)
C
```

```
C     RE-INITIALIZE C(I,J)
C
      C(1,1)=SQRT(A4)
      C(1,2)=D4/(2.*C(1,1))
      C(1,3)=E4/(2.*C(1,1))
      C(2,1)=SQRT(A5)
      C(2,2)=D5/(2.*C(2,1))
      C(2,3)=E5/(2.*C(2,1))
      C(3,1)=SQRT(A6)
      C(3,2)=D6/(2.*C(3,1))
      C(3,3)=E6/(2.*C(3,1))
      DO 111 II=1,3
      DO 111 JJ=1,3
      CC(II,JJ)=C(II,JJ)
  111 CONTINUE
      CALL DLEQD(CC,D,3,1,3,3,DET)
      UO=D(2)
      VO=D(1)
      WO=D(3)
      VINIT=VO
      UINIT=UO
      WINIT=WO
C
C     BEGIN NEWTON-RAPHSON ITERATION ON NONLINEAR EQUATIONS
C
      DO 200 N=1,NREPS
      AA1=SQRT(A4)
      AA2=SQRT(A5)
      AA3=SQRT(A6)
      BB1=D4/(2.*AA1)
      BB2=D5/(2.*AA2)
      BB3=D6/(2.*AA3)
      CC1=AA1*(B4/(2.*A4)-D4*D4/(8.*A4*A4))
      DD1=AA1*(F4/(2.*A4)-D4*E4/(4.*A4*A4))
      EE1=E4/(2.*AA1)
      FF1=AA1*(C4/(2.*A4)-E4*F4/(8.*A4*A4))
      CC2=AA2*(B5/(2.*A5)-D5*D5/(8.*A5*A5))
      DD2=AA2*(F5/(2.*A5)-D5*E5/(4.*A5*A5))
      EE2=E5/(2.*AA2)
      FF2=AA2*(C5/(2.*A5)-E5*E5/(8.*A5*A5))
      CC3=AA3*(B6/(2.*A6)-D6*D6/(8.*A6*A6))
      DD3=AA3*(F6/(2.*A6)-D6*E6/(4.*A6*A6))
      EE3=E6/(2.*AA3)
      FF3=AA3*(C6/(2.*A6)-E6*E6/(8.*A6*A6))
      GG1=AA1*VO+BB1*UO+CC1*UO*UO/VO+DD1*UO*WO/VO+EE1*WO+FF1*WO*WO/VO
     1-VEL1(I,J)
      GG2=AA2*VO+BB2*UO+CC2*UO*UO/VO+DD2*UO*WO/VO+EE2*WO+FF2*WO*WO/VO
     1-VEL2(I,J)
      GG3=AA3*VO+BB3*UO+CC3*UO*UO/VO+DD3*UO*WO/VO+EE3*WO+FF3*WO*WO/VO
     1-VEL3(I,J)
      G1WV=AA1-CC1*UO*UO/(VO*VO)-DD1*UO*WO/(VO*VO)-FF1*WO*WO/(VO*VO)
      G2WV=AA2-CC2*UO*UO/(VO*VO)-DD2*UO*WO/(VO*VO)-FF2*WO*WO/(VO*VO)
      G3WV=AA3-CC3*UO*UO/(VO*VO)-DD3*UO*WO/(VO*VO)-FF3*WO*WO/(VO*VO)
      G1WU=BB1+2.*CC1*UO/VO+DD1*WO/VO
```

```
      G2WU=BB2+2.*CC2*UO/VO+DD2*WO/VO
      G3WU=BB3+2.*CC3*UO/VO+DD3*WO/VO
      G1WW=EE1+DD1*UO/VO+2.*FF1*WO/VO
      G2WW=EE2+DD2*UO/VO+2.*FF2*WO/VO
      G3WW=EE3+DD3*UO/VO+2.*FF3*WO/VO
      D(1)=-GG1
      D(2)=-GG2
      D(3)=-GG3
      C(1,1)=G1WV
      C(1,2)=G1WU
      C(1,3)=G1WW
      C(2,1)=G2WV
      C(2,2)=G2WU
      C(2,3)=G2WW
      C(3,1)=G3WV
      C(3,2)=G3WU
      C(3,3)=G3WW
      DO 205 II=1,3
      DO 205 JJ=1,3
      CC(II,JJ)=C(II,JJ)
  205 CONTINUE
      CALL DLEQD(CC,D,3,1,3,3,DET)
      DELV=D(1)
      DELU=D(2)
      DELW=D(3)
      WV=VO+DELV
      WU=UO+DELU
      WW=WO+DELW
C
C     APPLY CONVERGENCE CRITERIA
C
      DELV=ABS(VO-WV)
      DELU=ABS(UO-WU)
      DELW=ABS(WO-WW)
      EPSV=EPS*ABS(VO)
      EPSU=EPS*ABS(UO)
      EPSW=EPS*ABS(WO)
      IF(DELV.GE.EPSV)GO TO 210
      IF(DELU.GE.EPSU)GO TO 210
      IF(DELW.GE.EPSW)GO TO 210
C
C     SOLUTION CONVERGED
C
      WRITE(6,84)N
      WR=WU/UTIP
      WT=WV/UTIP
      WZ=WW/UTIP
      W=SQRT(WT*WT+WR*WR+WZ*WZ)
      WRITE(6,61)WT,WR,WZ,W
      GO TO 220
C
  210 WWT=WV
      WWR=WU
      WWZ=WW
```

```
      IF(N.GE.2)GO TO 206
      VO=WV
      UO=WU
      WO=WW
      WWT1=WV
      WWR1=WU
      WWZ1=WW
      GO TO 200
  206 VO=(WWT+WWT1)/2.
      WO=(WWZ+WWZ1)/2.
      UO=(WWR+WWR1)/2.
      WWT1=WWT
      WWR1=WWR
      WWZ1=WWZ
  200 CONTINUE
C
C     SOLUTION FAILED TO CONVERGE - USE INITIAL VALUES OF VELOCITY
C     CALCULATED FROM LINEAR EQUATIONS FOR TURBULENCE DERIVATIONS
C
      WRITE(6,86)NREPS
      WV=VINIT
      WU=UINIT
      WW=WINIT
      WR=WU/UTIP
      WT=WV/UTIP
      WZ=WW/UTIP
      W=SQRT(WT*WT+WR*WR+WZ*WZ)
      WRITE(6,61)WT,WR,WZ,W
C
C     USE LINEARIZED THEORY TO CALCULATE FLUCTUATING VELOCITIES
C
  220 FACT1=4.*SQRT(VCHAN1(IPROBE,I,J))*SQRT(VEL1(I,J))/SLOPE1(IPROBE)
      FACT2=4.*SQRT(VCHAN2(IPROBE,I,J))*SQRT(VEL2(I,J))/SLOPE2(IPROBE)
      FACT3=4.*SQRT(VCHAN3(IPROBE,I,J))*SQRT(VEL3(I,J))/SLOPE3(IPROBE)
      FV1=SQRT(FV1SQ)/ATTEN
      FV2=SQRT(FV2SQ)/ATTEN
      FV3=SQRT(FV3SQ)/ATTEN
      U1=FACT1*FV1
      U2=FACT2*FV2
      U3=FACT3*FV3
      FVEL1(I,J)=U1*U1
      FVEL2(I,J)=U2*U2
      FVEL3(I,J)=U3*U3
      FV1P2=FV1P2/(ATTEN*ATTEN)
      FV1M2=FV1M2/(ATTEN*ATTEN)
      FV1P3=FV1P3/(ATTEN*ATTEN)
      FV1M3=FV1M3/(ATTEN*ATTEN)
      FV2P3=FV2P3/(ATTEN*ATTEN)
      FV2M3=FV2M3/(ATTEN*ATTEN)
      FV12=(FV1P2-FV1M2)/4.
      FV13=(FV1P3-FV1M3)/4.
      FV23=(FV2P3-FV2M3)/4.
      FVEL12=FACT1*FACT2*FV12
      FVEL13=FACT1*FACT3*FV13
```

```
      IF(N.GE.2)GO TO 206
      VO=WV
      UO=WU
      WO=WW
      WWT1=WV
      WWR1=WU
      WWZ1=WW
      GO TO 200
  206 VO=(WWT+WWT1)/2.
      WO=(WWZ+WWZ1)/2.
      UO=(WWR+WWR1)/2.
      WWT1=WWT
      WWR1=WWR
      WWZ1=WWZ
  200 CONTINUE
C
C     SOLUTION FAILED TO CONVERGE - USE INITIAL VALUES OF VELOCITY
C     CALCULATED FROM LINEAR EQUATIONS FOR TURBULENCE DERIVATIONS
C
      WRITE(6,86)NREPS
      WV=VINIT
      WU=UINIT
      WW=WINIT
      WR=WU/UTIP
      WT=WV/UTIP
      WZ=WW/UTIP
      W=SQRT(WT*WT+WR*WR+WZ*WZ)
      WRITE(6,61)WT,WR,WZ,W
C
C     USE LINEARIZED THEORY TO CALCULATE FLUCTUATING VELOCITIES
C
  220 FACT1=4.*SQRT(VCHAN1(IPROBE,I,J))*SQRT(VEL1(I,J))/SLOPE1(IPROBE)
      FACT2=4.*SQRT(VCHAN2(IPROBE,I,J))*SQRT(VEL2(I,J))/SLOPE2(IPROBE)
      FACT3=4.*SQRT(VCHAN3(IPROBE,I,J))*SQRT(VEL3(I,J))/SLOPE3(IPROBE)
      FV1=SQRT(FV1SQ)/ATTEN
      FV2=SQRT(FV2SQ)/ATTEN
      FV3=SQRT(FV3SQ)/ATTEN
      U1=FACT1*FV1
      U2=FACT2*FV2
      U3=FACT3*FV3
      FVEL1(I,J)=U1*U1
      FVEL2(I,J)=U2*U2
      FVEL3(I,J)=U3*U3
      FV1P2=FV1P2/(ATTEN*ATTEN)
      FV1M2=FV1M2/(ATTEN*ATTEN)
      FV1P3=FV1P3/(ATTEN*ATTEN)
      FV1M3=FV1M3/(ATTEN*ATTEN)
      FV2P3=FV2P3/(ATTEN*ATTEN)
      FV2M3=FV2M3/(ATTEN*ATTEN)
      FV12=(FV1P2-FV1M2)/4.
      FV13=(FV1P3-FV1M3)/4.
      FV23=(FV2P3-FV2M3)/4.
      FVEL12=FACT1*FACT2*FV12
      FVEL13=FACT1*FACT3*FV13
```

```
      FVEL23=FACT2*FACT3*FV23
C
C     CALCULATE FLUCTUATING VELOCITY COEFFICIENTS
C
      AA1=SQRT(A4)
      AA2=D4/(2.*AA1)
      AA3=E4/(2.*AA1)
      AA4=AA1*(B4/(2.*A4)-D4*D4/(8.*A4*A4))
      AA5=AA1*(C4/(2.*A4)-E4*E4/(8.*A4*A4))
      AA6=AA1*(F4/(2.*A4)-D4*E4/(4.*A4*A4))
      AA7=AA1*(B4/A4-D4*D4/(4.*A4*A4))
      AA8=AA1*(C4/A4-E4*E4/(4.*A4*A4))
      AA9=AA6
      BB1=SQRT(A5)
      BB2=D5/(2.*BB1)
      BB3=E5/(2.*BB1)
      BB4=BB1*(B5/(2.*A5)-D5*D5/(8.*A5*A5))
      BB5=BB1*(C5/(2.*A5)-E5*E5/(8.*A5*A5))
      BB6=BB1*(F5/(2.*A5)-D5*E5/(4.*A5*A5))
      BB7=BB1*(B5/A5-D5*D5/(4.*A5*A5))
      BB8=BB1*(C5/A5-E5*E5/(4.*A5*A5))
      BB9=BB6
      CC1=SQRT(A6)
      CC2=D6/(2.*CC1)
      CC3=E6/(2.*CC1)
      CC4=CC1*(B6/(2.*A6)-D6*D6/(8.*A6*A6))
      CC5=CC1*(C6/(2.*A6)-E6*E6/(8.*A6*A6))
      CC6=CC1*(F6/(2.*A6)-D6*E6/(4.*A6*A6))
      CC7=CC1*(B6/A6-D6*D6/(4.*A6*A6))
      CC8=CC1*(C6/A6-E6*E6/(4.*A6*A6))
      CC9=CC6
      AAA1=AA1
      AAA2=BB1
      AAA3=CC1
      BBB1=AA2+AA7*WR/WT+AA6*WZ/WT
      BBB2=BB2+BB7*WR/WT+BB6*WZ/WT
      BBB3=CC2+CC7*WR/WT+CC6*WZ/WT
      CCC1=AA3+AA8*WZ/WT+AA6*WR/WT
      CCC2=BB3+BB8*WZ/WT+BB6*WR/WT
      CCC3=CC3+CC8*WZ/WT+CC6*WR/WT
      A(1,1)=AAA1*AAA1
      A(1,2)=BBB1*BBB1
      A(1,3)=CCC1*CCC1
      A(1,4)=2.*AAA1*BBB1
      A(1,5)=2.*AAA1*CCC1
      A(1,6)=2.*BBB1*CCC1
      A(2,1)=AAA2*AAA2
      A(2,2)=BBB2*BBB2
      A(2,3)=CCC2*CCC2
      A(2,4)=2.*AAA2*BBB2
      A(2,5)=2.*AAA2*CCC2
      A(2,6)=2.*BBB2*CCC2
      A(3,1)=AAA3*AAA3
      A(3,2)=BBB3*BBB3
```

170

```
      A(3,3)=CCC3*CCC3
      A(3,4)=2.*AAA3*BBB3
      A(3,5)=2.*AAA3*CCC3
      A(3,6)=2.*BBB3*CCC3
      A(4,1)=AAA1*AAA2
      A(4,2)=BBB1*BBB2
      A(4,3)=CCC1*CCC2
      A(4,4)=AAA1*BBB2+AAA2*BBB1
      A(4,5)=AAA1*CCC2+AAA2*CCC1
      A(4,6)=BBB1*CCC2+CCC1*BBB2
      A(5,1)=AAA1*AAA3
      A(5,2)=BBB1*BBB3
      A(5,3)=CCC1*CCC3
      A(5,4)=AAA1*BBB3+AAA3*BBB1
      A(5,5)=AAA1*CCC3+AAA3*CCC1
      A(5,6)=BBB1*CCC3+CCC1*BBB3
      A(6,1)=AAA2*AAA3
      A(6,2)=BBB2*BBB3
      A(6,3)=CCC2*CCC3
      A(6,4)=AAA2*BBB3+AAA3*BBB2
      A(6,5)=AAA2*CCC3+AAA3*CCC2
      A(6,6)=BBB2*CCC3+CCC2*BBB3
      B(1)=FVEL1(I,J)
      B(2)=FVEL2(I,J)
      B(3)=FVEL3(I,J)
      B(4)=FVEL12
      B(5)=FVEL13
      B(6)=FVEL23
      DO 113 II=1,6
      DO 113 JJ=1,6
      AA(II,JJ)=A(II,JJ)
  113 CONTINUE
      CALL DLEQD(AA,B,6,1,6,6,DET)
      B(1)=DSQRT(B(1))
      B(2)=DSQRT(B(2))
      B(3)=DSQRT(B(3))
C
C     CORRECT FLUCTUATING VELOCITIES FOR HIGH TURBULENCE INTENSITIES
C
      ARG1=1.+FACTOR*(B(1)/(W*UTIP))**2.
      ARG2=1.+FACTOR*(B(2)/(W*UTIP))**2.
      ARG3=1.+FACTOR*(B(3)/(W*UTIP))**2.
      B(1)=B(1)/SQRT(ARG1)
      B(2)=B(2)/SQRT(ARG2)
      B(3)=B(3)/SQRT(ARG3)
C
      FWT=B(1)/(W*UTIP)
      FWR=B(2)/(W*UTIP)
      FWZ=B(3)/(W*UTIP)
      WRITE(6,62)FWT,FWR,FWZ
      B(4)=B(4)/(W*W*UTIP*UTIP)
      B(5)=B(5)/(W*W*UTIP*UTIP)
      B(6)=B(6)/(W*W*UTIP*UTIP)
      WRITE(6,63)B(4),B(5),B(6)
```

171

```
      QSQD=FWR*FWR+FWZ*FWZ+FWT*FWT
      WRITE(6,67)QSQD
      RATIO1=B(4)/QSQD
      RATIO2=B(5)/QSQD
      RATIO3=B(6)/QSQD
      WRITE(6,68)RATIO1,RATIO2,RATIO3
      WRITE(6,99)
  110 CONTINUE
  115 CONTINUE
C
C     FORMAT STATEMENTS
C
    5 FORMAT(9X,I1)
    6 FORMAT(3F10.5)
   10 FORMAT(8X,I2,F10.5)
   15 FORMAT(4F10.5)
   20 FORMAT(9X,I1,8X,I2)
   25 FORMAT(10F7.3)
   32 FORMAT(6F10.5)
   40 FORMAT(9X,I1,9X,I1)
   45 FORMAT(3F10.6)
   46 FORMAT(4F10.6)
   47 FORMAT(4F10.6,9X,I1)
   61 FORMAT(10X,'MEAN VELOCITIES :',4E15.5)
   62 FORMAT(10X,'TURBULENCE INTENSITIES :',3E15.5)
   63 FORMAT(10X,'TURBULENCE STRESSES :',3E15.5)
   67 FORMAT(10X,'TOTAL TURBULENCE ENERGY :',E15.5)
   68 FORMAT(10X,'STRESS/ENERGY RATIOS :',3E15.5)
   70 FORMAT(3F10.5)
   75 FORMAT(6F10.6)
   82 FORMAT(5X,I5,F10.5)
   84 FORMAT(5X,'MEAN VELOCITIES CONVERGED IN',I5,'ITERATIONS')
   86 FORMAT(5X,'MEAN VELOCITIES DID NOT CONVERGE AFTER',I5,'ITERATIONS'
     1/)
   99 FORMAT(1X,//)
      STOP
      END
```

| 1. Report No. NASA CR-3333 | 2. Government Accession No. | 3. Recipient's Catalog No. |
|---|---|---|
| 4. Title and Subtitle  ANALYTICAL AND EXPERIMENTAL STUDY OF MEAN FLOW AND TURBULENCE CHARACTERISTICS INSIDE THE PASSAGES OF AN AXIAL FLOW INDUCER | | 5. Report Date November 1980 |
| | | 6. Performing Organization Code |
| 7. Author(s) C. A. Gorton and B. Lakshminarayana | | 8. Performing Organization Report No. PSU-Aersp 74-2 |
| | | 10. Work Unit No. |
| 9. Performing Organization Name and Address The Pennsylvania State University 233 Hammond Building University Park, Pennsylvania 16802 | | |
| | | 11. Contract or Grant No. NGL 39-009-007 |
| | | 13. Type of Report and Period Covered Contractor Report |
| 12. Sponsoring Agency Name and Address National Aeronautics and Space Administration Washington, D.C. 20546 | | |
| | | 14. Sponsoring Agency Code |

16. Abstract

This report summarizes the research carried out in understanding the complex inviscid and viscid effects existing within the passages of a three-bladed axial flow inducer operating at a flow coefficient of 0.065. The experimental investigations undertaken included determination of the blade static pressure and blade limiting streamline angle distributions, and measurement of the three components of mean velocity, turbulence intensities and turbulence stresses at locations inside the inducer blade passage utilizing a rotating three-sensor hotwire probe.  Applicable equations were derived for the hotwire data reduction analysis and solved numerically to obtain the appropriate flow parameters.  Analytical investigations were conducted to predict the three-dimensional inviscid flow in the inducer by numerically solving the exact equations of motion, and to approximately predict the three-dimensional viscid flow by incorporating the dominant viscous terms into the exact equations.  The analytical results are compared with the experimental measurements and design values where appropriate.  Radial velocities are found to be of the same order as axial velocities within the inducer passage, confirming the highly three-dimensional characteristic of inducer flow and emphasizing the necessity for a suitable three-dimensional theory for accurate flow prediction. Total relative velocity distributions indicate a substantial velocity deficiency near the tip at mid-passage which expands significantly as the flow proceeds toward the inducer trailing edge.  High turbulence intensities and turbulence stresses are concentrated within this core region.  Considerable wake diffusion occurs immediately downstream of the inducer trailing edge to decay this loss core.  Evidence of boundary layer interactions, blade blockage effects, radially inward flows, annulus wall effects and backflows are all found to exist within the long, narrow passages of the inducer, emphasizing the complex nature of inducer flow which makes accurate prediction of the flow behavior extremely difficult.

| 17. Key Words (Suggested by Author(s)) Rocket pump inducers Turbomachinery Three dimensional flow | 18. Distribution Statement Unclassified - unlimited STAR Category 02 |
|---|---|

| 19. Security Classif. (of this report) Unclassified | 20. Security Classif. (of this page) Unclassified | 21. No. of Pages 178 | 22. Price* A09 |
|---|---|---|---|